

**THERMODYNAMIC OPTIMIZATION UNDER
TOPOLOGICAL CONSTRAINTS**

THERMODYNAMIC OPTIMIZATION UNDER TOPOLOGICAL CONSTRAINTS

By

THEVIKA BALAKUMAR,

B.Sc. Eng.

University of Moratuwa, Sri Lanka, 2000

M. A. Sc.

Concordia University, Canada, 2004

A Thesis

Submitted to the School of Graduate Studies

in partial fulfilment of the requirements

for the degree

Doctor of Philosophy

McMaster University

©Copyright by Thevika Balakumar, May 2008

To my husband Bala
and
our dearest son Athavan

ABSTRACT

Computational thermodynamics is a powerful tool for solving practically important problems including the design of new materials and the analysis of their internal and external stability. This thesis contributes to computational thermodynamics by proposing several practical solutions to eliminate the so-called *thermodynamic artifacts* rather frequently found in thermodynamic assessments.

First, a method is developed to eliminate the artifacts such as inverted miscibility gaps in the liquid phase at high-temperatures and reappearance of the liquid phase at low-temperatures or reappearance of a solid phase at elevated temperatures. This method is based on introducing a sufficiently dense mesh of knots (not related to experimental points utilized in the optimization) and ensuring that specific inequality conditions (topological constraints) governing the appearance of the phase diagram are satisfied in these knots. A feasibility of the approach proposed is exemplified by carrying out a re-optimization of the Mg–Sb system.

Generally re-optimization of a system would take months to get the optimized results. Hence, to minimize time needed to get rid of artifacts, two different quick correction methods are developed to eliminate the unrealistic inverted miscibility gap in the liquid phase at elevated temperatures. Both methods employ optimization under topological constraints via controlling the sign of the second derivative of the Gibbs energy. Their applicability is exemplified on the Sn–Zr system.

Also, a theoretical study was done on undulate phase boundaries. Usually, an inflection point on a phase boundary is considered as an unambiguous indication that one

of the phases participating in the equilibrium is internally unstable, i.e., that it is prone to phase separation. It has been generally assumed that an inflection point may occur only if the thermodynamic model of this phase contains an excess Gibbs energy term. It is shown that in contrast to this assumption, inflection points on a phase boundary may appear when a pure solid component or a stoichiometric binary phase is in equilibrium with the ideal binary solution, which is internally stable.

Finally, in addition to the theoretical analysis on undulate phase boundaries, a thermodynamic optimization is done on an imaginary A-B binary system subjected to topological constraints. Since, Thermo-Calc does not have the necessary tools to implement such topological constraints as $d^2T/dx^2 > 0$ or $d^2T/dx^2 < 0$. A Fortran 90 program was developed to make use of these constraints.

ACKNOWLEDGEMENTS

First of all, I would like to express my sincere gratitude to my supervisor Dr. Dmitri V. Malakhov, who offered me an opportunity to be a graduate student and conduct research under his supervision. I am grateful to Dr. Malakhov for spending his precious time with me discussing my work, my research papers and this thesis.

I acknowledge the financial support provided by Natural Sciences and Engineering Research Council, Canada.

I thank Professor Antony Petric and Dr. Nikolas Provatas for serving in my supervisory committee and for giving valuable suggestions on my research.

I am grateful to all staff members of our department for their kind support. Especially, I thank Mrs. Elvira Evangelista, Mrs. Mary Mitchell and Mrs. Jane Mah for their constant help and support. Further, I thank Mr. Ed McCaffery who solved all my computer related problems. I am grateful to my fellow graduate students for their support during my studies.

I had a challenging PhD period that my husband was also a PhD student during the same period and we have been raising our son during the same period. All of it would have been impossible without the support of my husband's PhD supervisor Dr. T. Kirubarajan who was very kind and flexible with my husband in research meetings and delayed paper submissions. For the same reason, I once again thank my supervisor.

I thank my parents and siblings for their endless support of me during my PhD period and beyond.

Finally but most importantly, I would like to acknowledge the love and support I received from my husband, Bala, and our wonderful son, Athavan, during my studies.

TABLE OF CONTENTS

ABSTRACT.....	IV
ACKNOWLEDGEMENTS.....	VI
LIST OF FIGURES.....	XII
LIST OF TABLES.....	XX
SYMBOLS AND ABBREVIATIONS.....	XXI
CHAPTER 1: Introduction.....	1
1.1 Thermodynamic optimization.....	1
1.2 Overview of the thesis.....	3
1.2.1 Motivation and objectives of the thesis.....	3
1.2.2 Thesis outline.....	4
1.2.3 Contributions.....	6
1.2.4 Related publications.....	7
CHAPTER 2: Thermodynamic optimization: The past and present.....	9
2.1 Historical notes.....	9
2.2 Integral parts of thermodynamic optimization.....	10
2.2.1 Models of phases.....	10
2.2.1.(a) Models for phases with fixed composition.....	11
2.2.1.(b) Models for phases with variable compositions...	13
2.2.2 Optimization tools.....	18
2.2.3 Databases.....	21
2.2.4 Software for thermodynamic optimization.....	23
2.3 Algorithmic details of thermodynamic optimization.....	25
2.3.1 Gibbs energy minimization.....	26
2.3.2 Conditions of equilibrium.....	27
2.3.3 Finding the equilibrium conditions.....	29
2.3.4 Model parameter optimization.....	34

2.4 Conclusions.....	36
CHAPTER 3: Post-optimization artifacts.....	37
3.1 What are artifacts?.....	37
3.2 Classifications of artifacts.....	37
3.2.1 Non-existing and erroneous phase boundaries.....	38
3.2.1.(a) Non-real inverted miscibility gaps in the liquid phase at high-temperatures.....	38
3.2.1.(b) Excessive number of inflection points on phase boundaries/ undulate phase boundaries.....	46
3.2.1.(c) Low-temperature phase becomes stable again at high-temperature.....	54
3.2.2 Suspicious temperature and composition dependencies of properties.....	56
3.3 How to eliminate artifacts?.....	59
3.3.1 Eliminating artifacts by using physically feasible models..	59
3.3.2 Kaptay's method of artifact elimination.....	63
3.4 Conclusions.....	67
CHAPTER 4: Shape-preserving approximation.....	68
4.1 Introduction.....	68
4.2 Existing methods of isogeometric curve and surface fitting.....	69
4.3 Isogeometric interpolations by splines.....	70
4.4 Spline approximation in thermodynamic optimizations.....	72
4.5 Conclusions.....	74
CHAPTER 5: Topological constraint in eliminating inverted miscibility gaps during re-assessment of the Mg-Sb system.....	75
5.1 Introduction.....	75
5.2 Problem formulation.....	75
5.3 Possible approaches to the problem.....	80
5.4 A non-thermodynamic example.....	82

7.2.1 Slope of the phase boundary.....	144
7.2.2 Curvature of the phase boundary.....	146
7.3 Simplifications.....	148
7.4 Analysis.....	152
7.5 Conclusion.....	159
CHAPTER 8: Topological constraints in eliminating suspicious inflexion points on phase boundaries.....	160
8.1 Introduction.....	160
8.2 Aim.....	161
8.3 An imaginary A-B binary system with undulated liquidus and solidus.....	162
8.3.1 Generating the A-B phase diagram.....	162
8.3.2 Calculation of slopes and curvatures.....	165
8.3.3 Derivatives to calculate dx^S/dx^L , dT/dx^L , $d^2x^S/d(x^L)^2$ and $d^2T/d(x^L)^2$	167
8.4 Thermodynamic optimization of the A-B system under topological constraints.....	168
8.4.1 Model selection.....	168
8.4.2 Optimization.....	169
8.4.3 Results.....	170
8.5 Conclusions.....	174
CHAPTER 9: Concluding remarks and future directions.....	175
9.1 Concluding remarks.....	175
9.2 Future directions.....	176
 BIBLIOGRAPHY.....	 177
APPENDIX I.....	195
APPENDIX II.....	197

LIST OF FIGURES

Figure 1: Formation of a real solution $A_{(1-x)}B_x$ of structure ϕ at T_s and P_s	14
Figure 2: Some ternary extrapolation methods.....	17
Figure 3: General structure of the Thermo-Calc package [59].....	24
Figure 4: Newton's method.....	30
Figure 5: $f(x) = x \exp(-x)$ produces a divergent sequence.....	32
Figure 6: $f(x) = x^3 - x - 3$ produces a cyclic sequence.....	32
Figure 7: $f(x) = \arctan(x)$ produces divergent oscillations.....	32
Figure 8: A plot of Gibbs energy of mixing Vs Mole fraction for parameters $h_{0i} = -10000$ and $s_{0i} = -22$ at different temperatures.....	41
Figure 9: Calculated Si-Ta binary phase diagram using the parameters of [77] by Chen <i>et al.</i> [75].....	43
Figure 10: Calculated Sn-Zr phase diagram using a thermodynamic description published in the literature [79] by Chen <i>et al.</i> [75].....	44
Figure 11: Calculated Mg-Si phase diagram using the parameters of [82] by Kevorkov <i>et al.</i> [81].....	44
Figure 12: Calculated Mg-Si phase diagram using the parameters of [83] by Kevorkov <i>et al.</i> [81].....	45
Figure 13: Calculated phase diagram of the Pt-Sn system using the parameters of [85] by Grolier and Schmid-Fetzer [84].....	45

Figure 14: Calculated Mg-Sb phase diagram using the parameters of [86].....	46
Figure 15: Calculated Cd-Na phase diagram using the thermodynamic descriptions of [87] (extracted from [88]).....	47
Figure 16: Calculated phase diagram of the Sn-Zn system by [89].....	48
Figure 17: Calculated phase diagram of the In-Zn system by [89].....	48
Figure 18: Topological changes in the phase diagram for a system A-B with regular solid and liquid phases [90].....	49
Figure 19: Calculated Se-As phase diagram by Degterov <i>et al.</i> [91].....	51
Figure 20: Gd-Mg phase diagram calculated by [92].....	52
Figure 21: Calculated phase diagram of the V-Hf binary system by [93].....	53
Figure 22: Co-Si phase diagram calculated by [94].....	54
Figure 23: Calculated Ni-Ti phase diagram using the parameters of [97] by Chen <i>et al.</i> [75].....	55
Figure 24: Calculated Co-Si phase diagram using the parameters of [102] by Chen <i>et al.</i> [75].....	55
Figure 25: Partial and integral molar Gibbs free energies of liquid Bi-Sn solution as a function of composition at 400°C calculated by Cho and Ochoa [103].....	56
Figure 26: The calculated Fe content of the liquid phase in the liq/fcc/bcc three- phase equilibrium in the Fe-Cr-Ni system by Lee [104].....	58
Figure 27: The calculated Mg-Si phase diagram by Schmid-Fetzer <i>et al.</i> [109] using the Kaptay's formalism in (3.34).....	66

Figure 28: Activity calculations of Cd in Cd-Au system at 777K by [118] shows the comparison of spline approximation (line 1) with the conventional linear least squares approximation (line 2).....	73
Figure 29: Calculation of integral molar enthalpy of formation of Al-Te alloys at 1188K by [118] shows the comparison of spline approximation (line 1) with the conventional linear least squares approximation (line 2).....	73
Figure 30: The calculated phase diagram of the Mg-Sb system by Balakumar and Medraj [86].....	76
Figure 31: Inverted miscibility gaps resulted from the thermodynamic model for the liquid phase proposed in [86].....	77
Figure 32: A plot of $QF\langle L \rangle$ Vs mole fraction of Sb at different temperatures for the Mg-Sb liquid description in [86].....	79
Figure 33: A plot of $QF\langle L \rangle$ Vs mole fraction of Zn at different temperatures for the Bi-Zn liquid description in [127].....	82
Figure 34: Fitting of kinetic data with physically feasible models.....	84
Figure 35: Fitting of kinetic data with formal mathematical expressions.....	87
Figure 36: Phase diagram of the Mg-Sb system resulted from an unconstrained optimization.....	93
Figure 37: Phase diagram of the Mg-Sb system resulted (by the use of the Thermo-Calc command, AMEND_PHASE_DESCRIPTION) from an unconstrained optimization.....	94

Figure 38: A plot of $QF\langle L \rangle$ Vs mole fraction of Sb at elevated temperatures: for the unconstrained optimization.....	95
Figure 39: Phase diagram of the Mg-Sb system resulted from an optimization in the course of which topological constraints were imposed on the HCP+L/L liquidus.....	97
Figure 40: A plot of $QF\langle L \rangle$ Vs mole fraction of Sb at elevated temperatures: topological constraints were imposed on the HCP+L/L liquidus.....	98
Figure 41: Phase diagram of the Mg-Sb system resulted from an optimization in the course of which topological constraints were imposed on the HCP+L/L liquidus and on the sign of $\partial^2 G^L / \partial (x^L)^2$	101
Figure 42: A plot of $QF\langle L \rangle$ Vs mole fraction of Sb at elevated temperatures: topological constraints were imposed on the HCP+L/L liquidus and on the sign of $\partial^2 G^L / \partial (x^L)^2$	102
Figure 43: Comparison of the molar Gibbs energies of the liquid phase at 1000 K resulted from unconstrained and topologically constrained optimizations.....	104
Figure 44: Comparison of the molar Gibbs energies of the liquid phase at 2000 K resulted from unconstrained and topologically constrained optimizations.....	105
Figure 45: Phase diagram of the Sn–Zr system as presented in [79].....	109

Figure 46: Phase diagram of the Sn–Zr system with an inverted miscibility gap discovered.....	110
Figure 47: Location of knots at which the topological constraint $\partial^2 G/\partial x^2$ was used.....	114
Figure 48: Phase diagrams constructed with the old and new models.....	118
Figure 49: Molar Gibbs energies of mixing at 1250 K resulting from the old and new models.....	119
Figure 50: Molar enthalpies of mixing at 1250 K computed with the old and new models.....	120
Figure 51: Activities of Sn and Zr in the liquid phase at 1250 K calculated with the old and new models.....	120
Figure 52: Molar Gibbs energies of mixing at 1750 K resulting from the old and new models.....	121
Figure 53: Molar enthalpies of mixing at 1750 K computed with the old and new models.....	122
Figure 54: Activities of Sn and Zr in the liquid phase at 1750 K calculated with the old and new models.....	122
Figure 55: Molar Gibbs energies of mixing at 2750 K resulting from the old and new models.....	123
Figure 56: Molar enthalpies of mixing at 2750 K computed with the old and new models.....	124
Figure 57: Activities of Sn and Zr in the liquid phase at 2750 K calculated with	

the old and new models.....	124
Figure 58: Hatched area is a “similarity region” within which a new model is made similar to the old model. • are knots at which the topological constraint $\partial^2 G/\partial x^2$ was employed.....	134
Figure 59: Phase diagrams constructed with the old and new models.....	135
Figure 60: Temperature-independent molar enthalpies of mixing computed with the old and new models.....	136
Figure 61: Molar Gibbs energies of mixing at 1250 K resulting from the old and new models.....	137
Figure 62: Activities of Sn and Zr in the liquid phase at 1750 K calculated with the old and new models.....	138
Figure 63: Molar Gibbs energies of mixing at 1750 K predicted by the old and new models.....	138
Figure 64: Activities of Sn and Zr in the liquid phase at 1750 K computed with the old and new models.....	139
Figure 65: Molar Gibbs energies of mixing at 2750 K predicted by the old and new models.....	139
Figure 66: Activities of Sn and Zr in the liquid phase at 2750 K according to the old and new models.....	140
Figure 67: A metastable miscibility gap in the liquid phase (dashed curve) superimposed on the equilibrium Sn–Zn phase diagram.....	142

Figure 68: A schematic diagram shows the phase equilibrium boundary between a solution phase L and a stoichiometric phase α in an imaginary A-B binary system.....	143
Figure 69: The relationship between Gibbs energy and temperature for stable phases.....	149
Figure 70: A family of phase boundaries corresponding to the equilibrium between the ideal solution and the pure solid first component constructed for various entropies of fusion.....	155
Figure 71: An example of concentration dependencies of the LHS of (7.31) for different entropies of fusion and compositions of the stoichiometric phase.....	157
Figure 72: A phase diagram unambiguously demonstrating the presence of inflection points at the phase boundary for the case when the ideal solution is in equilibrium with a stoichiometric phase.....	158
Figure 73: An imaginary A-B phase diagram.....	162
Figure 74: A comparison of different models in the calculation of the A-B imaginary binary phase diagram.....	170
Figure 75: A comparison of different models in the calculation of $\Delta_{\text{mix}} G^S$ in A-B binary system at 823.15 K.....	171
Figure 76: A comparison of different models in the calculation of μ^{ex} solid in A-B binary system at 823.15 K.....	172

Figure 77: A comparison of different models in the calculation of $\Delta_{\text{mix}} G^L$ in A-B

binary system at 1473.15 K..... 173

Figure 78: A comparison of different models in the calculation of μ^{ex} liquid in

A-B binary system at 1473.15 K..... 174

LIST OF TABLES

Table 1: Experimental data used in the present re-optimization of the magnesium-antimony system.....	91
Table 2: Numerical values of the interaction parameters resulted from unconstrained and constrained optimizations of the Mg-Sb system (a reference to a figure showing a phase diagram calculated with the given set of coefficients is given in the parentheses).....	103
Table 3: Interaction parameters used in previous assessments to describe the excess Gibbs energy of the liquid phase in the Sn-Zr system.....	109
Table 4: Characteristics of invariant equilibria in the Sn-Zr system.....	112
Table 5: Statistically optimum values of adjustable parameters in (6.3) for describing the excess Gibbs energy of the liquid phase by two alternative models.....	117

SYMBOLS AND ABBREVIATIONS

a	Activity
B	Bulk modulus
C_A^0	Initial concentration of A
C_A	Concentration of A
$\vec{C}^\alpha, \vec{C}^\beta$	Vector of coefficients
C_i	Coefficients
C_p	Heat capacity at constant pressure
C_v	Heat capacity at constant volume
F	Helmholtz energy
G	Integral Gibbs energy of a phase
G_m	Molar integral Gibbs energy
G_m^{ref}	Molar reference Gibbs energy
G_m^{id}	Molar ideal Gibbs energy
${}^0G_i^\varphi$	Standard molar Gibbs energy of the phase φ
$G_m^{ex,\varphi}$	Excess molar Gibbs energy of the phase φ
g^0	Standard chemical potential
H	Enthalpy
k_1, k_2	Kinetic constant
K	Isothermal compressibility
L_{ij}	Substitutional solution binary interaction parameters
L_{ijk}	Substitutional solution ternary interaction parameters
L_{ijkl}	Substitutional solution quaternary interaction parameters
${}^vL_{ij}$	Redlich-Kister binary interaction parameters

N	Total number of measurements
n, n_i, n_j	Number of moles
$P_m(t)$	A polynomial function of t of the order m
P	Pressure
p	Weighting factor
R	Universal gas constant
S	Entropy
t	Time
T	Temperature
U	Internal energy
V	Volume
V^0	Molar volume at room temperature
w_1, w_2	Rate of transformation
w_i	Weighting factor
x_i	Mole fraction of constituent i
x^L	Mole fraction of phase
y	Site fractions
α	Thermal expansion
γ_i	Activity coefficient of element i
μ_i	Chemical potential (partial Gibbs energy)
τ_j	Positions of the knots

CHAPTER 1

Introduction

1.1 Thermodynamic optimization

Thermodynamic optimization is a process of modeling thermodynamic properties of each phase and simulating multicomponent multiphase behavior in complex systems. This process is often referred to as thermodynamic modeling, thermodynamic assessment, or CALPHAD (CALculation of PHase Diagrams) technique in the literature. By performing a thermodynamic optimization, one obtains the state functions (usually, Gibbs energies) of phases in a system. The state function depends on its natural variables, which, in the case of the Gibbs energy, are temperature, pressure, and number of moles of components.

The advantage of having such a state function is that it enables one to perform a wide range of thermodynamic calculations. In the field of materials science and engineering, these calculations are useful not only in research and development but also in solving industrial problems [1, 2]. Examples of thermodynamic optimization in many different applications include the reduction of the alloy development cycle time [3], the development of Pb-free solders [4, 5], the analysis of homogenization of Cu-Ni-Sn alloys [6], the interpretation of the growth of inter-metallic layers and the formation of dross when galvanizing in Cr-added Zn bath [7].

The most attractive feature of thermodynamic optimization is that the evaluated Gibbs energies can be used for estimation and prediction of thermodynamic properties

and phase boundaries beyond the regions of available experimental data. Let us recall that for many systems, a comprehensive experimental investigation was not performed. In such cases, a full-scale thermodynamic analysis is possible through thermodynamic optimization, which has the ability to use available fragmentary experimental results to build Gibbs energy functions for all phases in the system of interest.

A vast number of examples can be found for such thermodynamic estimations and predictions in the literature. One selected example is [8] where the thermodynamic optimization was used for the estimation of confidence intervals of calculated phase boundaries. Another selected example is [9] where the thermodynamic optimization was used for the prediction of solid-liquid interface stability and dendritic growth in several industrial Al-Si-Mg alloys.

The successful use of thermodynamic optimization in thermodynamic calculations, predictions, and estimations depends on the accuracy and reliability of the evaluated Gibbs energy functions during an optimization. The traditional thermodynamic optimization technique consists of two steps. Firstly phase models for each phase that may exist in a system are selected. These phase models are analytical expressions that describe the Gibbs energies of each phase. Depending on the depth of our knowledge of phase structure and physical properties, the phase models could be either physically feasible models or mathematically convenient formalisms. Some of these phase models contain adjustable coefficients that are often referred to as model parameters. Secondly a non-linear least squares optimization is performed in order to find the statistically optimal values for the model parameters that provides the best match between available

experimental values and the calculated quantities. Different types of experiments are used to measure thermodynamic properties of individual phases, thermodynamic properties of multiphase mixtures, and to determine the conditions of phase equilibria.

1.2 Overview of the thesis

1.2.1 Motivation and objectives of the thesis

Essentially, the traditional thermodynamic optimization technique is accuracy based non-linear least square optimization where the adjustable coefficients in the phase models are evaluated through the minimization of the sum of weighted squares of deviations between the experimental values and corresponding calculated values. Hence, one could expect highly accurate reproduction of experimentally measured thermodynamic properties and phase boundaries within the regions where experiments have been carried out.

However, accurate reproduction of experimental data does not guarantee that the evaluated phase models correctly extrapolates the thermodynamic properties and phase boundaries beyond the regions of available experimental data. A thermodynamic extrapolation is said to be correct when it is not merely numerically accurate, but also when it provides a topologically accurate thermodynamic properties and phase boundaries.

Topology of thermodynamic properties and phase boundaries are defined by their characteristic shapes such as regions of convexity and concavity, and existence of saddle points. In a thermodynamic optimization reproduction of these characteristic features is very important because they may reflect the (or “may be reflected to the”) stability of a

phase in the system. For example, a flat liquidus with an inflection point indicates the instability of the liquid phase below liquidus.

Since the sole criterion of the traditional thermodynamic optimization is the accuracy with which the experimental data are reproduced, the traditional (or “habitual”) thermodynamic optimization may result in erroneous topology of the thermodynamic properties and the phase boundaries as well as in other deficiencies. These defective features are referred to as artifacts of thermodynamic optimization or, sometimes, as phantoms of approximation. Hence, there exist an area for research and development of new thermodynamic optimization technique that not merely detects, but eliminates possible thermodynamic artifacts.

Motivated by the above facts, a new thermodynamic optimization technique that uses topological constraints is presented in this thesis.

1.2.2 Thesis outline

Chapter 1 gives an introduction to the traditional thermodynamic optimization and emphasizes its importance and usefulness. Further, unaddressed challenges of traditional thermodynamic optimization are presented, and the motivation for this research is discussed.

Chapter 2 starts with a short historical note on thermodynamic optimization. Then it presents descriptions of four principal components of thermodynamic optimization such as models, minimization engines, databases and software. Finally, this chapter provides algorithmic details of a thermodynamic optimization. As an example, it is

explained, how the equilibrium state of a system is evaluated through Newton-Raphson method.

Chapter 3 gives a review on possible thermodynamic artifacts. Many examples for different types of artifacts from published articles are given. The existing methods in eliminating these artifacts are described and their limitations are pointed to.

Chapter 4 gives background information on existing shape-preserving optimization techniques. It is discussed why the existing shape-preserving methods cannot be directly applied in thermodynamic optimization to accentuate the novelty of algorithms reported in this thesis.

Chapter 5 presents the new thermodynamic approach, which employs topological constraints during the thermodynamic assessment in eliminating non-real inverted miscibility gaps. Firstly, a non-thermodynamic example is presented to illustrate why the topological features are to be considered during thermodynamic optimization. Then a re-optimization of the Mg-Sb system is presented to exemplify the proposed topologically constrained thermodynamic optimization in eliminating non-real inverted miscibility gaps.

Chapter 6 presents two quick correction methods that eliminate the non-real inverted miscibility gaps in much faster and easier way than a full-scale re-optimization under topological constraints. The proposed quick correction methods are exemplified through the optimization of Sn-Zr binary system.

Chapter 7 presents a new thermodynamic finding on the existence of inflexion point along phase boundaries. The so-called “2R” rule is formulated in this chapter.

Chapter 8 presents elimination of incorrect undulation on phase boundaries through a topologically constrained thermodynamic optimization technique. This technique is exemplified by optimizing an imaginary A-B system under topological constraints.

Chapter 9 provides concluding remarks on the thesis and suggests possible future extensions to the research.

1.2.3 Contributions

The scientific contributions of the thesis are:

- **Novel thermodynamic optimization technique:** Due to the accuracy-based nature of the target function used in the traditional thermodynamic optimization, a number of assessments resulted in thermodynamic artifacts. In order to eliminate these artifacts, a new topologically constrained thermodynamic optimization technique is proposed. The successful application of this new technique is exemplified via the re-optimization of the Mg-Sb system.
- **Quick correction methods to eliminate non-real inverted miscibility gaps:** To correct frequently observed non-real inverted miscibility gaps, two correction methods are proposed. They not only use topological constraints, but also use the valuable information from the previous assessment that produced the artifact. The workability of these quick correction methods is exemplified through the optimization of the Sn-Zr system.
- **Theoretical analysis on the existence of inflection points on phase boundaries:** Through the calculation of slopes and curvatures of phase boundaries, a new

mathematical criterion governing the presence of inflection points on the phase boundary is formulated.

- Elimination of erroneous undulation from phase boundaries: An example of a topologically constrained thermodynamic optimization performed on imaginary A-B system shows that a successful elimination of erroneous undulations on phase boundaries is in principle possible.

1.2.4 Related publications and presentations

Some selected contents of this thesis are published in the following journals:

1. Dmitri V. Malakhov, Thevika Balakumar “Re-optimization of the Mg-Sb system under topological constraints” *International journal of materials research* 2006, Vol.97, No.5, P.517-525
2. Dmitri V. Malakhov, Thevika Balakumar “Post-optimization elimination of inverted miscibility gaps” *International journal of materials research* 2007, Vol.98, No.9, P.786-796
3. Dmitri V. Malakhov, Thevika Balakumar “Undulate phase boundaries on binary $T-x$ diagrams” *Calphad* 2008, Vol.32, No.1, P.89-93

Some of the results reported in this thesis have been presented in the following conferences and workshops:

1. Dmitri V. Malakhov, Thevika Balakumar “Thermodynamic optimization under topological constraints: principles and examples” XXXV CALPHAD Meeting, 7-12 May 2006, Haifa, Israel

2. Dmitri V. Malakhov, Thevika Balakumar "A particular type of post-optimization artifacts and approaches to their elimination" XXXVI CALPHAD Meeting, 6-11 May 2007, State College, PA, USA

CHAPTER 2

Thermodynamic optimization: The past and present

2.1 Historical notes

Calculation of phase diagrams from thermodynamic properties of phases was first initiated by Van Laar [10, 11] in 1908. In Van Laar's works, only binary systems were analyzed, and only ideal and regular solution models were employed. Almost half a century later, Meijering [12-16] extended the work of Van Laar to multicomponent systems. In the following years, many researchers started to use phase equilibria data in the evaluation of the thermodynamic properties of alloys [17-22]. In later years, computers were being used in phase diagram calculations. At that time, researchers developed their own software (written almost exclusively in FORTRAN) and generated phase diagrams through computer calculations. Among those researchers, Larry Kaufman is the first person to lay the foundation for the present day thermodynamic optimization called CALPHAD technique. The essence of his approach was summarized in the monograph [23]. Following Kaufman's landmark work, many research groups worked on developing phase diagram calculating software packages. The most widely used software packages are listed in section 2.2.4.

2.2 Integral parts of thermodynamic optimization

The CALPHAD technique consists of four main components. They are models of phases, minimization engines, databases, and software packages. Each of these components is briefly discussed in this section.

2.2.1 Models of phases

In thermodynamic assessment of a system, choosing phase models for all phases that may exist in the system is a crucial task. Here the phase model refers to an analytical description of the Gibbs energy of a phase as a function of temperature, composition, and, if necessary, pressure. That is,

$$G = G(T, P, n) \quad (2.1)$$

The reason to model the Gibbs energy and not any other thermodynamic function is that, from Gibbs energy all other thermodynamic properties can be derived. For example:

$$V = \left(\frac{\partial G}{\partial P} \right)_{T,n} \quad (2.2)$$

$$S = - \left(\frac{\partial G}{\partial T} \right)_{P,n} \quad (2.3)$$

$$H = G - T \left(\frac{\partial G}{\partial T} \right)_{P,n} \quad (2.4)$$

$$U = G - T \left(\frac{\partial G}{\partial T} \right)_{P,n} - P \left(\frac{\partial G}{\partial P} \right)_{T,n} \quad (2.5)$$

$$F = G - P \left(\frac{\partial G}{\partial P} \right)_{T,n} \quad (2.6)$$

$$C_p = -T \left(\frac{\partial^2 G}{\partial T^2} \right)_{P,n} \quad (2.7)$$

$$\mu_i = \left(\frac{\partial G}{\partial n_i} \right)_{T,P,n_j} \quad (2.8)$$

$$\alpha = \frac{1}{V} \left(\frac{\partial^2 G}{\partial P \partial T} \right)_n \quad (2.9)$$

$$K = -\frac{1}{V} \left(\frac{\partial^2 G}{\partial P^2} \right)_{T,n} \quad (2.10)$$

$$B = 1/K \quad (2.11)$$

In an alloy system one could find the following two types of phases:

- (a) Phases with fixed composition (e.g. a pure element, a stoichiometric compound)
- (b) Phases with variable compositions (e.g. a solution)

When modeling a phase, one should consider its physical and chemical properties such as crystallography, types of bonding, and magnetic properties. In modeling condensed phases (liquids and solids) the pressure-dependent properties such as volume and thermal expansivity are often ignored due to their insignificant contribution to the Gibbs energy.

2.2.1.(a) Models for phases with fixed composition

Even though phases are modeled via Gibbs energy functions, in practice, phases with fixed composition are described by their heat capacities. Generally, heat capacity of such a phase is described by Maier and Kelly type equation [24]:

$$C_p = a + bT + cT^{-2} + dT^2 + \dots \quad (2.12)$$

To derive the Gibbs energy function from (2.12), one should use the following relations with Gibbs-Helmholtz equation $G = H - TS$:

$$H = H^{298} + \int_{298}^T C_p dT \quad (2.13)$$

$$S = S^{298} + \int_{298}^T \frac{C_p}{T} dT \quad (2.14)$$

where H^{298} and S^{298} are standard enthalpy and entropy of the substance respectively.

Now from (2.12)-(2.14), one obtains the Gibbs energy of a phase with fixed composition as:

$$G = A + BT + CT \ln T + DT^2 + ET^{-1} + FT^3 + \dots \quad (2.15)$$

The Gibbs energy description in (2.15) is adequate for phases with fixed composition if pressure dependence and magnetic ordering are not taken into account.

Even though pressure dependence to the Gibbs energy of a condensed phase is negligible, its contribution is important at very high pressures. For condensed phases Murnaghan [25] suggested the following pressure contribution to the Gibbs energy:

$$\text{pressure } G = V^0 \exp \left[\int_{298}^T \alpha(T) dT \right] \frac{[1 + nK(T)P]^{(1-\frac{1}{n})} - 1}{(n-1)K(T)} \quad (2.16)$$

where V^0 is the molar volume at room temperature, $\alpha(T)$ is thermal expansion, $K(T)$ is the compressibility at 1 bar, and n is the pressure derivative of the bulk modulus (bulk modulus = inverse of compressibility). Moreover, $\alpha(T)$ and $K(T)$ are expressed as:

$$\alpha(T) = A_0 + A_1T + A_2T^2 + A_3T^{-2} \quad (2.17)$$

$$K(T) = K_0 + K_1T + K_2T^2 \quad (2.18)$$

For ferromagnetic phases, the magnetic contribution to the Gibbs energy is given by:

$${}^{\text{magnetic}}G = RTf\left(\frac{T}{T_c}\right)\ln(\beta) \quad (2.19)$$

where T_c is Curie or Neel temperature, and β is the average magnetic momentum in Bohr magnetons. The structure dependent function, $f\left(\frac{T}{T_c}\right)$ is given based on the model for C_p suggested by Inden [26] and Hillert and Jarl [27].

2.2.1.(b) Models for phases with variable compositions

At constant pressure, Gibbs energy of a phase with variable composition is a function of temperature (T) and the amounts of components in the phase (n_i). When the number of components is equal to the number of elements, the amounts of components (n_i) are often expressed by the mole fractions of components (x_i) which is defined as:

$$x_i = \frac{n_i}{N} \quad (2.20)$$

where $N = \sum_i n_i$ is the total number of components. But, there are cases when one prefers to use components other than elements in modeling a phase. In such cases the amounts of components in the phase is often expressed by constituent fraction (or site fraction), y_i .

Gibbs energy of a solution phase, ϕ can be divided in to three parts as:

$$G^\phi = G^{\text{reference}} + G^{\text{ideal}} + G^{\text{excess}} \quad (2.21)$$

where $G^{\text{reference}}$ describes the solution properties relative to the properties of the pure constituents in the same structure, ϕ :

$$G^{\text{reference}} = \sum x_i {}^0G_i^\phi \quad (2.22)$$

G^{ideal} describes the solution properties by assuming random mixing (or ideal mixing) of atoms. For a substitutional solution, all atoms are assumed to mix each other and G^{ideal} is given as:

$$G^{\text{ideal}} = RT \sum x_i \ln x_i \quad (2.23)$$

G^{excess} describes the deviation of the solution properties from ideal mixing by some mathematical expression. Generally the excess Gibbs energy is described by polynomial functions.

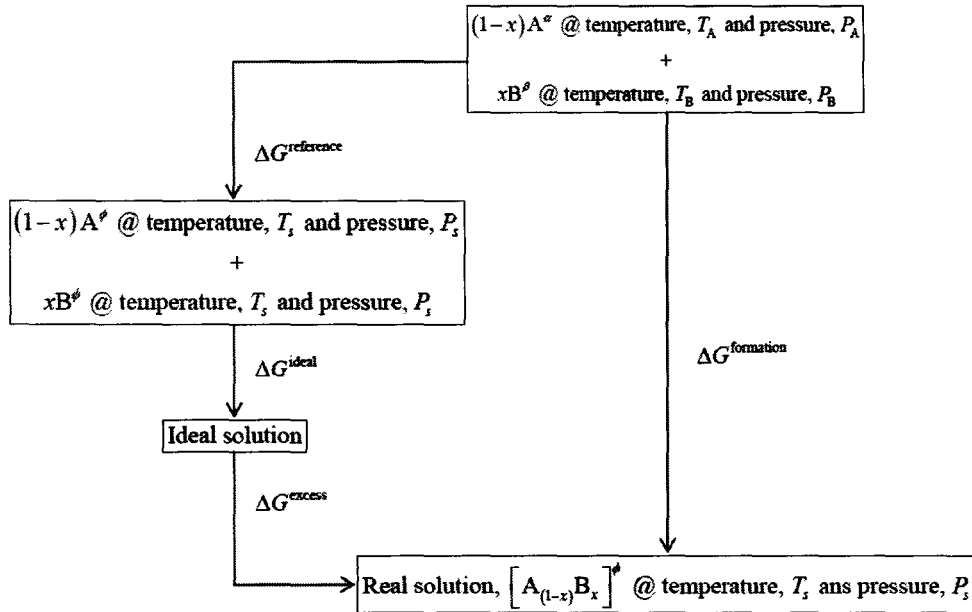


Figure 1: Formation of a real solution $A_{(1-x)}B_x$ of structure ϕ at T_s and P_s

Figure 1 shows the three different Gibbs energy contribution in forming a substitutional solution, $A_{(1-x)}B_x$ in phase, ϕ . When modeling the excess Gibbs energy the following three properties should be satisfied:

$$(i) \Delta G^{\text{excess}}(x=0) = \Delta G^{\text{excess}}(x=1) = 0$$

(ii) Continuous (twice continuous differentiable)

$$(iii) \left[\frac{\partial(\Delta G^{\text{excess}})}{\partial x} \right]_{T,P,x=0} \text{ is finite and } \left[\frac{\partial(\Delta G^{\text{excess}})}{\partial x} \right]_{T,P,x=1} \text{ is finite}$$

In the simplest case one could use Margules polynomials [28]. For a binary system, excess Gibbs energy in the form of Margules polynomials is written as:

$$G^{\text{excess}} = RTx_i x_j \sum_k A_k x_j^k \quad (2.24)$$

where the coefficients, A_k are calculated from activity coefficients of components:

$$\ln \gamma_i = \sum_k a_k x_i^k \quad (2.25)$$

where γ_i is the activity coefficient of component i . One of the limitations of Margules polynomials in expressing the excess Gibbs energy is that the coefficients, A_k in (2.24) are not transformed directly to higher order systems [29].

The frequently used polynomial form to describe the excess Gibbs energy is called Redlich-Kister polynomial [30]. For a binary system, excess Gibbs energy in the form of Redlich-Kister polynomial is written as:

$$G^{\text{excess}} = x_i x_j \sum_{\nu=0}^k {}^{\nu}L_{ij} (x_i - x_j)^{\nu} \quad (2.26)$$

In (2.26) the Redlich-Kister binary interaction parameter ${}^vL_{ij}$ is frequently a linear function of temperature:

$${}^vL_{ij} = {}^va_{ij} + {}^vb_{ij}T \quad (2.27)$$

One of the advantages of using Redlich-Kister polynomials to describe the excess Gibbs energies is that they can be easily extended to multicomponent systems without changing the shape of the excess Gibbs energy of the binary system in the multicomponent system [31].

There are various geometric extrapolation methods available to calculate ternary excess Gibbs energy. Some of these methods are illustrated in Figure 2. The excess Gibbs energy at the ternary point P is estimated from the binary excess Gibbs energies evaluated at the binary points a, b, and c:

$$G_{123(P)}^{\text{excess}} = x_1x_2G_{12(a)}^{\text{excess}} + x_2x_3G_{23(b)}^{\text{excess}} + x_1x_3G_{13(c)}^{\text{excess}} + (\text{ternary terms}) \quad (2.28)$$

The ternary terms in (2.28) are polynomial terms that are rarely used to fit the ternary experimental data.

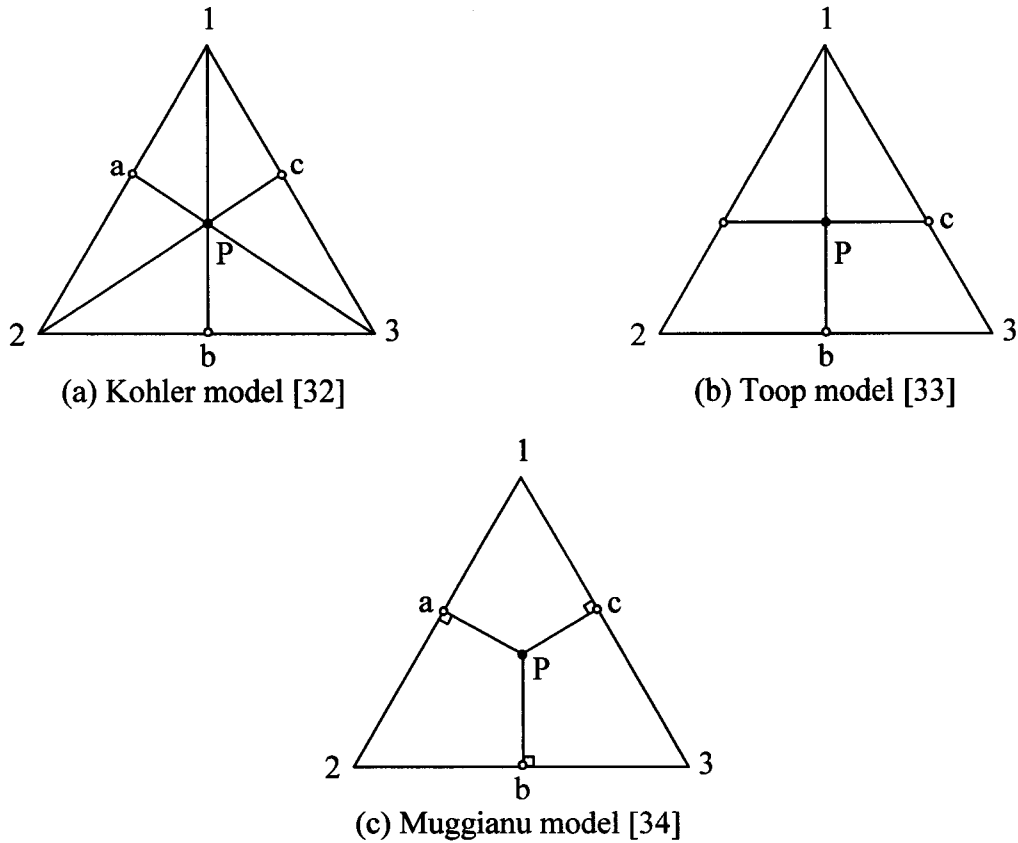


Figure 2: Some ternary extrapolation methods

When modeling a solid solution one could use models that describe its structure information. For example, the sublattice model uses the crystallographic information of the solid solution to introduce sublattices. Let us take a simple example where the solid phase, ϕ is assumed having two sublattices and two different constituents on each one. In this case, the sublattices of the phase, ϕ is represented by the formula, $(A, B)_a(C, D)_c$, where a and c are the numbers of sites in the first and second sublattice, correspondingly. Usually a and c are normalized: $a + c = 1$. The Gibbs energy of this phase is:

$$G_m^\phi = \sum_i \sum_{<j} y_i^1 y_j^2 G_{ij}^\phi + aRT \sum_i y_i^1 \ln y_i^1 + cRT \sum_j y_j^2 \ln y_j^2 \quad (2.29)$$

The above Gibbs energy equation (2.29) is called the ‘compound energy’ model [35].

Generally liquid phase in many metallic systems is modeled by random substitutional model with Redlich-Kister excess Gibbs energy. When liquids tend to exhibit short-range order (SRO), *i.e.*, the local arrangement of atoms, the associate solution model [36] is used to describe their Gibbs energy functions. For molten salts and liquids contain oxygen are often modeled by partially ionic liquid model [37].

Models for handling SRO are associate solution model, quasi-chemical model, and cluster –variation method. An in-depth discussion on different models can be found in [31].

2.2.2 Optimization tools

Once the models for the phases are selected, available experimental thermodynamic data and phase diagram data are collected based on their reliability and accuracy. Then these experimental data are used to evaluate the model parameters or adjustable coefficients in the analytical expressions of phases using optimization tools such as BINGSS [38, 39], TERGSS [39], PARROT [40] and OPTISAGE [41].

The least-squares method is used for assigning statistically best values to the adjustable coefficients in the analytical expressions of phases. The purpose of the least squares method is to fit the adjustable coefficients of an analytical expression to experimental values. To find statistically optimum values of the adjustable coefficients, firstly, a set of approximate values are assigned to the adjustable coefficients and using

the analytical expressions different types of thermodynamic and phase diagram data are calculated. Secondly, the error is defined as

$$\text{error} = (\text{Experimental value} - \text{Calculated value}) \times p \quad (2.30)$$

where p is the weighting factor. Finally, the optimum values for the adjustable coefficients are obtained by minimizing the squared error:

$$\sum_{i=1}^n [(\text{error})_i]^2 = \text{minimum} \quad (2.31)$$

To illustrate the least squares method further, let us consider the following example [31]. Assume that there are measured quantities of M_i .

$$M_i = F_i(\vec{x}_i), \quad i = 1, \dots, n \quad (2.32)$$

where \vec{x}_i is a vector of experimental conditions, $\dim(\vec{x}_i) = Q_i$. Error associated with measured quantities and experimental conditions are $\Delta F_i(\vec{x}_i)$ and $\Delta \vec{x}_i$ respectively. Now let us assume that the measured M_i are calculable through (2.33)

$$M_i = \hat{F}_i(\vec{x}_i, \vec{C}), \quad i = 1, \dots, n \quad (2.33)$$

where \vec{C} is a vector of unknown coefficients, $\dim(\vec{C}) = m$. If $n > m$, generally it is not possible to get the vector of unknown coefficients \vec{C} using (2.33). In such cases, the vector of unknown coefficients \vec{C} can be calculated by minimizing the sum of squares of weighted deviations between the measured and calculated quantities. The weighted error between the measured and calculated quantities is given as,

$$E_i = [F_i(\vec{x}_i) - \hat{F}_i(\vec{x}_i, \vec{C})] p_i \quad (2.34)$$

and the weights p_i in (2.34) are calculated as follows assuming $\Delta F_i(\bar{x}_i)$ and $\Delta \bar{x}_i$ are independent

$$p_i = \frac{1}{\left\{ \left[\Delta F_i(\bar{x}_i) \right]^2 + \sum_{q=1}^{q_i} \left[\frac{\partial \hat{F}_i(\bar{x}_i, \bar{C})}{\partial x_{qi}} \Delta x_{qi} \right]^2 \right\}^2} \quad (2.35)$$

Hence, the target function to be optimized to get the best estimation of the vector of unknown coefficients \bar{C} is,

$$\sum_{i=1}^n E_i^2 = \min(\bar{C}) \quad (2.36)$$

From (2.36) one gets the following m equations.

$$\sum_{i=1}^n E_i \cdot \frac{\partial E_i}{\partial C_j} = 0, \quad j = 1, \dots, m \quad (2.37)$$

To solve (2.37), let us employ the first order Taylor series approximation for E_i :

$$E_i(\bar{x}_i, \bar{C}) \approx E_i(\bar{x}_i, \bar{C}_j^0) + \sum_{k=1}^m \left(\frac{\partial E_i}{\partial C_k} \right) \cdot \Delta C_k \quad (2.38)$$

where \bar{C}_j^0 is the initial guess and ΔC_k are the corrections to the coefficients C_k , which can be calculated using (2.37), and (2.38). The substitution of (2.38) in (2.37) results in the following m linear equations for the m unknowns ΔC_k :

$$\left[\left(\sum_{i=1}^n \frac{\partial E_i}{\partial C_j} \cdot \frac{\partial E_i}{\partial C_k} \right) \right]_{m \times m} \cdot [(\Delta C_k)]_{m \times 1} = \left[\left(- \sum_{i=1}^n E_i^0 \cdot \frac{\partial E_i}{\partial C_k} \right) \right]_{m \times 1} \quad (2.39)$$

The above set of equations (2.39) in matrix notation is called “Gaussian normal equations” [31]. The calculation in (2.39) will be repeated until the corrections are below a prescribed limit.

2.2.3 Databases

Databases mainly contain critically assessed unary, binary and ternary thermochemical data for the concerned elements, species, and phases in all the stable and many metastable states from 298.15 K up to their liquid and gaseous states. These data are in stored in SI units.

One of the main motivations behind the thermodynamic assessment is the creation of multicomponent thermodynamic databases. Several binary and ternary thermodynamic assessments are merged to create Multicomponent databases. These databases can be used to calculate the equilibrium amount of phases, their compositions, and transformation temperatures. These calculated values have accuracy close to that of an experimental measurement and hence the database is a valuable tool for planning new experimental work in alloy design when it is compared with the cost of experimental work in multi-component systems.

Some of many different types of thermodynamic databases are namely pure element database also known as unary database, solution database, stoichiometric compound database, semiconductor database, steel database, solders database, etc.

Among all these databases the pure element database is an internationally accepted one. SGTE database [42] is such an internationally accepted pure element database. The database [43] contains pure substances thermochemical data for

approximately 600 chemical species of the trace elements: As, B, Be, Cd, Co, Cr, Ga, Ge, Hg, Ni, P, Pb, Sb, Se, Sn, V and Zn. A semiconductor database for binary III-V systems is presented in [44]. Pelton [45] presented a database for molten salt solution. More useful information on several databases can be found in [46].

In addition to the above-mentioned databases, there are experimental databases used in thermodynamic optimization. These databases contain properly referenced experimental quantities. Each item of experimental information has certain uncertainty.

Some of the important steps to be followed during the creation of a multicomponent database are:

- Collecting necessary thermodynamic assessments
- Making compatibility checks: are the pure element data same in all assessment? is the same phase modeled in the same way in all assessments? are the thermodynamic parameters of all assessments reliable?
- Unifying the phase names: e.g. [31] consider the quaternary Ca-Mg-Fe-O system. CaO in Ca-O system, MgO in Mg-O system, and FeO in Fe-O system are named lime, periclase, and wustite respectively. Since all these three phases have the same NaCl (B1) structure and form a continuous solution in the quaternary Ca-Mg-Fe-O, these three phases are stored under the name “halite” in the database.

In creating a thermodynamic database, merging thermodynamic assessments may result:

- Un - assessed parameters: e.g. ternary interaction parameter. It is reported in [31] that these un - assessed parameters do not have much influence on stable equilibrium calculations thus one can assign estimated values for such parameters.

- Missing parameters: e.g. phases that are ignored during the assessment of a binary system may appear as stable after merging thermodynamic assessments. Different suggestions to find missing parameters were formulated in [31].

Once a database is created, it should be validated by making correct extrapolations to higher order systems. Moreover, a database should be updated time to time with new experimental data and new thermodynamic assessments.

A summary on development of thermodynamic databases can be found in [47].

Many examples of the use of thermodynamic databases are given in [48-50].

2.2.4 Software for thermodynamic optimization

To perform a thermodynamic optimization one should be able to link the models of phases, the minimization engines and the databases together. This is made possible through many available software packages such as Thermo-Calc [51], FactSage [52], PANDAT [53], MTDATA [54], IVTANTHERMO [55], etc.

Thermo-Calc is one of the widely used phase diagram calculating software. In this software the POLY module performs the equilibrium calculations and GES module deals with thermodynamic models, and data treatment. These two modules are built by Jansson [56] and Sundman [47] respectively.

Another phase diagram calculating software FactSage uses the Gibbs energy minimizer, SOLGAXMIX developed by Eriksson [57]. SOLGAXMIX is an extended work of one of Eriksson's previous work SOLGAS [58].

Figure 3 shows how the models of phases, the minimization engines, and the databases are linked together in Thermo-Calc package.

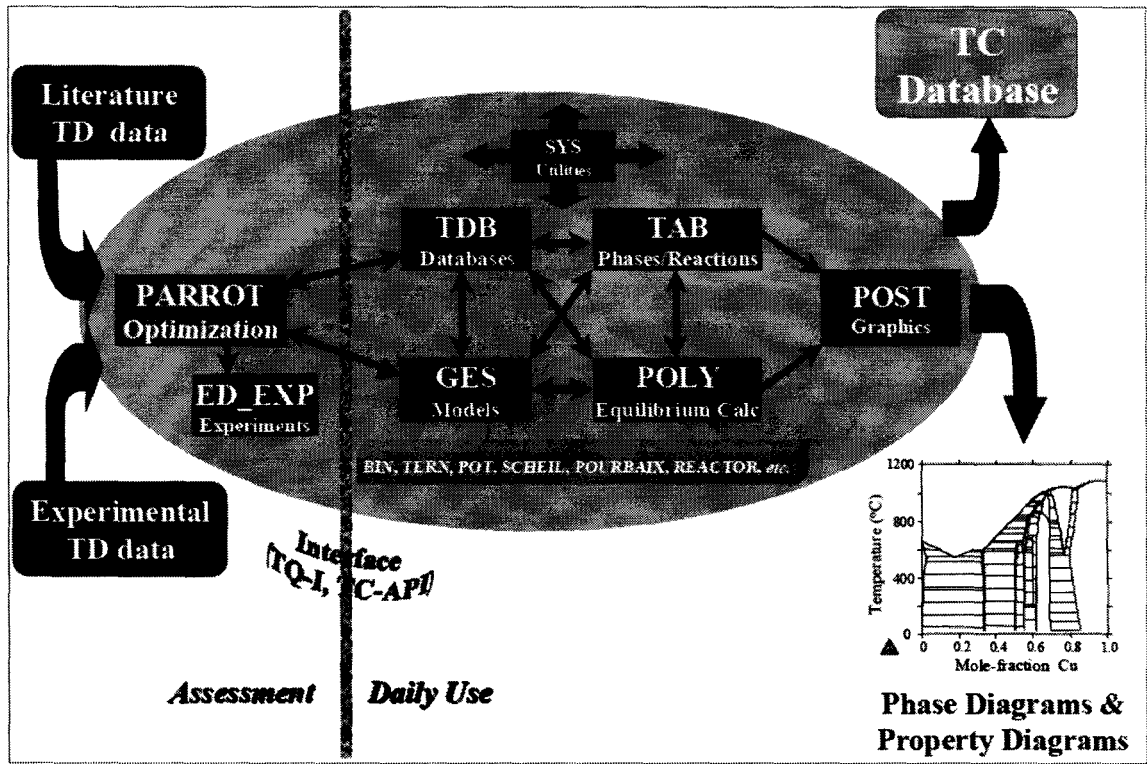


Figure 3: General structure of the Thermo-Calc package [59]

Functions of the modules shown in Figure 3 are given below.

- TDB – for database retrieval and management
- GES – for thermodynamic model handling and data treatments for various phases
- TAB – for thermodynamic property tabulations of phases and reactions
- POLY – for multi-component heterogeneous equilibrium and stepping/mapping calculations
- POST – for post-processing of various phase diagrams and property diagrams
- PARROT – for parameter optimizations in data assessments
- ED_Experimental – for experimental points editing and equilibrium calculations

All the above-mentioned modules are necessary during thermodynamic calculations and predictions.

Thermodynamic software packages are capable of performing numerous thermodynamic and phase diagram calculations such as

- Calculation of phase diagrams: binary, ternary, isothermal, isoplethal
- Calculation of property diagrams: fraction of phase, Gibbs energy, enthalpy, Cp, etc
- Metastable equilibria: Fe-Fe₃C diagram
- Pourbaix diagrams and many other diagrams for aqueous-involving interaction systems: eh Vs pH diagrams
- Scheil-Gulliver-type solidification calculations
- Liquidus surfaces for multi-component alloys
- Thermodynamic factors, driving forces
- Establishment and modification of datasets or databases
- Several more calculations to be found in [60], [61]

2.3 Algorithmic details of thermodynamic optimization

In this section, algorithmic details involved in thermodynamic optimization are presented in four parts. Firstly, details of finding equilibrium state of a system are presented. Then the condition to be set to achieve the equilibrium state is presented. Next, the solution method to evaluate the equilibrium state is presented. Finally, model parameter optimization is presented.

2.3.1 Gibbs energy minimization

Finding the equilibrium state of the system is inevitable when the optimization is being carried out. In thermodynamics, equilibrium state of a system is described through state functions. In equilibrium calculations, the commonly used state function is the Gibbs energy, G which is given by

$$G = U + PV - TS \quad (2.40)$$

Generally U in (2.40) is replaced by another state function H and given by

$$H = U + P \cdot V \quad (2.41)$$

A system at constant temperature (T) and pressure (P) with fixed amounts of components is said to be at equilibrium when the Gibbs energy reaches its minimum. In many thermodynamic calculations instead of number of moles, N_i , the mole fraction, x_i is used in Gibbs energy equations.

A number of phases may exist in a thermodynamic system. Among these phases, only those, which are in equilibrium, may contribute to the total Gibbs energy of the system G through

$$G = \sum_{\phi} m^{\phi} \cdot G_m^{\phi} \quad (2.42)$$

where m^{ϕ} is the amounts of the phase ϕ and G_m^{ϕ} is the molar Gibbs energy of each phase. Hence, for a thermodynamic system at equilibrium one may write

$$G_{\min} = \min \left[\sum_{\phi} m^{\phi} \cdot G_m^{\phi} (T, p, x_i^{\phi}) \right] \quad (2.43)$$

2.3.2 Conditions of equilibrium

Now from (2.43), it is clear that to find the equilibrium state of a system the variables T, P, x_i^ϕ, m^ϕ are to be evaluated at G_{\min} . These variables at minimum Gibbs energy can be evaluated by setting the first derivatives of G with respect to its variables to zero.

To find the G_{\min} at a known temperature and pressure, we need additional i equations to eliminate m^ϕ and N_i . The overall mole fraction of the component, $x_i = \sum_{\phi} m^\phi x_i^\phi$, the mole fractions, $x_i = N_i/N$ and the total amount, $N = \sum N_i$.

The i additional equations are obtained through the equilibrium chemical potential (partial molar Gibbs energy) equations of each component. They are,

$$G_i^\phi(T, p, x_i^\phi) = G_i^\gamma(T, p, x_i^\gamma) \quad (2.44)$$

where $i = 1, \dots, c$, $\phi = 1, \dots, (p-1)$, and $\gamma = (\phi+1), \dots, p$.

If the phase ϕ is to be described using a sublattice model given in (2.29), then instead of mole fractions x_i^ϕ site fractions $y_e^{(s,\phi)}$ is to be used in (2.43). The site fraction $y_e^{(s,\phi)}$ refers the fraction of component e of the phase ϕ on the sublattice s . Due to the interrelationship between x_i^ϕ and $y_e^{(s,\phi)}$ in the above mentioned situation it is not very easy to use the equations in (2.44) to find the equilibrium state. Eriksson [58] and Hillert [62] eased this situation via Lagrange multiplier method. In their method the following three conditions are subjected in the minimization of G given in (2.43).

1. There is no change in the total amount of each component:

$$\sum_{\phi} m^{\phi} \sum_s a^{(s)} \sum_k b_{e,i}^{(s,\phi)} \cdot y_e^{(s,\phi)} - N_i = 0 \quad (2.45)$$

Where $b_{e,i}^{(s,\phi)}$ - the stoichiometry of the component e in the sublattice s in ϕ phase, $a^{(s)}$ - the site fractions of sublattice s assigned to all sites of the phase.

2. The sum of all site fractions in each sublattice is equal to unity:

$$\sum_e y_e^{(s,\phi)} - 1 = 0 \quad (2.46)$$

3. Each phase remains neutral (uncharged):

$$\sum_s a^{(s)} \sum_e \tau_e^{(s,\phi)} \cdot y_e^{(s,\phi)} = 0 \quad (2.47)$$

Where $\tau_e^{(s,\phi)}$ - the charges of the components e in the sublattice s in the ϕ phase.

Now let us write the target function to be minimized (Λ) in the Lagrange multiplier method:

$$\begin{aligned} \min \left[\Lambda \left(T, p, N_i, y_e^{(s,\phi)}, m^{\phi}, \lambda, \mu, \delta \right) \right] = & G \left(T, p, y_e^{(s,\phi)} \right) + \lambda f_1 \left(m^{\phi}, y_e^{(s,\phi)}, N_i \right) \\ & + \mu f_2 \left(y_e^{(s,\phi)} \right) + \delta f_3 \left(y_e^{(s,\phi)} \right) \end{aligned} \quad (2.48)$$

Where λ, μ, δ are Lagrange multipliers and f_1, f_2, f_3 are the LHS of equations (2.45), (2.46), (2.47) respectively. To get the Λ_{\min} given in (2.48), the first derivatives of Λ with respect to the unknowns is set to zero. At the end of this process one gets a set of non linear equations with the unknowns $T, p, N_i, y_e^{(s,\phi)}, m^{\phi}, \lambda, \mu,$ and δ . The method to solve these sets of equation is discussed in the section 2.3.3.

2.3.3 Finding the equilibrium conditions

The equilibrium state of a system can be derived by solving the non linear equations derived for the G_{\min} in section 2.3.2. There are several root-finding algorithms available to find the solution from a set of equations. Some of them are, namely, bisection method, Newton–Raphson method, Halley's method, false position method, and Brent's method.

The research work presented in this thesis is accomplished using Thermo-Calc which uses the Newton–Raphson method in solving system of equations. Hence, in this section the Newton–Raphson method is discussed in detail.

Newton's method is an iterative method of finding the root of a function of single variable through some definite procedure. The Newton–Raphson method is the extended version of the Newton's method in solving multiple variable functions. The Newton's method is reviewed with the help of Figure 4.

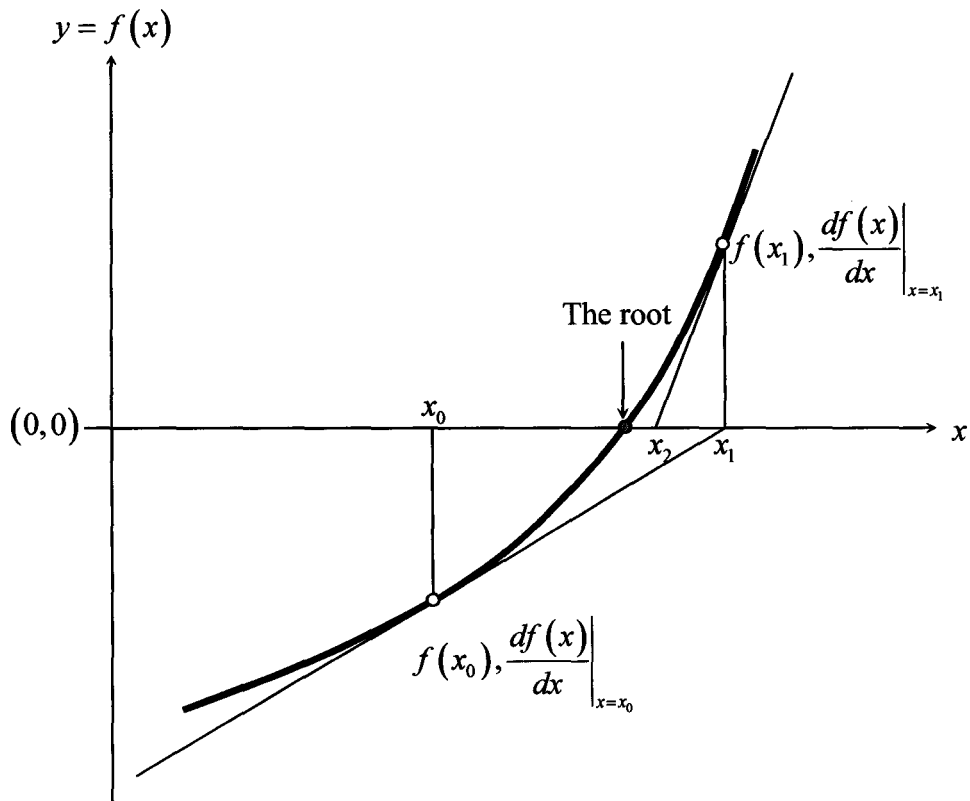


Figure 4: Newton's method

Firstly an initial guess for the root of the function $f(x)$ is taken as x_0 . Then at $x = x_0$ the functions numerical value $f(x_0)$ and its first derivative $\left. \frac{df(x)}{dx} \right|_{x=x_0}$ are calculated.

Secondly another guess for the root is made as x_1 , which is the intersection between the gradient $\left. \frac{df(x)}{dx} \right|_{x=x_0}$ and the x axis. Where,

$$\left. \frac{df(x)}{dx} \right|_{x=x_0} = f'(x_0) = \frac{f(x_0) - 0}{(x_0 - x_1)} = \frac{-f(x_0)}{(x_1 - x_0)} \quad (2.49)$$

and

$$x_1 = x_0 - \frac{f(x_0)}{f'(x_0)} \quad (2.50)$$

This procedure is repeated until the value of the function $f(x)$ becomes less than a pre-selected limit ε . For any $(i+1)^{\text{th}}$ iteration, the first derivative of the function and the root is given by,

$$\left. \frac{df(x)}{dx} \right|_{x=x_{i+1}} = f'(x_{i+1}) = \frac{-f(x_i)}{(x_{i+1} - x_i)} \quad (2.51)$$

and

$$x_{i+1} = x_i - \frac{f(x_i)}{f'(x_i)} \quad (2.52)$$

respectively.

The Newton iteration will converge to the root of $f(x)$, if x_i is in an interval $[a, b]$ such that:

- $f(a)f(b) < 0$
- f' is not zero in $[a, b]$
- f'' does not change sign in $[a, b]$
- $f(a)/f'(a) < (b-a)$ and $f(b)/f'(b) < (b-a)$

Usually Newton's method converges very rapidly. However, there are cases when the method diverges. Three of such cases from [63] are illustrated in Figure 5-Figure 7.

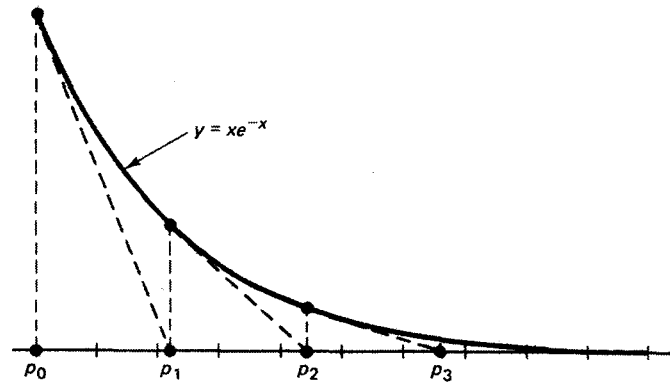


Figure 5: $f(x) = x \exp(-x)$ produces a divergent sequence

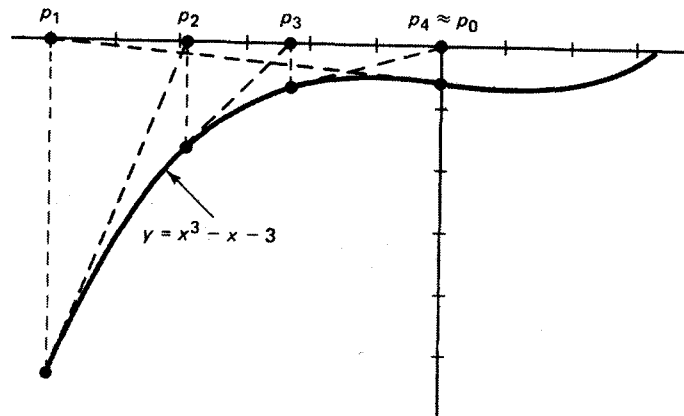


Figure 6: $f(x) = x^3 - x - 3$ produces a cyclic sequence

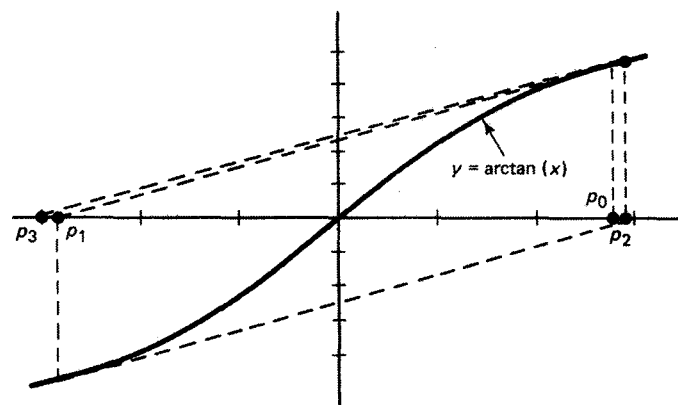


Figure 7: $f(x) = \arctan(x)$ produces divergent oscillations

Now the Newton-Raphson method in solving N functional relations to be zeroed, involving N variables of x_i , $i = 1, \dots, N$ could be discussed. Let

$$f_i(x_1, x_2, \dots, x_N) = 0 \quad i = 1, 2, \dots, N \quad (2.53)$$

Now to solve the set of equation in (2.53) we need the first derivatives of all these functions. To find that, let us expand each of the functions f_i in Taylor series and truncate them to the linear terms we get

$$f_i(\mathbf{x} + \delta\mathbf{x}) = f_i(\mathbf{x}) + \sum_{j=1}^N \frac{\partial f_i}{\partial x_j} \delta x_j \quad (2.54)$$

where $\mathbf{x} = \begin{pmatrix} x_1 \\ x_2 \\ \vdots \\ x_N \end{pmatrix}$.

From (2.54) we get a set of linear equations similar to the ones given in (2.52):

$$\sum_{i,j=1}^N \alpha_{ij} \delta x_j = \beta_i \quad (2.55)$$

where

$$\alpha_{ij} = \frac{\partial f_i}{\partial x_j}, \quad \beta_i = -f_i \quad (2.56)$$

The matrix equations given in (2.55) is solved by LU decomposition and the consecutive guesses of the roots are obtained through

$$x_i^{\text{new}} = x_i^{\text{old}} + \delta x_i \quad (2.57)$$

and this procedure is iterated until it reaches to a certain terminating condition.

2.3.4 Model parameter optimization

During a thermodynamic optimization not only the equilibrium state of a system is calculated but the coefficients of the phase models of all the existing phases are also evaluated. As explained in section 2.2.2 the coefficients of the phase models are evaluated via least squares method by minimizing the weighted square error between the calculated and experimental thermodynamic quantities.

In other words the target function to be minimized here is

$$\min_{\vec{C}} F(\vec{C}) = \sum_{i=1}^{\text{number of measurements}} w_i \left\{ \begin{array}{l} (\text{measured property})_i \\ -(\text{calculated property})_i(\vec{x}_i^{\text{exp}}, \vec{C}) \end{array} \right\}^2 \quad (2.58)$$

In (2.58), the weighting factor w_i is incorporated in the target function to compare the errors of the different types of measurements and it is calculated as follows. Suppose a measured property Y is a function of s and r then,

$$w = \frac{1}{(\Delta Y)^2 + \left(\frac{\partial Y}{\partial s} \Delta s\right)^2 + \left(\frac{\partial Y}{\partial r} \Delta r\right)^2} \quad (2.59)$$

Since the results presented in this thesis are calculated by Thermo-Calc, let us see how the errors are fed during Thermo-Calc calculations. There are two ways to feed the errors in experimental conditions (independent state variables) into the Thermo-Calc optimizer PARROT. They are,

- (i) Specifying the errors in experimental conditions in the POLY module. In this case, equilibria are calculated with the experimental values of independent state variables.

- (ii) Optimizing the “true” value of the experimental conditions using one of the defined variables as the condition.

Both methods can be transformed into a least squares problem shown in (2.58) and the optimized parameters are found using the subroutine VA05A, a numerical subroutine from the Harwell Subroutine Library (HSL).

It is clear from (2.58) that the traditional CALPHAD type thermodynamic calculations are based on experimental observations. However, there are situations where experimental investigations are not possible. For example it is difficult to get experimental information of metastable equilibria, or on unknown phases especially in developing new materials. During such situations one could evaluate thermodynamic quantities using first principles calculations. Some impressive results for thermodynamic calculations using first principle calculations can be found in [64-68].

From the algorithmic details presented so far, it can be said that the present day CALPHAD technique is based on least squares optimization, where the optimal values of the model parameters are evaluated by providing the best match between the calculated and experimental quantities. In other words, thermodynamic optimizations performed by the present day thermodynamic software packages guarantee only the accuracy of thermodynamic calculations.

However, the fact that all experimental data have been accurately reproduced does not imply that the Gibbs energies are suitable for extrapolation of phase boundaries beyond a range of conditions within which, the experiments were carried out. In the

literatures we can find numerous examples of such unreliable thermodynamic calculations and extrapolations, which will be discussed in detail in chapter 3.

2.4 Conclusions

The present day thermodynamic optimization is an un-constrained non-linear least squares optimization. Thermodynamic calculations performed using the traditional Calphad technique is reliable within the regions of experimental data. However, such calculations out side the experimental data are not always reliable.

CHAPTER 3

Post-optimization artifacts

3.1 What are artifacts?

The traditional CALPHAD method guarantees the accuracy of the phase models within the region where experiments were carried out. However, this does not guarantee a trustworthy extrapolation in the regions of no experimental data. Keeping this circumstance in mind, it is important to know how the success of a thermodynamic optimization is determined.

A thermodynamic optimization is said to be successful when its phase diagram and thermodynamic property diagram(s) calculations result in a good agreement with experimental points, characteristic shapes such as concavity and convexity of phase boundaries and thermodynamic properties (and their continuations).

In a number of published thermodynamic optimizations in journals such as *Calphad*, *Journal of phase equilibria and diffusion*, *International journal of materials research*, and *Metallurgical and materials transactions A* erroneous extrapolations were later discovered. Such erroneous extrapolations were named post optimization artifacts.

3.2 Classifications of artifacts

Artifacts encountered up to date can be categorized under two major types. They are,

1. Non-existing and erroneous phase equilibria
2. Suspicious temperature and composition dependencies of properties

Further, non-existing and erroneous phase boundaries can be subdivided into three kinds.

They are,

- a. Non-real inverted miscibility gaps in the liquid phase at high-temperatures
- b. Excessive number of inflection points on phase boundaries/ undulate phase boundaries
- c. Low-temperature phase becomes stable again at high-temperature

A categorization of possible artifacts is given in [69-70].

3.2.1 Non-existing and erroneous phase boundaries

3.2.1.(a) Non-real inverted miscibility gaps in the liquid phase at high-temperatures

The first and the most frequently observed artifact of this category is the non-real inverted miscibility gap. It is likely that there are systems in which an inverted miscibility gap exists. Here, however, the term is exclusively used for specifying situations when a real liquid phase is not prone to separation, while its model (*i.e.* an expression describing how its molar Gibbs energy depends on temperature and composition) predicts that the liquid phase is internally unstable at elevated temperatures and thus decomposes into two solutions having different compositions.

The occurrence of this kind remains un-noticed during the optimization due to their appearance at very high-temperatures in most cases. However, there are cases where inverted miscibility gaps predicted at fairly low-temperatures compared to the liquidus of the system optimized.

A decade ago, this problem was not paid much attention to mainly because at that time dedicated efforts were needed for catching a defective thermodynamics of the liquid

phase. The development and a subsequent widespread usage of PANDAT [71-73] drastically changed the situation, because in contrast to other competing programs, it had a built-in ability to detect faulty thermodynamic models. A rapidly growing number of assessed systems in which inverted miscibility gaps (as well as other types of post-assessment phantoms) were revealed by PANDAT.

The non-real inverted miscibility gaps are usually observed when the excess Gibbs energy of the liquid phase is modeled using a linear temperature dependent Redlich-Kister interaction parameters L_i . For example, let us consider the excess Gibbs energy of a binary liquid A-B,

$$\Delta^E G^L = x_A x_B \sum_{i=0}^n L_i (x_A - x_B)^i \quad (3.1)$$

where L_i is the i^{th} interaction parameter of the components A and B which is given by,

$$L_i = a_i - b_i T \quad (3.2)$$

Moreover, the excess Gibbs energy is related to the enthalpy of mixing (ΔH^L), excess entropy of mixing ($\Delta^E S^L$), and the excess heat capacity of mixing ($\Delta^E C_p^L$) through the following expressions.

$$\Delta^E G^L = \Delta H^L - T \Delta^E S^L \quad (3.3)$$

$$\Delta H^L = \Delta H_0^L + \int_{T=0}^T \Delta^E C_p^L(T) dT \quad (3.4)$$

where ΔH_0^L is the enthalpy of mixing at $T = 0K$

$$\Delta^E S^L = \Delta^E S_0^L + \int_{T=0}^T \frac{\Delta^E C_p^L(T)}{T} dT \quad (3.5)$$

where $\Delta^E S_0^L$ is the excess entropy of mixing at $T = 0K$. From (3.3)-(3.5) $\Delta^E G^L$ can be written as,

$$\Delta^E G^L = \Delta H_0^L + \int_{T=0}^T \Delta^E C_p^L(T) dT - T \left[\Delta^E S_0^L + \int_{T=0}^T \frac{\Delta^E C_p^L(T)}{T} dT \right] \quad (3.6)$$

Now by comparing (3.1) and (3.6) L_i can be written as,

$$L_i = h_{0i} + \int_{T=0}^T c_i(T) dT - T \left[s_{0i} + \int_{T=0}^T \frac{c_i(T)}{T} dT \right] \quad (3.7)$$

where h_{0i} , s_{0i} , and $c_i(T)$ are coefficients to be evaluated during optimization. From

(3.1) and (3.7), for a regular solution phase, the excess Gibbs energy $\Delta^E G^L$ is written as,

$$\Delta^E G^L = x_A x_B L_{00} = x_A x_B (h_{00} - s_{00} T) \quad (3.8)$$

According to Kaptay [74] h_{00} and s_{00} should have the same sign. Hence, when both h_{00}

and s_{00} are negative, at high temperatures, $\Delta^E G^L$ reaches positive value. Due to this

positive value of $\Delta^E G^L$ inverted miscibility gap appears at high temperature. This

situation is illustrated in Figure 8.

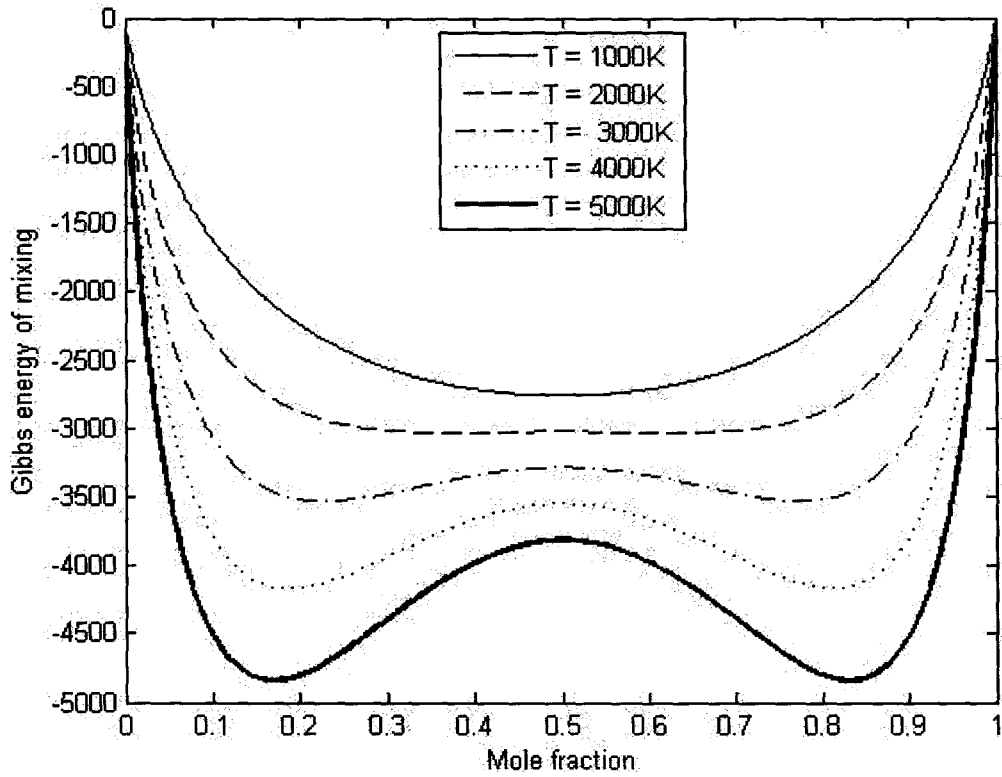


Figure 8: A plot of Gibbs energy of mixing Vs Mole fraction for parameters $h_{0i} = -10000$ and $s_{0i} = -22$ at different temperatures

To find the lower critical temperature of this inverted miscibility gap, let us consider the Darken's stability condition, that is,

$$\frac{\partial^2 (\Delta^M G^L)}{\partial (x_B)^2} = 0 \quad (3.9)$$

where $\Delta^M G^L$ is the Gibbs energy of mixing of the liquid phase. The expression (3.9) can be further expanded as,

$$\frac{\partial^2 (\Delta^{id} G^L + \Delta^E G^L)}{\partial (x_B)^2} = 0 \quad (3.10)$$

where

$$\Delta^{id}G^L = RT[x_A \ln x_A + x_B \ln x_B] \quad (3.11)$$

From (3.8), (3.10), and (3.11) we get the critical temperature of the inverted miscibility gap T_c ,

$$T_c = \frac{2h_{00}}{\left(\frac{R}{x_A x_B} + 2s_{00}\right)} \quad (3.12)$$

Further, $T_{c,\min}$ is obtained when $x_A = x_B = 0.5$. That is,

$$T_{c,\min} = \frac{h_{00}}{2R + s_{00}} \quad (3.13)$$

From the above analysis it can be seen that the inverted miscibility gap is predicted with the lower critical temperature given in (3.13) when the excess Gibbs energy of the liquid phase is described by a linear temperature dependent interaction parameter.

Chen *et al.* [75] looked for the above-described thermodynamic artifact in previous thermodynamic assessments using PANDAT [53], which is able to detect the inverted miscibility gap without using any information about its location in the phase diagram. They presented seven such thermodynamic assessments. They are Co-Mo [76], Si-M [77], Al-Mo [78], Al-W, Al-Nd, Fe-Si, and Sn-Zr [79].

Kaptay [74] pointed to another thermodynamic assessment [80] on Cd-X [X=Y, Ce, La, Pr, Nd, Gd, U, Np, Pu] binary systems, which predicts inverted miscibility gaps in all six binary assessments. Kevorkov *et al.* [81] re-assessed the Mg-Si system whose previous assessments [82, 83] predicted the inverted miscibility gap. Another

thermodynamic re-assessment by Grolier and Schmid-Fetzer [84] revealed the prediction of inverted miscibility gap in the Pt-Sn system using the description of Su *et al.* [85].

In addition to the above pointed examples, the following example is from the author's own thermodynamic assessment. In the author's first publication [86], the Mg-Sb system was assessed using the interaction parameters in the form of (3.2). Later, it was discovered that the evaluated thermodynamic description for the liquid Mg-Sb phase predicts two inverted miscibility gaps at high temperatures.

Since looking for this type of artifact is a time consuming task not all thermodynamic assessments that predict high temperature inverted miscibility gap are reported here. Some calculated phase diagrams from those assessments reported in this section that predict high temperature inverted miscibility gap are illustrated in Figure 9- Figure 14.

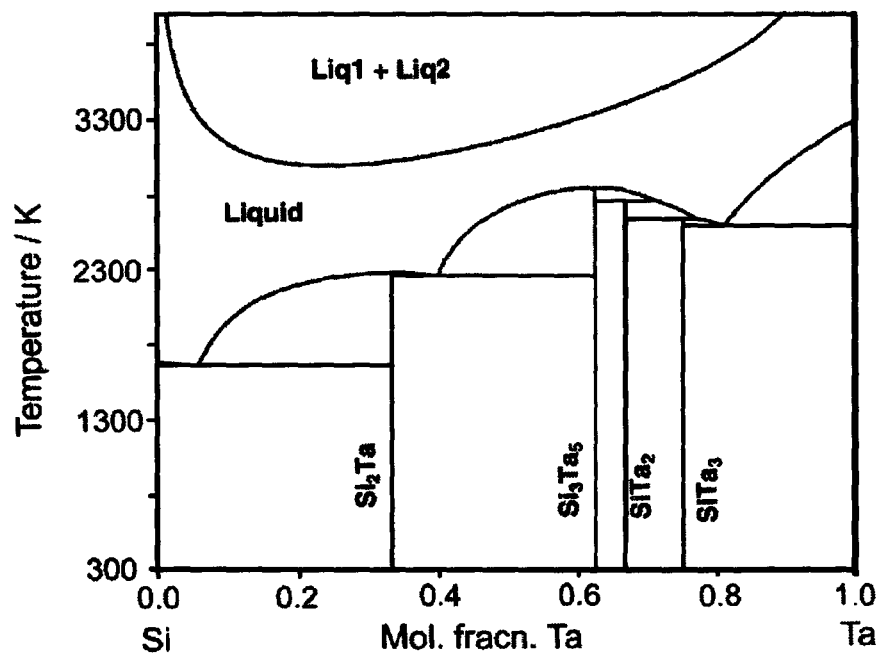


Figure 9: Calculated Si-Ta binary phase diagram using the parameters of [77] by Chen *et al.* [75]

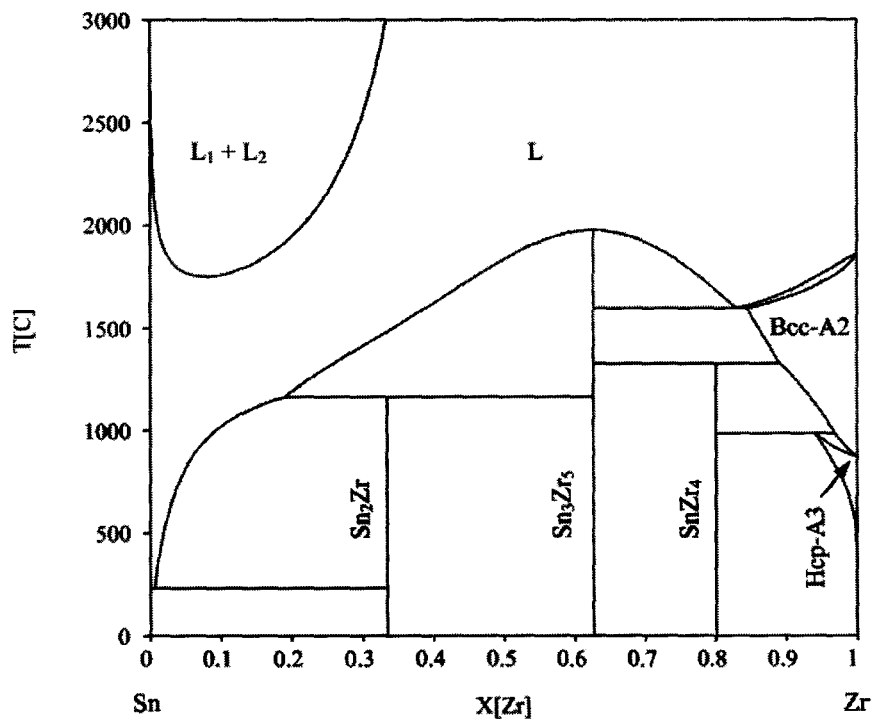


Figure 10: Calculated Sn–Zr phase diagram using a thermodynamic description published in the literature [79] by Chen *et al.* [75]

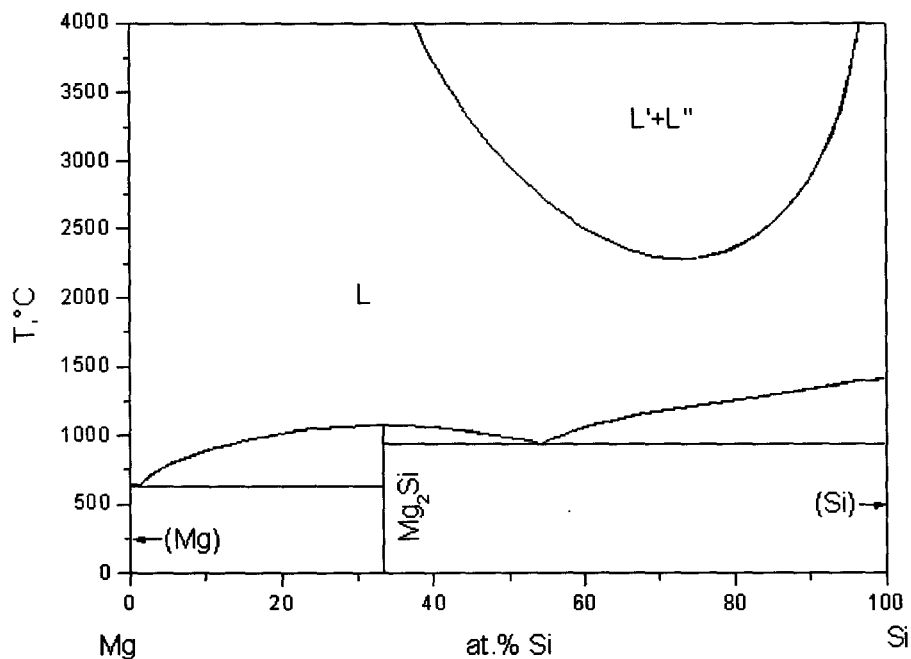


Figure 11: Calculated Mg–Si phase diagram using the parameters of [82] by Kevorkov *et al.* [81]

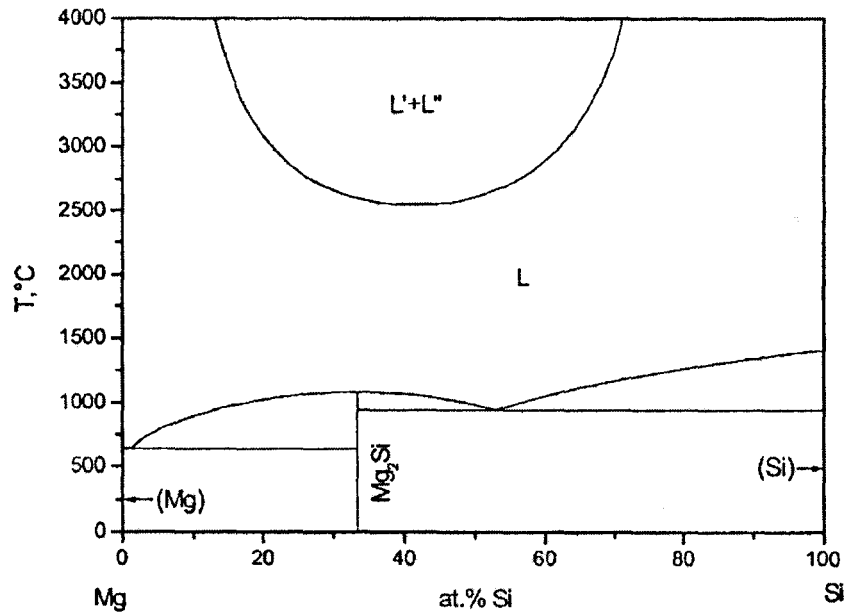


Figure 12: Calculated Mg-Si phase diagram using the parameters of [83] by Kevorkov *et al.* [81]

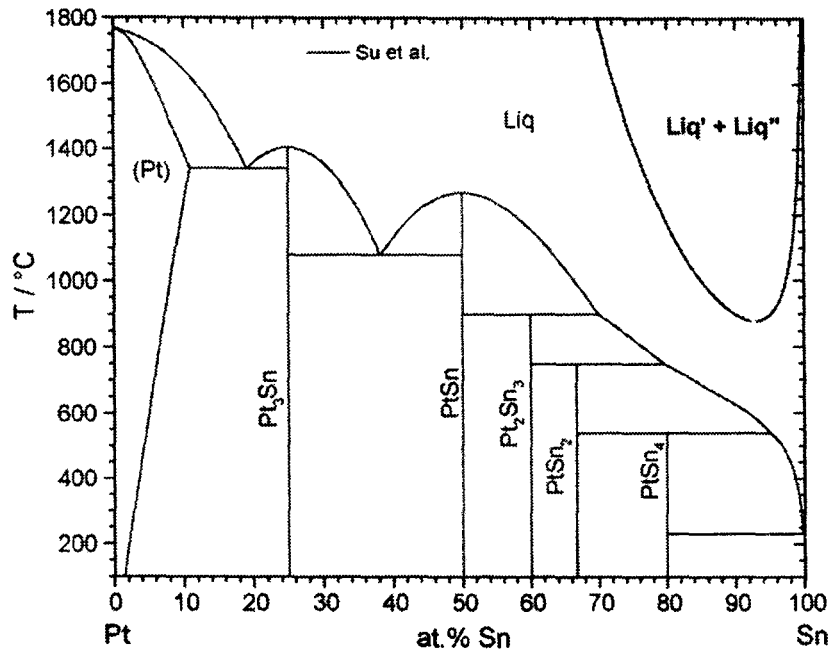


Figure 13: Calculated phase diagram of the Pt-Sn system using the parameters of [85] by Grolier and Schmid-Fetzer [84]

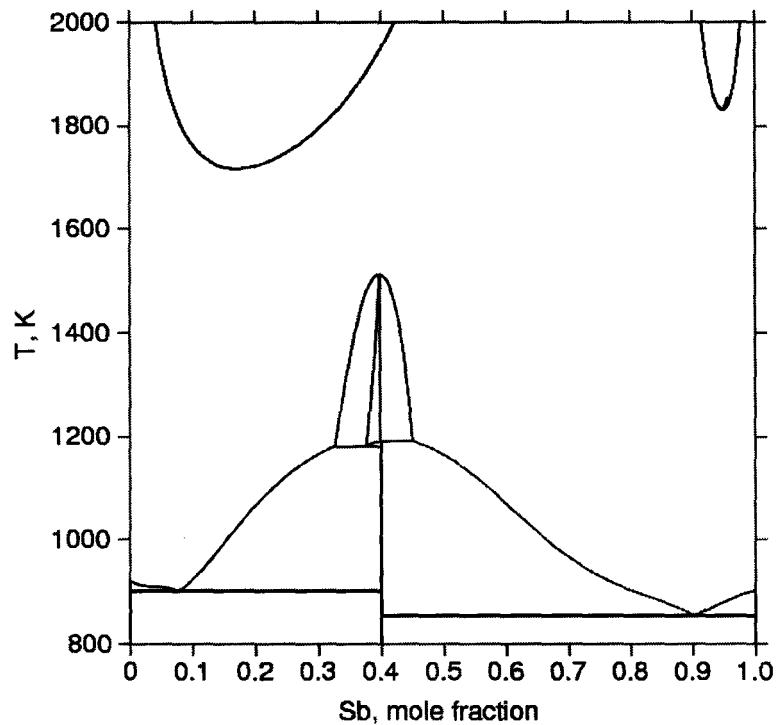


Figure 14: Calculated Mg-Sb phase diagram using the parameters of [86]

3.2.1.(b) Excessive number of inflection points on phase boundaries/ undulate phase boundaries

The second most frequent artifact is the excessive number of inflection points on phase boundaries (also referred as undulate phase boundaries). When dealing with this kind of artifact one has to be very cautious about real inflection points which reflect the existence of meta-stable equilibrium of a phase. For example, in Figure 15 the inflection point on the liquidus between 40 - 80 atomic percent of Na corresponds to the metastable equilibrium of the liquid phase shown in dashed line below the liquid phase boundary.

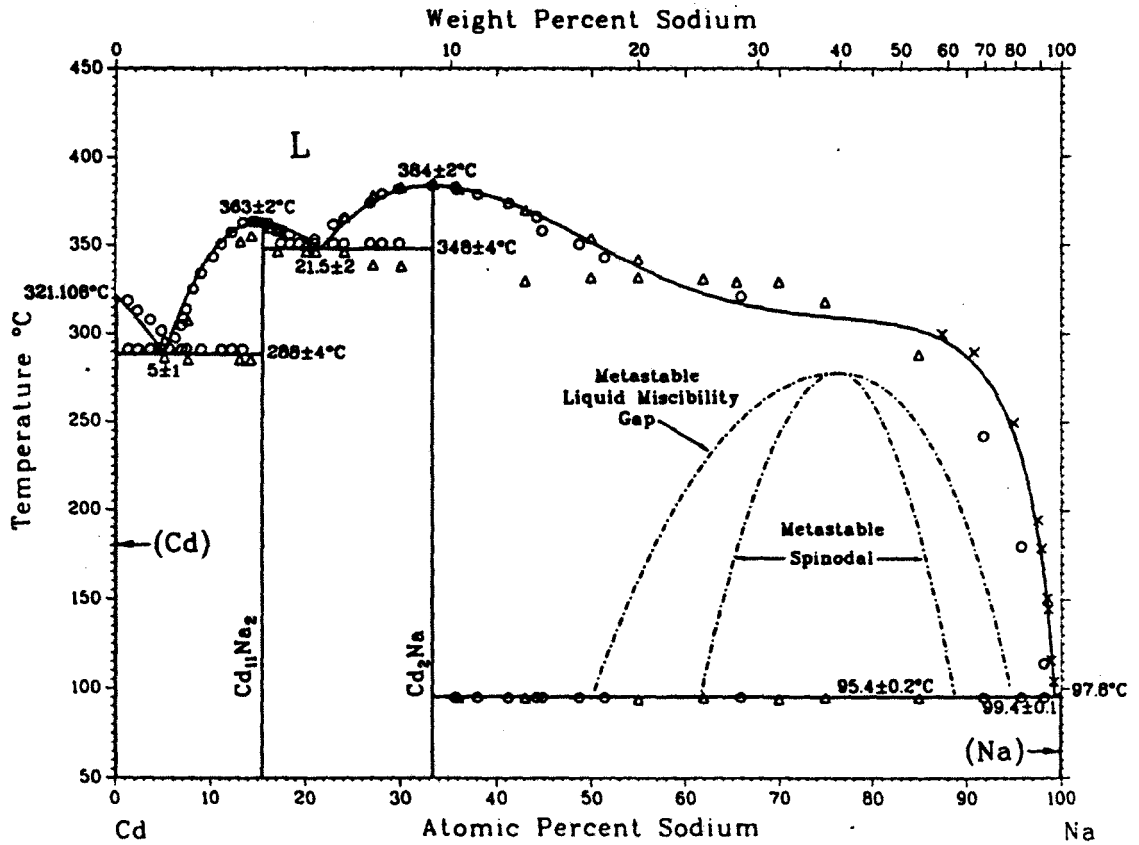


Figure 15: Calculated Cd-Na phase diagram using the thermodynamic descriptions of [87] (extracted from [88])

This example shows the real existence of undulate phase boundary. Similar liquidus topology is observed in Sn - Zn and In - Zn systems. The phase diagrams for these two binary systems are given in Figure 16 and Figure 17 respectively.

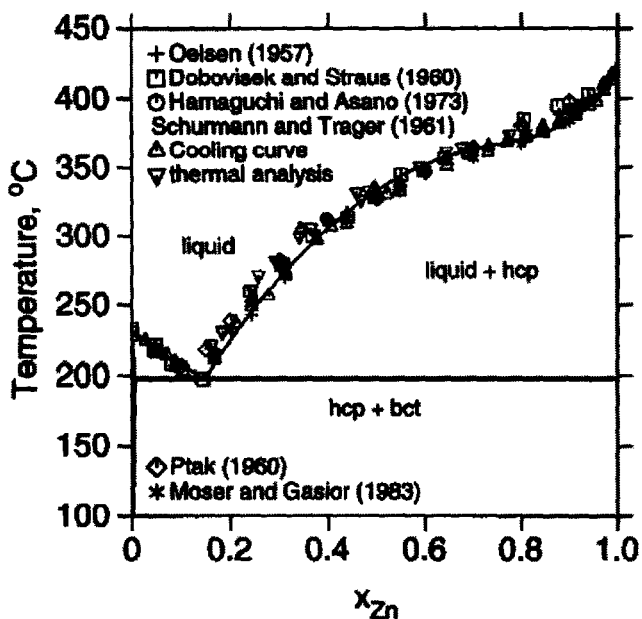


Figure 16: Calculated phase diagram of the Sn-Zn system by [89]

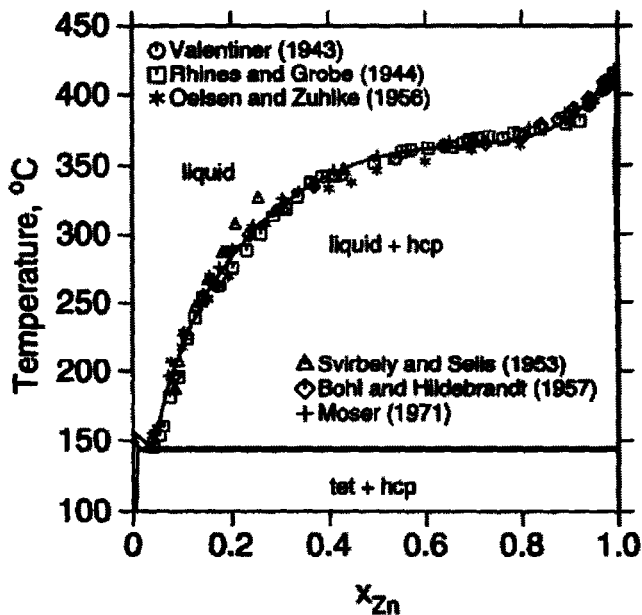


Figure 17: Calculated phase diagram of the In-Zn system by [89]

The topological feature of flat liquidus, which exhibit inflection point on it, can be explained through Figure 18.

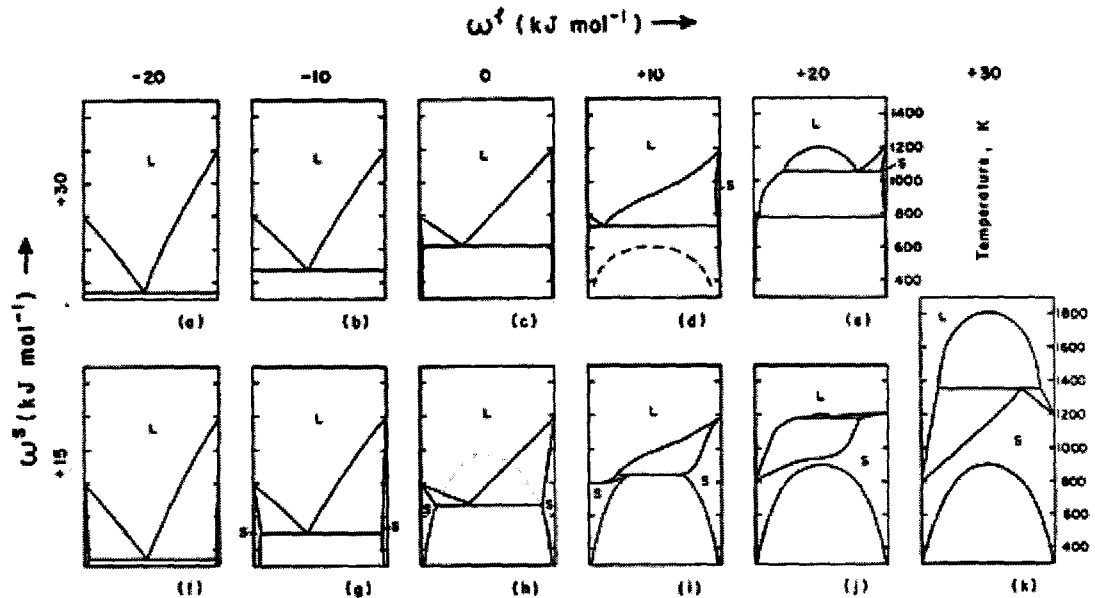


Figure 18: Topological changes in the phase diagram for a system A-B with regular solid and liquid phases [90]

Figure 18 shows phase diagrams of an imaginary A-B system. The thermodynamic data used in [90] to construct the above set of phase diagrams are: melting point of A is 800 K, melting point of B is 1200 K, entropy of fusion of A is 10 J/mol K, entropy of fusion of B is 10 J/mol K, excess Gibbs energy of solid solution $\Delta^E G^s = \omega^s x_A x_B$, excess Gibbs energy of liquid $\Delta^E G^l = \omega^l x_A x_B$. For the purpose of explaining the flat liquidus only the first row of phase diagrams in Figure 18 are discussed below.

In Figure 18(c), the A-B liquid is ideal, but the solid solution is a regular solution with positive excess Gibbs energy. This positive excess Gibbs energy gives the solid-solid miscibility gap. When the excess Gibbs energy of the liquid becomes more and more negative from $\omega^l = -10 \rightarrow -20$ the liquid becomes more stable and the eutectic lines moves down wards. This feature is shown through Figure 18(b) \rightarrow Figure 18(a).

When the Gibbs energy of the liquid becomes more and more positive from $\omega^l = +10 \rightarrow +20$ the liquid becomes less stable and gives rise to a liquid-liquid miscibility gap. This feature is shown through Figure 18(d) \rightarrow Figure 18(e). When the positive deviation of the $\Delta^E G^l$ is not large enough to produce a liquid-liquid miscibility gap, it flattens the liquidus as shown in Figure 18(d). This flattening indicates a meta-stable equilibrium of the liquid phase at lower temperatures, which is shown in broken lines in Figure 18(d). To observe this meta-stable equilibrium one has to suppress the solid phases by sufficiently rapid cooling.

Now let us see an example where the thermodynamic assessment wrongly calculates the liquidus with undulation. For example, in Figure 19 the undulated phase boundaries are observed on the Se rich and on the As rich liquid phase boundaries. These liquidus segments are considered as artifact because of two reasons:

- (i) These calculated liquidus segments do not conform to the locations of experimental points.
- (ii) The assessment used too many (as many as eight) coefficients to model the Se-As liquid.

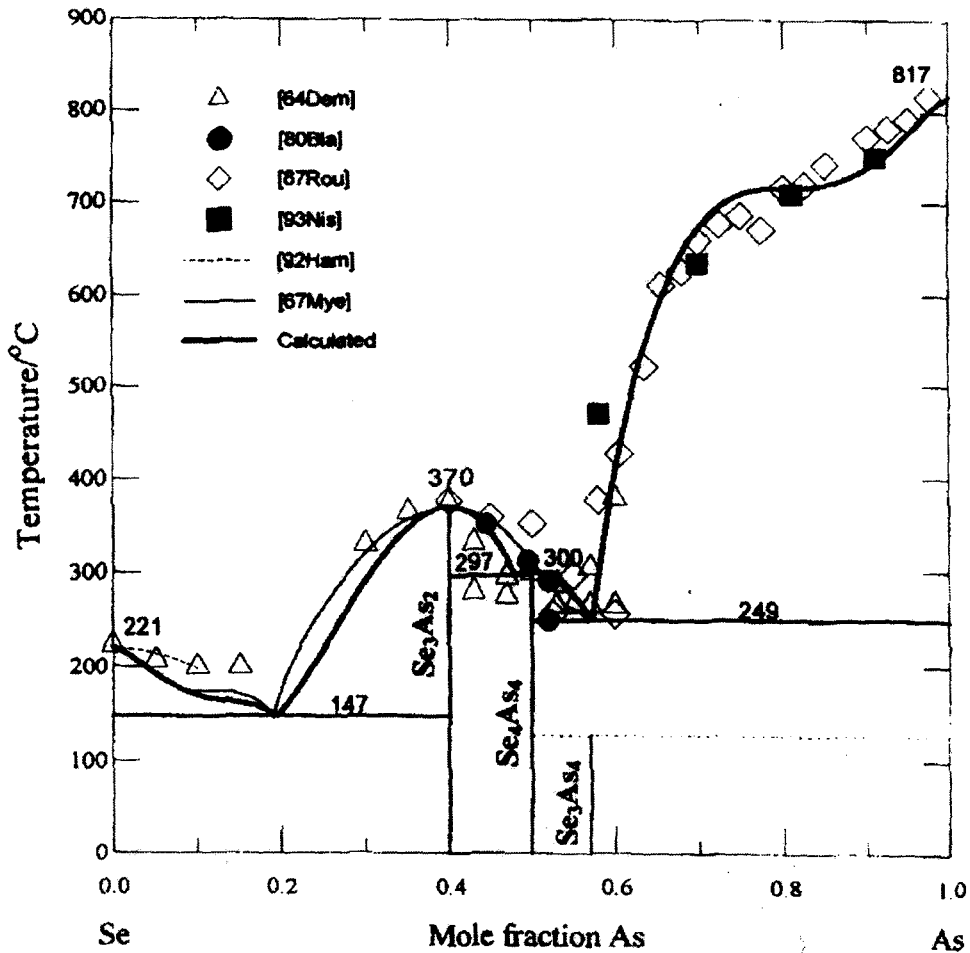


Figure 19: Calculated Se-As phase diagram by Degterov *et al.* [91]

The above-described undulated phase boundaries are generated because in thermodynamic optimization the model parameters are evaluated in such a way that the model calculates thermodynamic values closer to the experimental measurements. Moreover when finding close fitting to discrete experimental data sometimes the characteristic shapes of the phase boundaries such as convexity and concavity would not be achieved. Thermodynamic description of a system should be able to calculate not only

accurate phase diagrams but it also should be able to generate correct topological features of the phase diagram.

We can find many examples for the artifact – undulate phase boundaries in the literature. Some selected examples are given below in Figure 20 - Figure 22. In these figures the undulated phase boundaries are identified by ovals.

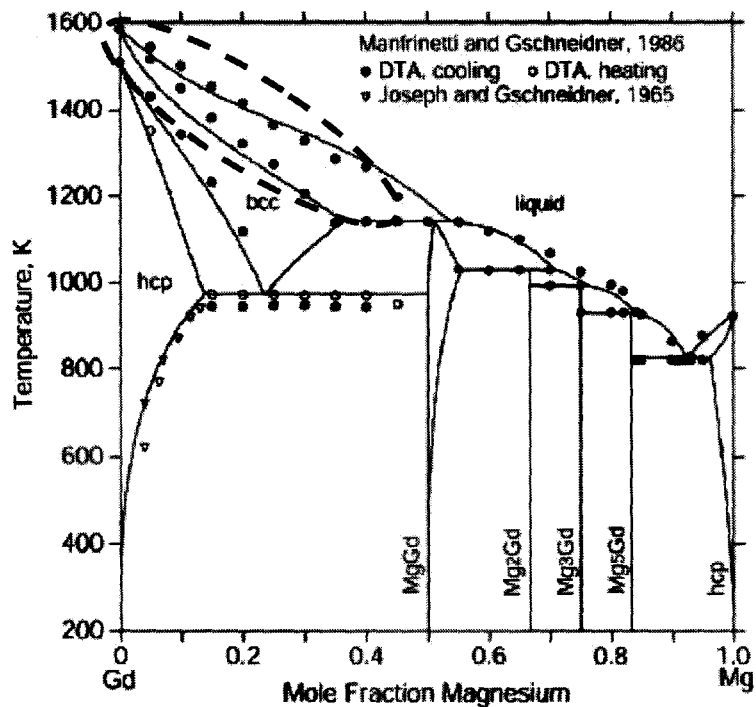


Figure 20: Gd-Mg phase diagram calculated by [92]

Some observations on the selected region in the Figure 20 are as follows:

- The calculated phase boundaries do not show the trend of the experimental points
- Possibly an overfitted phase diagram. The liquid and the bcc phases were modeled using five and six Redlich-Kister coefficients respectively.

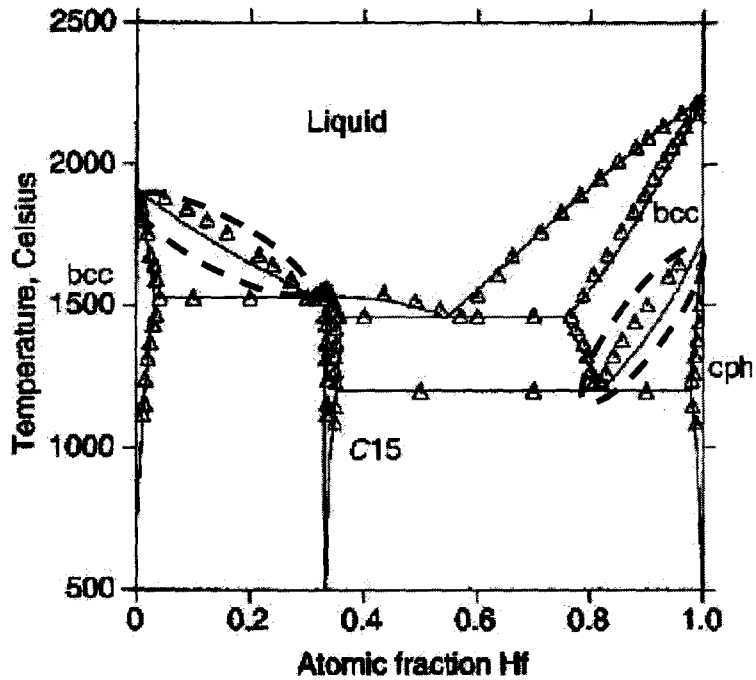


Figure 21: Calculated phase diagram of the V-Hf binary system by [93]

Some comments on the selected region in the Figure 21 are as follows:

- The calculated phase boundaries do not show the trend of the experimental points
- Possibly an overfitted diagram. A huge number of Redlich-Kister coefficients were used to model both the liquid and the bcc phases
- Different models were used to describe a phase in different regions of the phase diagram

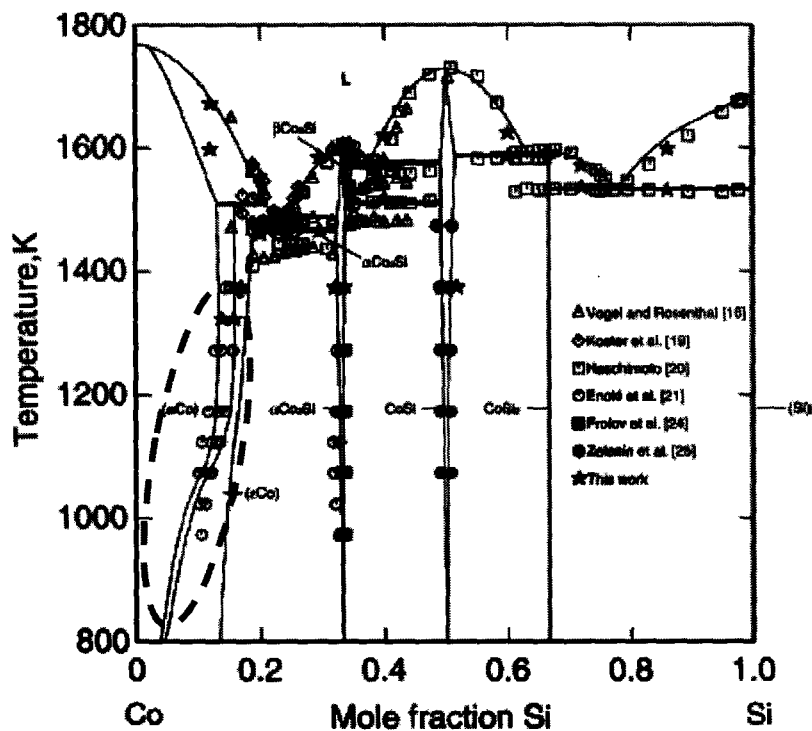


Figure 22: Co-Si phase diagram calculated by [94]

Comments on the selected region in the Figure 22: The calculated phase boundaries do not show the trend of the experimental points.

3.2.1.(c) Low-temperature phase becomes stable again at high-temperature

The third type of erroneous features, which is frequently overlooked during thermodynamic optimization, is the stabilization of low-temperature phase(s) again at high temperatures. Chen *et al.* [75] listed the following assessments for such unrealistic thermodynamic predictions at high temperatures. They are Sn-Ti [79], Nb-C [95], Mo-C [96], Ni-Ti [97], Fe-C [98], Ni-C [99], Al-Co [100], Cr-Ta [101] and, Co-Si [102]. Figure 23 shows the stabilization of the low-temperature phase, Ni_3Ti above the liquidus. The

Ni-Ti phase diagram in Figure 23 calculated using the parameters of [97] is reported in [75].

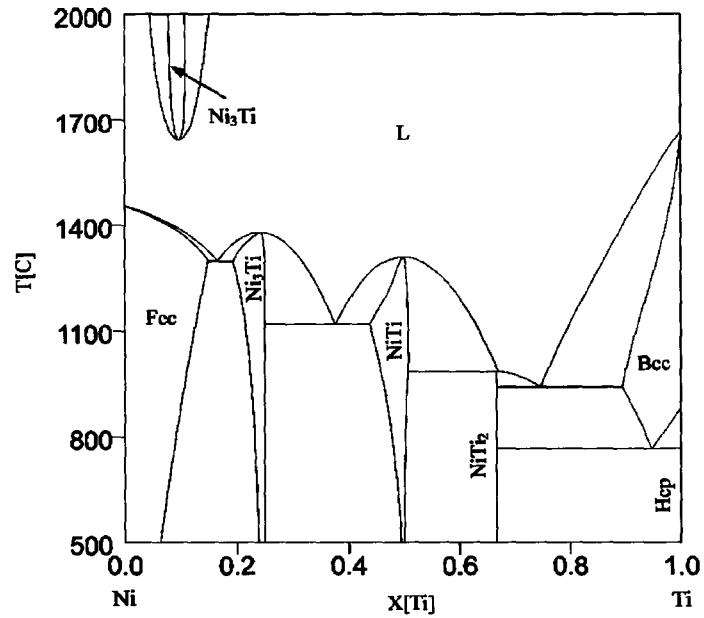


Figure 23: Calculated Ni-Ti phase diagram using the parameters of [97] by Chen *et al.* [75]

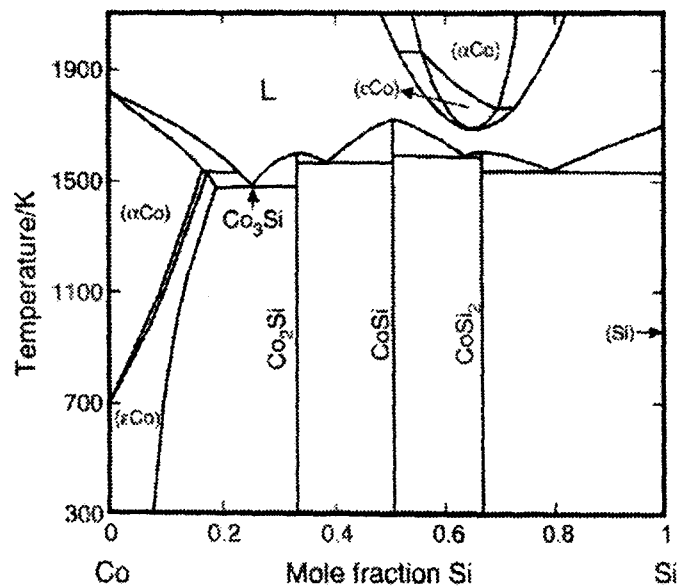


Figure 24: Calculated Co-Si phase diagram using the parameters of [102] by Chen *et al.* [75]

Figure 24 is the calculated Co-Si phase diagram by Chen *et al.* [75] using description of [102], which shows the unrealistic stabilization of the solid phases αCo and εCo above liquidus.

It is reported in [74] that the solid phase may become stable again above the liquidus when the τ -value of the solid solution is significantly higher than that of the liquid solution. Where τ is the temperature at which the interaction parameter L_i in (3.2) would change its sign when extrapolated from $T = 0\text{K}$.

3.2.2 Suspicious temperature and composition dependencies of properties

Figure 25 and Figure 26 demonstrates examples of suspicious temperature and composition dependencies of properties.

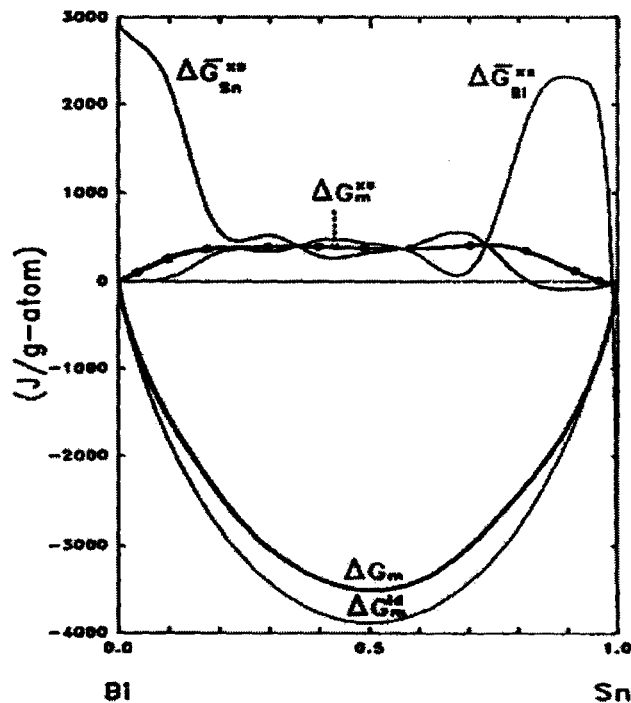


Figure 25: Partial and integral molar Gibbs free energies of liquid Bi-Sn solution as a function of composition at 400°C calculated by Cho and Ochoa [103]

In Figure 25, the thermodynamic description of the liquid Bi-Sn solution by Cho and Ochoa [103] predicts highly wavy partial molar Gibbs energies. Probably this wavy feature resulted from overfittings to experimental data. For example, in a binary system A-B, let us assume that μ_B has multiple extrema within the whole composition range, $[0,1]$. From this assumption we can say that, the function, $\partial(\mu_B)/\partial x = 0$, has multiple roots within $[0,1]$. As we know,

$$\mu_B = G + (1-x) \frac{\partial G}{\partial x} \quad (3.14)$$

We can write,

$$\frac{\partial(\mu_B)}{\partial x} = (1-x) \frac{\partial^2 G}{\partial x^2} = 0 \quad (3.15)$$

where (3.15) has multiple roots. Since $(1-x)$ is always positive, we can write,

$$\frac{\partial^2 G}{\partial x^2} = 0 \quad (3.16)$$

where (3.16) has multiple roots. Now if we expand (3.16) for ideal and excess Gibbs energy terms, we get

$$\frac{\partial^2 (G^{\text{id}})}{\partial x^2} + \frac{\partial^2 (G^{\text{ex}})}{\partial x^2} = 0 \quad (3.17)$$

As we know that $G^{\text{id}} = RT[x \ln x + (1-x) \ln(1-x)]$, from (3.17) we get,

$$RT + x(1-x) \frac{\partial^2 (G^{\text{ex}})}{\partial x^2} = 0 \quad (3.18)$$

where (3.18) has multiple roots. From (3.18) we can deduce that for an n number of extrema to appear in the partial chemical potential, the excess Gibbs energy should be modeled with at least $(n-2)$ coefficients. In the example illustrated in Figure 25, the partial excess Gibbs energies have at least five extrema on each curve. It means that the excess Gibbs energy of the liquid phase should be expressed with at least three parameters. Hence, there is a possibility for over fitted excess properties.

Another example of suspicious calculation of thermodynamic properties is demonstrated in Figure 26 where, Fe content of the liquid phase in the liq/fcc/bcc three-phase equilibrium in the Fe-Cr-Ni system is plotted against temperature.

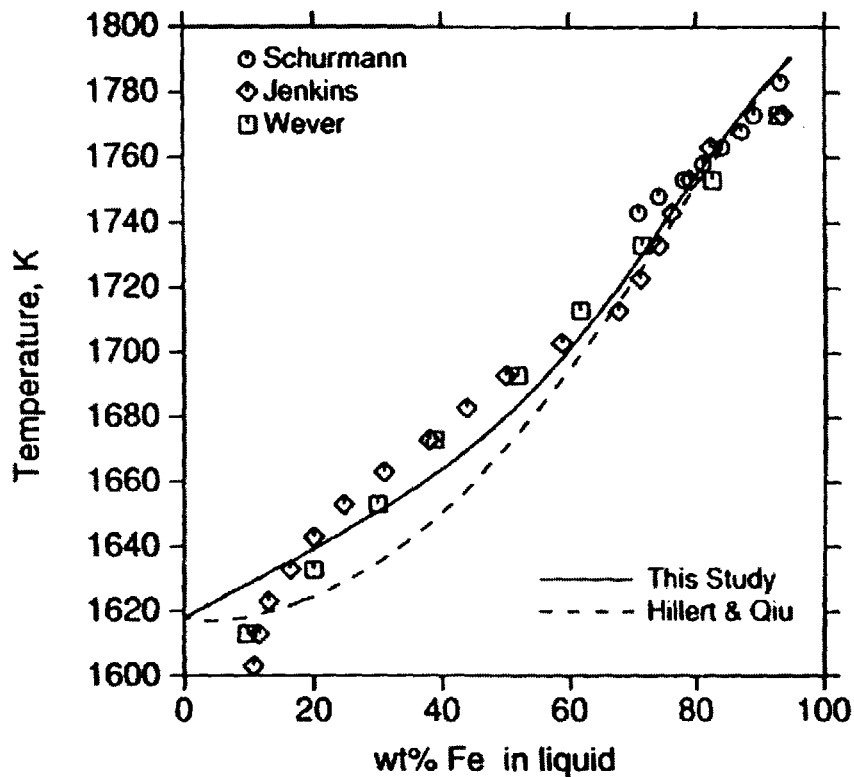


Figure 26: The calculated Fe content of the liquid phase in the liq/fcc/bcc three-phase equilibrium in the Fe-Cr-Ni system by Lee [104]

It can be seen from Figure 26 that the calculation line for the Fe content by [104] does not agree with the trend of the many experimental data points by different researchers shown in the figure. Hence, it can be concluded that the above shown calculation of [104] is suspicious and should be considered as an artifact.

3.3 How to eliminate artifacts?

There are three possible ways to eliminate the artifacts known to the author. Post-optimization phantoms can be avoided:

- (i) By using physically feasible models
- (ii) By Kaptay's method
- (iii) By enforcing the correctness of formalisms and models by using special type of constraints – topological constraints.

3.3.1 Eliminating artifacts by using physically feasible models

By far the best way to eliminate thermodynamic artifacts is by using physically feasible models that describe physical or chemical feature of phases. Some of the widely used models that describe the physical feature of phases are associate solution model [36], quasi-chemical model [105], and cluster variation method-based models [106].

For example the associate solution model would be a good choice to describe a solution phase, which exhibits short range ordering (SRO). A solution with SRO will result a typical “V” shaped enthalpy of mixing Vs composition diagram. For instance let us consider an imaginary A-B liquid solution with a pronounced SRO at the equimolar composition. In associate solution modeling, this physical feature of the liquid is reflected

by introducing the AB associate as a constituent of the liquid. In this case, the Gibbs energy of the liquid is given by:

$$\begin{aligned}
 G_m^L = & y_A G_A^0 + y_B G_B^0 + y_{AB} G_{AB}^0 \\
 & + RT \left[y_A \ln(y_A) + y_B \ln(y_B) + y_{AB} \ln(y_{AB}) \right] \\
 & + y_A y_B L_{A,B} + y_{AB} y_A L_{AB,A} + y_{AB} y_B L_{AB,B}
 \end{aligned} \quad (3.19)$$

where y_A , y_B and y_{AB} are the site fractions of the constituents A, B, and AB respectively.

The major disadvantage of using the associate solution model in thermodynamic optimizations is that when the interactions between the constituents are large, the random entropy of mixing, $S_m^{id} = -R \left[y_A \ln(y_A) + y_B \ln(y_B) + y_{AB} \ln(y_{AB}) \right]$ used in (3.19) will overestimate the Gibbs energy of the phase. Even though this overestimation of the Gibbs energy could be adjusted through the excess contribution

$G_m^{ex} = y_A y_B L_{A,B} + y_{AB} y_A L_{AB,A} + y_{AB} y_B L_{AB,B}$, it is reported that this excess contribution might yield a bad extrapolation to higher order systems [31]. Hence, associate solution model cannot be applied to all thermodynamic systems in eliminating thermodynamic artifacts.

The Gibbs energy description by quasi-chemical model gives a better description for the ideal entropy of mixing than does the associate solution model. To describe an imaginary A-B liquid solution with a strong SRO at the 1:1 composition, the quasi-chemical model assumes that bonding between A and B atoms gives molecules of AA, BB, AB, and BA. These molecules are assumed to be randomly distributed in the

solution. The creation of bonds is given by the chemical reaction for the molecules AA, BB, AB, and BA:



For a solution with z number of bonds per atom, the Gibbs energy of the solution by the quasi-chemical model is given by,

$$\begin{aligned} G_m^L &= y_{AA} G_A^0 + y_{BB} G_B^0 + y_{AB} G_{AB}^0 + y_{BA} G_{BA}^0 \\ &+ \frac{z}{2} RT \left[y_{AA} \ln \left(\frac{y_{AA}}{x_A^2} \right) + y_{BB} \ln \left(\frac{y_{BB}}{x_B^2} \right) + y_{AB} \ln \left(\frac{y_{AB}}{x_A x_B} \right) + y_{BA} \ln \left(\frac{y_{BA}}{x_A x_B} \right) \right] \\ &+ RT [x_A \ln(x_A) + x_B \ln(x_B)] \\ &+ G_m^{ex} \end{aligned} \quad (3.21)$$

where y_{AA} , y_{BB} , y_{AB} , and y_{BA} are the site fractions of the constituents AA, BB, AB, and BA respectively; x_A , and x_B are the mole fractions of A and B. Moreover one can relate the site and mole fractions using the mass balance constraints. That is,

$$x_A = y_{AA} + 0.5(y_{AB} + y_{BA}) \quad (3.22)$$

$$x_B = y_{BB} + 0.5(y_{AB} + y_{BA}) \quad (3.23)$$

Even though the quasi-chemical model gives better Gibbs energy estimation than does the associate solution model it is again reported in [31] that the ideal entropy of mixing in (3.21),

$$\begin{aligned} S_m^{id} &= \frac{z}{2} RT \left[y_{AA} \ln \left(\frac{y_{AA}}{x_A^2} \right) + y_{BB} \ln \left(\frac{y_{BB}}{x_B^2} \right) + y_{AB} \ln \left(\frac{y_{AB}}{x_A x_B} \right) + y_{BA} \ln \left(\frac{y_{BA}}{x_A x_B} \right) \right] \\ &+ RT [x_A \ln(x_A) + x_B \ln(x_B)] \end{aligned} \quad \text{is only valid}$$

for small degree of SRO. Moreover it is shown in [31] that when the SRO is strong and

for $z > 2$ then S_m^{id} may become negative. Hence, quasi-chemical model too cannot be applied to all thermodynamic systems in eliminating thermodynamic artifacts.

In the case of cluster variation method (CVM) the quasi-chemical entropy is improved by considering clusters with three, four, and more atoms. These clusters are treated as independent constituents of the solutions. However, in deriving the ideal entropy of mixing of these clusters, they are assumed to share their corners, edges, surfaces, etc with each other. This consideration is the basic difference between the quasi-chemical and the CVM. For a short range ordered liquid solution with the clusters A, $A_{0.75}B_{0.25}$, $A_{0.5}B_{0.5}$, $A_{0.25}B_{0.75}$, and B the Gibbs energy is given by:

$$\begin{aligned}
 G_m^L = & y_A G_A^0 + y_{A_{0.75}B_{0.25}} G_{A_{0.75}B_{0.25}}^0 + y_{A_{0.5}B_{0.5}} G_{A_{0.5}B_{0.5}}^0 + y_{A_{0.25}B_{0.75}} G_{A_{0.25}B_{0.75}}^0 + y_B G_B^0 \\
 & + 2RT \left[y_A \ln(y_A) + y_{A_{0.75}B_{0.25}} \ln(y_{A_{0.75}B_{0.25}}) + y_{A_{0.5}B_{0.5}} \ln(y_{A_{0.5}B_{0.5}}) \right. \\
 & \left. + y_{A_{0.25}B_{0.75}} \ln(y_{A_{0.25}B_{0.75}}) + y_B \ln(y_B) \right] \\
 & + 2RT \left[(y_{A_{0.75}B_{0.25}} + y_{A_{0.25}B_{0.75}}) \ln(4) + y_{A_{0.5}B_{0.5}} \ln(6) \right] \\
 & - 6RT \left[p_{AA} \ln(p_{AA}) + p_{AB} \ln(p_{AB}) + p_{BA} \ln(p_{BA}) + p_{BB} \ln(p_{BB}) \right] \\
 & + 5RT \left[x_A \ln(x_A) + x_B \ln(x_B) \right] \\
 & + G_m^{\text{ex}}
 \end{aligned} \tag{3.24}$$

where the clusters are assumed to share the edges and corners with each other;

$y_A, y_{A_{0.75}B_{0.25}}, y_{A_{0.5}B_{0.5}}, y_{A_{0.25}B_{0.75}}$, and y_B are cluster fractions; p_{AA}, p_{AB}, p_{BA} , and p_{BB} are pair probabilities; x_A , and x_B are the mole fractions of A and B respectively.

The Gibbs energy description in (3.24) is superior to the description of associate solution model and quasi-chemical model. However when it comes to multi-component system the number of clusters increases exponentially with the number of components

and thermodynamic calculations become extremely difficult. Hence, the applicability of CVM in suppressing artifacts is not always possible.

3.3.2 Kaptay's method of artifact elimination

As explained in section 3.2.1, artificial inverted miscibility gaps are observed when the interaction parameter L_i in the excess Gibbs energy term is linear dependent of temperature as given in (3.2). To suppress this artifact Kaptay [74] developed a formalism by considering the following boundary conditions:

Condition 1: When $T \rightarrow 0$, ΔG^E reaches a finite value ΔH_0 . Hence, the condition to be satisfied is,

$$\lim_{T \rightarrow 0} L_i = h_{0i} \quad (3.25)$$

Condition 2: When $T \rightarrow 0$, the slope of the ΔG^E with respect to T reaches $-\Delta S_0^E$.

Hence, the condition to be satisfied is,

$$\lim_{T \rightarrow 0} \frac{dL_i}{dT} = -s_{0i} \quad (3.26)$$

He derives the third boundary condition by considering the interaction of atoms at very high temperatures. When temperature becomes infinitely high, the interaction between the atoms vanishes and the atoms distribution becomes random. That is, when $T \rightarrow \infty$ the solution becomes ideal. In other words, when temperature is very high, the excess Gibbs energy should reach zero.

Condition 3: When $T \rightarrow \infty$, the ΔG^E reaches zero. Hence, the condition to be satisfied is,

$$\lim_{T \rightarrow \infty} L_i = 0 \quad (3.27)$$

In calculating a stable phase diagram, the selected excess Gibbs energy model should satisfy the above three conditions in (3.25)-(3.27). To analyze the satisfying boundary conditions during thermodynamic optimization, Kaptay [74] considers the following three different possibilities for the excess heat capacities.

Case 1: The most complex form,

$$c_i(T) = A_i + B_i T + C_i T^2 + D_i T^{-2} \quad (3.28)$$

$$L_i = a_i + b_i T + c_i T \ln T + d_i T^2 + e_i T^3 + f_i T^{-1} \quad (3.29)$$

Case 2: The rarely used form of excess heat capacity in thermodynamic optimizations,

$$c_i(T) = A_i \quad (3.30)$$

$$L_i = a_i + b_i T + c_i T \ln T \quad (3.31)$$

Case 3: The frequently used form,

$$c_i(T) = 0 \quad (3.32)$$

$$L_i = h_{0i} - s_{0i} T \quad (3.33)$$

where (3.29), (3.31), and (3.33) are the interaction parameter terms derived for the case 1, 2, and 3 respectively.

When the interaction parameter in (3.29) is used in the excess Gibbs energy none of the three conditions are satisfied. When the interaction parameters in (3.31) or (3.33), the first two boundary conditions in (3.25) and (3.26) are satisfied but they fail to satisfy the third condition (3.27). Due to the above contradictory results in the boundary

conditions, the widely used linear interaction parameters in (3.33) tend to generate artifacts at high temperatures.

To calculate a stable phase diagram without generating any artifacts Kaptay proposed the following formalism for L_i :

$$L_i = h_{0i} \exp\left(-T \frac{s_{0i}}{h_{0i}}\right) \quad (3.34)$$

According to Lupis and Elliott [107], $\frac{h_{0i}}{s_{0i}} = \tau_{0i}$ which is the temperature at which the system becomes ideal when the experimental results at temperature T are extrapolated linearly. Moreover Lupis and Elliott [107] found that for the majority of the metallic solutions the heat of mixing and excess entropy of mixing have the same sign. Hence,

$$\tau_{0i} = \frac{h_{0i}}{s_{0i}} > 0 \quad (3.35)$$

The expression for L_i in (3.34) satisfies all three boundary conditions given in (3.25)-(3.27). In addition to the three boundary conditions, the condition in (3.35) is to be satisfied during the evaluation of the parameters h_{0i} and s_{0i} .

Arroyave and Liu [108] tried the Kapatay's formalism to model the liquid phase during the thermodynamic optimization of the Zn-Zr system. It was reported in [108] that the agreement between the experimental data and the calculations by Kaptay's formalism were not satisfactory and a more complicated temperature dependencies were needed to get a passable agreement with experimental data and the calculations.

More adverse effect was observed when Schmid-Fetzer *et al.* [109] re-assessed the Mg-Si system using the Kaptay's formalism to eliminate the inverted miscibility gap in the system from its previous assessment. In this re-assessment, the Kaptay's formalism successfully eliminated the inverted miscibility gap. However, Schmid-Fetzer *et al.* [109] detected the re-stabilization of the liquid phase at low temperature. Schmid-Fetzer *et al.* [109] pointed out that when the parameter h_{0i} becomes negative, the exponential function exaggerate the Gibbs energy at very low temperature, resulting in the re-stabilization of the liquid phase at low temperature.

The Figure 27 given below shows the re-stabilization of the liquid phase during the reassessment of the Mg-Sb system by Schmid-Fetzer *et al.* [109] using the Kaptay's formalism.

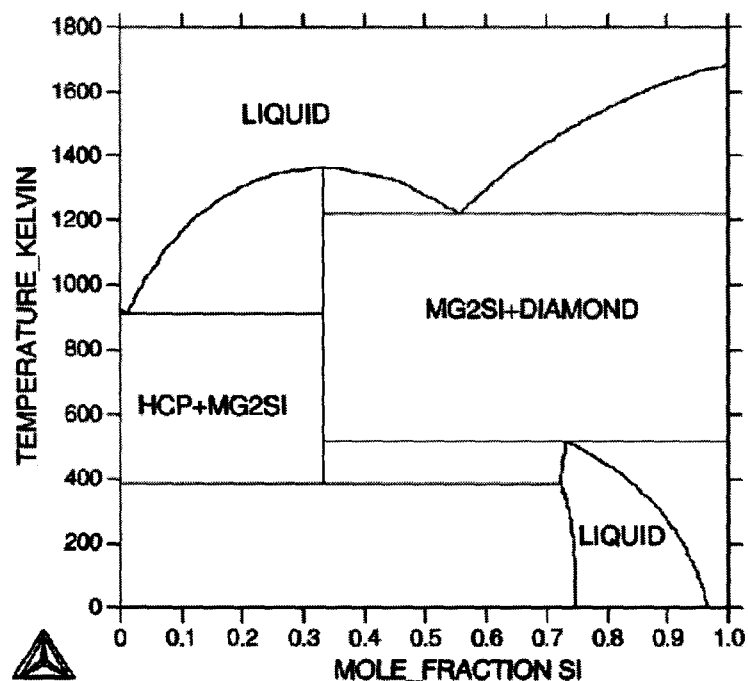


Figure 27: The calculated Mg-Si phase diagram by Schmid-Fetzer *et al.* [109] using the Kaptay's formalism in (3.34)

From the above example we can conclude that the Kaptay's method is not a universal solution in eliminating thermodynamic artifacts.

3.4 Conclusions

The above-discussed methods to struggle against thermodynamic artifacts give problem-specific solutions. Hence this thesis proposes a new approach to find a general solution to eliminate thermodynamic artifacts by employing topological constraints in thermodynamic optimization. The essence of employing topological constraints in thermodynamic optimization will be revealed in chapter 5.

CHAPTER 4

Shape-preserving approximation

4.1 Introduction

The objective of this chapter is to explore the existing shape preserving approximation techniques in order to make sure that the algorithm proposed in this thesis has no parallels or overlaps to any already existing approaches.

The importance of preserving the correct shape of a function describing experimental data was realized in different research areas such as cartography, engineering design, meteorology, statistics, computer graphics and animation. For example, consider the derivation of nonparametric probability density function f from random sample of responses under the assumptions that the function is unimodal. However, since the responses are affected by random noise, the function estimated is not guaranteed to have the single maximum if the traditional likelihood method is employed. In order to eliminate possible extrema, it was suggested to use a penalized likelihood method [110], *i.e.*

$$\text{maximize } \prod_i f(x_i) \exp\left\{-p \int [f''(t)]^2 dt\right\}, p > 0 \quad (4.1)$$

Physically unacceptable oscillations in f are eliminated by increasing the smoothing parameter p . In other words, the inclusion of the parameter p in (4.1) helps to eliminate wiggles in functions interpolating experimental data.

A topologically constrained interpolation (also known as isogeometric interpolation) problem is solved through procedure known as polynomial fitting. The basic idea behind this procedure is to find a polynomial function that goes through all the given (experimental) points. The main attraction for this class of functions in interpolations is due to their easy computations in addition, multiplication, differentiation and integration. It is always possible to find a polynomial function that fits through all the given data points. However, when the number of points increases the order of the polynomial function as well as the wiggles and oscillations of the fitted curve also found to increase. This oscillation problem in polynomial interpolation is overcome by using sufficient number of low order polynomial segments (also known as splines) between pair of interpolating points and joining them in a smooth way [111, 112].

4.2 Existing methods of isogeometric curve and surface fitting

One of the existing procedures to find approximations while preserving topological features is found in Akima [113, 114] where the resulting curve is found to be in agreement with the global shape implied by data points. However the fitted curve does not have a continuous second derivative. Another approach reported for similar objective in [115, 116] guarantees that if experimental data had convex and concave regions, then convexity and concavity of the interpolating spline will be consistent with these intervals. Again, the resulting spline did not have a continuous second derivative.

A traditional way of smoothing an approximant with false extrema and inflection points is to add the energy functional to the target function as follows:

$$(1-p) \sum_{i=1}^n \omega_i [y_i - f(x_i, \bar{C})]^2 + p \int_{x_1}^{x_n} [f''(t, \bar{C})]^2 dt \rightarrow \min(\bar{C}), \quad 0 \leq p < 1 \quad (4.2)$$

When the smoothing parameter p is zero, the problem is the usual polynomial fitting problem since the second term in the left hand side of (4.2) becomes zero. This results in an excellent fitting, however, the unwanted wavy shapes or wiggles are prone to present in this case. On the other hand, when p tends to one, the leftmost term in (4.2) vanishes and the resulting minimization will yield a straight line that is obviously not useful. It is sensible to find a balance between these extreme cases and to find a value of p that gives enough weight for accuracy of fitting while maintaining the shape of the function approximate enough to the topological shape. Sometimes such an approach works [117], but in general, it does not guarantee that a topologically correct solution can be obtained. Moreover, the only one class of functions whose utilization in (4.2) is computationally feasible is splines. The next sub-section gives a brief introduction to spline curves.

4.3 Isogeometric interpolations by splines

Splines are advanced types of isogeometric-interpolated curves that have many applications in computer graphics and animation. A common idea behind the techniques is to partition the data range into smaller segments and to find a local fitting curve that seamlessly joints with the adjacent local curves. The analysis of spline curves is often preceded by a similar curve called Bezier curves from which the idea of splines has evolved. Bezier curves were first used by a French engineer named Pierre Bézier in automobile body design.

In isogeometric Bezier curve and spline curve interpolations, the data range is portioned into smaller segments and a local fitting is found. When each segment has three data points (notice that each segments having two points is a rather obvious case in which the best fit through polynomial, Bezier, or spline curves is the straight line between these two points) they are called quadratic Bezier curves and quadratic spline curves respectively. When each segment has four data points they are called cubic Bezier curves and cubic spline curves respectively. Cubic Bezier/spline curves have wider applications in shape preserving approximations.

The main advantage of using Bezier curve interpolation over polynomial interpolation is that the adjacent interpolated curves have a smooth joint. However, this type of interpolations suffer from a feature that is known as lack of local control, *i.e.*, even though they avoid wiggles compared to polynomial curves, Bezier curves are found far apart to some of the data points. To avoid this problem spline curve interpolations use weighted control through data points. In calculating a certain value of the curve, nearest data points are given higher weights. Usually the weight distribution is arranged to reflect a Gaussian shape. The spline curves assure the existence of first derivative and second derivative for some cases. However, it is impossible to impose any conditions to be satisfied on the second derivatives.

The most popular choice to get smoother approximations in isogeometric interpolations is the cubic splines. The reason for smoother approximation by cubic splines is that these functions possess at least a continuous first derivative and in some

cases, even a continuous second derivative [111]. APPENDIX I gives more details on Bezier curves and spline curves.

4.4 Spline approximation in thermodynamic optimizations

The publication by Voronin, and Degtyarev [118] shows possible application of spline approximation in thermodynamic calculations. In [118], the authors performed different thermodynamic calculations on binary systems and showed that the spline approximation is useful in thermodynamic calculations. It can be seen from Figure 28 and Figure 29 that the spline approximation gives higher accuracy than that of the conventional linear least squares approximation. Moreover Voronin, and Degtyarev showed the possible application of spline approximation in phase diagram calculations by calculating liquidus lines in the binary system In-Sb. However, spline approximation is hardly applicable in multi-component thermodynamic calculations. By far, [118] is the only published work, which uses the spline approximation in thermodynamic calculations.

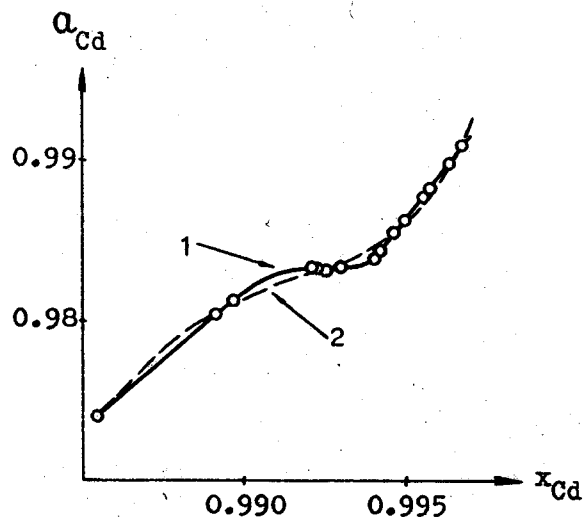


Figure 28: Activity calculations of Cd in Cd-Au system at 777K by [118] shows the comparison of spline approximation (line 1) with the conventional linear least squares approximation (line 2)

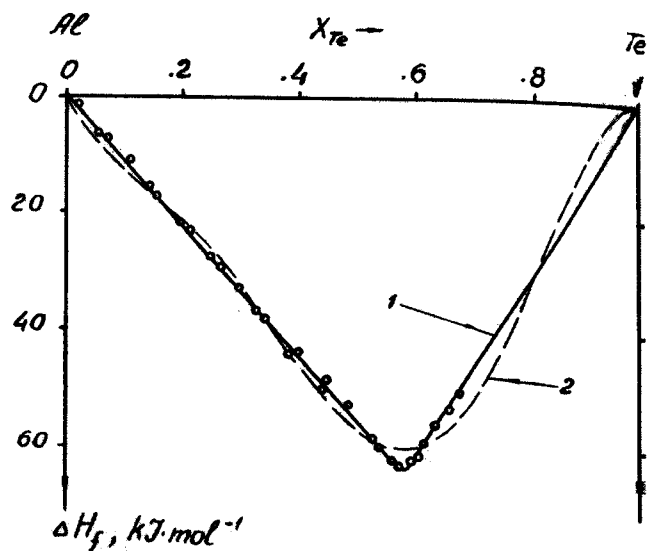


Figure 29: Calculation of integral molar enthalpy of formation of Al-Te alloys at 1188K by [118] shows the comparison of spline approximation (line 1) with the conventional linear least squares approximation (line 2)

4.5 Conclusions

Shape preserving approximation techniques have applications in many other research areas other than thermodynamic optimization. Different shape preserving approximation techniques developed to fulfill some specific objectives are available in the literature. However, none of the available techniques are found to satisfy the requirements arisen in thermodynamic optimization.

CHAPTER 5

Topological constraint in eliminating inverted miscibility gaps during re-assessment of the Mg-Sb system

5.1 Introduction

In this chapter a novel method to eliminate artificial inverted miscibility gap during thermodynamic optimization is proposed. Unlike traditional CALPHAD technique, which is an unconstrained non-linear least squares optimization technique, the proposed method in this chapter performs a topologically constrained non-linear least squares optimization.

In order to achieve the correct shape of the phase diagram, topological constraints that govern the appearance of the phase diagram are set to be satisfied on a sufficiently dense mesh of knots during thermodynamic optimization. These knots are not related to the experimental points used in the optimization and are introduced within the region where inverted miscibility gap is observed.

Moreover, it is shown that syntax of the language describing conditions and experiments in the PARROT module of Thermo-Calc is suitable for performing such kind of optimization. A workability of the method proposed is exemplified by carrying out a re-optimization of the Mg-Sb system.

5.2 Problem formulation

In [86], the thermodynamic properties of the Mg-Al-Sb system were assessed using the CALPHAD method. As a part of that assessment, the thermodynamic properties

of the Mg-Sb system were optimized. The optimization was based on experimental data on activities of Mg in the liquid phase [119-121] and conditions of phase equilibria [122, 123]. A passable agreement between the experimental and calculated quantities was obtained. The phase diagram shown in Figure 30 is unquestionably reasonable being a “computed twin” of the Mg-Sb diagrams evaluated by experts [20, 124]. According to [41], lattice stabilities of Mg are defined from 298.15 to 3000 K, while these for Sb are determined within the 298.15-2000 K range. This, in particular, means that the calculated properties of the liquid phase should not be trusted above 2000 K, but nothing dramatic is expected to happen if the upper limit of the temperature axis in Figure 30 is extended from 1600 to 2000 K.

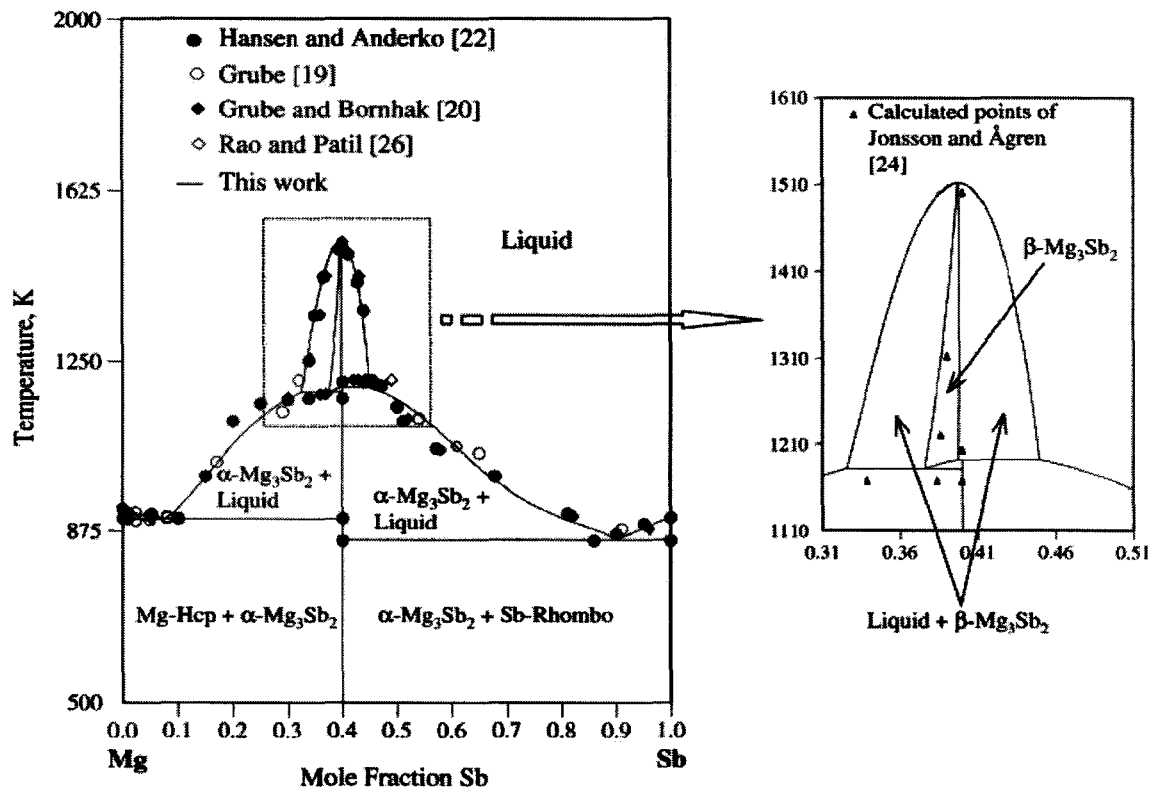


Figure 30: The calculated phase diagram of the Mg-Sb system by Balakumar and Medraj [86]

An inspection of Figure 31, however, reveals an unexpected phenomenon: the liquid phase has two inverted miscibility gaps. It is very unlikely that the actual Mg-Sb melt is prone to separation; it is the description of the Gibbs energy of the melt proposed in [86] that incorrectly predicts such a behavior!

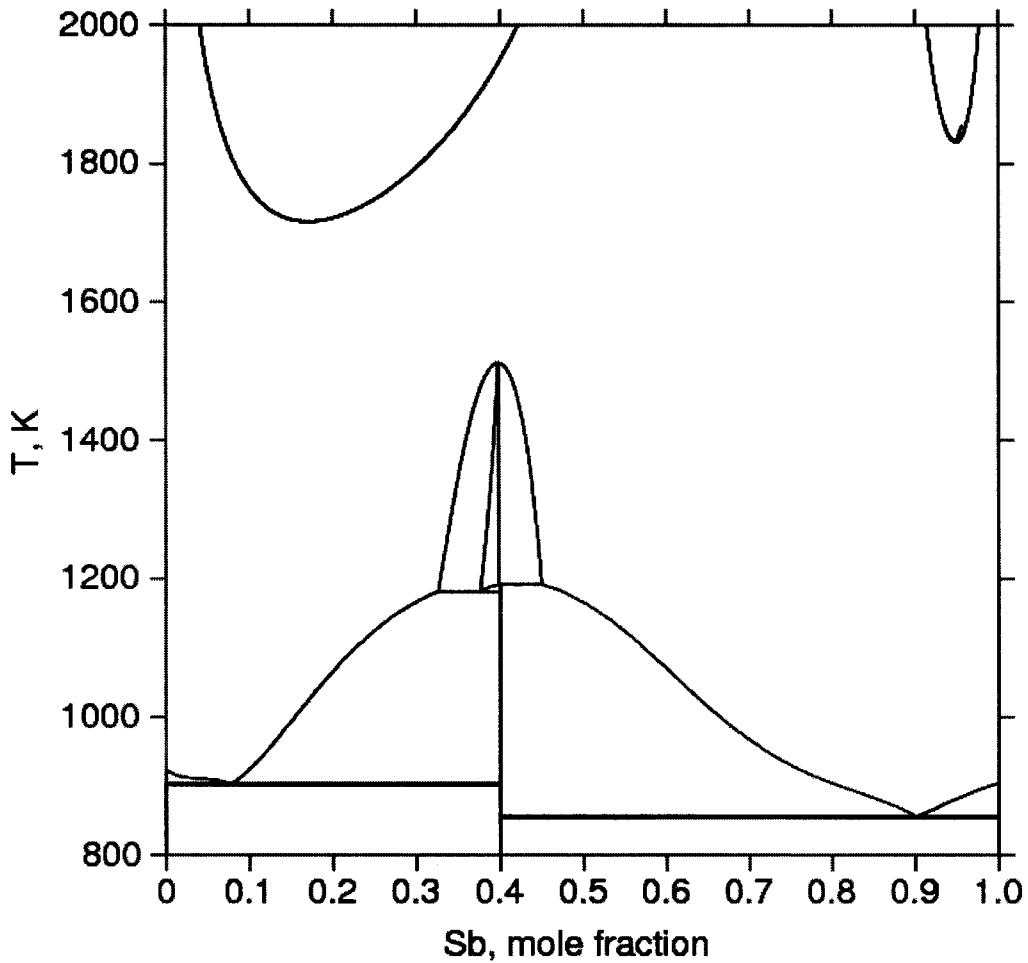


Figure 31: Inverted miscibility gaps resulted from the thermodynamic model for the liquid phase proposed in [86]

The one possible way to analyze the predictions of the Mg-Sb liquid phase model proposed in [86] is by checking the stability of the liquid phase through Darken's stability

function. In Thermo-Calc syntax, $QF\langle\text{phase}\rangle$ refers to the Darkens stability function. For a binary system $QF\langle\text{phase}\rangle$ is defined as:

$$QF\langle\text{phase}\rangle = \frac{x^{\text{phase}}(1-x^{\text{phase}})}{(RT)} \frac{\partial^2 G^{\text{phase}}}{\partial (x^{\text{phase}})^2} \quad (5.1)$$

In (5.1), the term $x^{\text{phase}}(1-x^{\text{phase}})/(RT)$ is always positive. Hence the sign of the term $\partial^2 G^{\text{phase}}/\partial (x^{\text{phase}})^2$ is equal to the sign of the function $QF\langle\text{phase}\rangle$. Moreover $\partial^2 G^{\text{phase}}/\partial (x^{\text{phase}})^2$ can be related to the curvature of G^{phase} in the following manner. By definition,

$$\text{curvature of } G^{\text{phase}} \text{ with respect to the composition } x^{\text{phase}} = \frac{\frac{\partial^2 G^{\text{phase}}}{\partial (x^{\text{phase}})^2}}{\left\{1 + \left[\frac{\partial G^{\text{phase}}}{\partial (x^{\text{phase}})}\right]^2\right\}^{3/2}} \quad (5.2)$$

In (5.2) the denominator is always positive. Hence, the sign of the curvature of G^{phase} is same as the sign of $\partial^2 G^{\text{phase}}/\partial (x^{\text{phase}})^2$.

For a phase to be stable the stability function should possess a positive value. In other words $QF\langle\text{phase}\rangle > 0$ in the stable phase region. Further, one can say that the curvature of G^{phase} with respect to the composition is positive in the stable phase region. Hence, by checking the sign of the function $QF\langle\text{phase}\rangle$ one can detect the topology of the G^{phase} such as regions of convexity ($QF\langle\text{phase}\rangle > 0$) and concavity ($QF\langle\text{phase}\rangle < 0$).

The above-mentioned analysis using the function $QF\langle\text{phase}\rangle$ is carried on the Mg-Sb liquid for the description given in [86]. The values of the function $QF\langle L\rangle$ are calculated for the whole composition range at temperatures 500 K, 1000 K, 1500 K, and 2000 K.

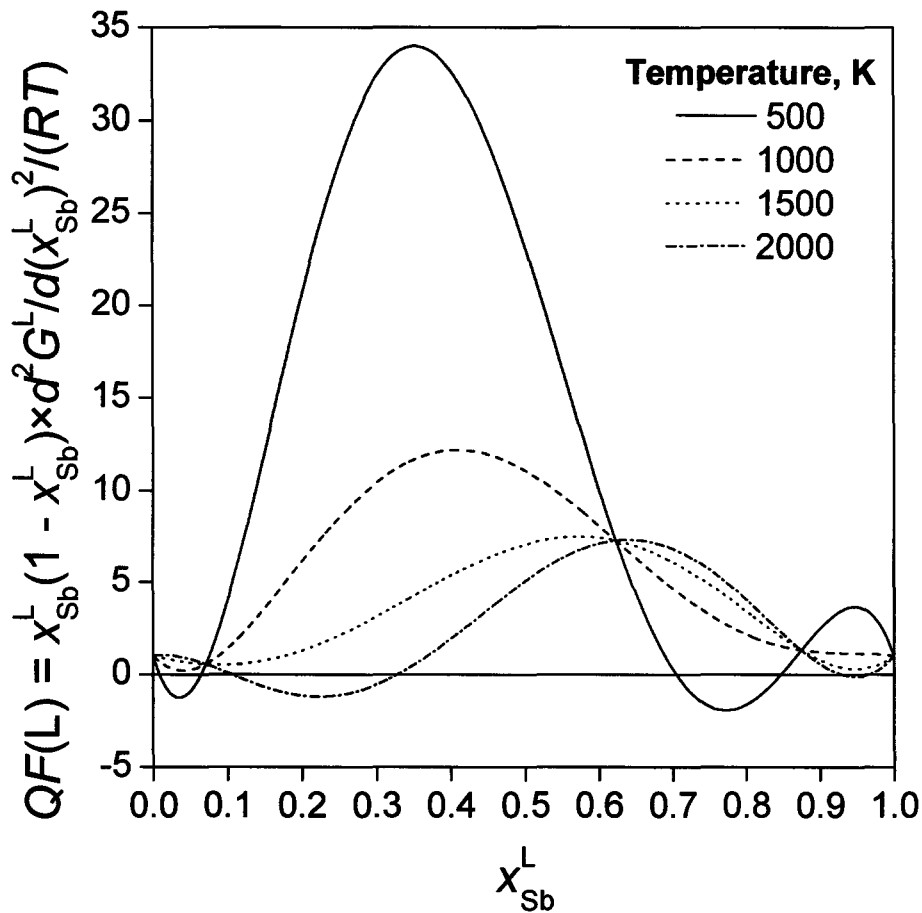


Figure 32: A plot of $QF\langle L\rangle$ Vs mole fraction of Sb at different temperatures for the Mg-Sb liquid description in [86]

By looking at the sign of the function $QF\langle L\rangle$ in Figure 32, the regions of convexity and concavity of the concentration dependencies of the Gibbs energy of the

liquid phase can be detected. The composition ranges at 2000 K for the negative $QF\langle L \rangle$ in Figure 32 correspond to the composition ranges where inverted miscibility gaps are observed at 2000 K in Figure 31.

For grasping the gravity of the problem encountered, let us recall that one of the most acclaimed features of the CALPHAD method is that the Gibbs energies of phases evaluated with its aid can then be used for estimating properties that were not measured experimentally. They can also be employed for calculating the phase boundaries beyond a range of conditions within which the experiments were performed. The latter case includes the computation of metastable continuations of phase boundaries, which are utilized for specifying boundary conditions when certain types of diffusion-controlled transformations is modeled. The example given for the Mg-Sb system suggests that accurately reproducing all experimental data cannot guarantee by itself that the Gibbs energies would automatically be suitable for such kind of extrapolation.

5.3 Possible approaches to the problem

Before going into details about topologically constrained thermodynamic optimization in eliminating the inverted miscibility gap in the Mg-Sb system, let us investigate possible other approaches to eliminate the inverted miscibility gap, particularly for the Mg-Sb system. As explained in section 3.3.1 the best way of action is finding a better, physically feasible model. With respect to the Mg-Sb melt, it can be speculated that the Redlich-Kister formalism used in [86] is not particularly good because magnesium and antimony are chemically different. For melts formed by a typical metal (such as Mg) and an element demonstrating pronounced non-metallic characteristics

(such as Sb) it might be advantageous to use the partially ionic liquid model [37], which reflect a strong affinity between such components. The model $(Mg^{2+})_p (Sb, Sb^{3-}, Va^{2-})_q$ used by Jönsson and Ågren [125,126] did not lead to an inverted miscibility gap in the magnesium-antimony melt at elevated temperatures.

If a better model is difficult to find, then various empirical or heuristic approaches can be tried. An interesting and very elegant semi-empirical method for getting rid of the inverted miscibility gap proposed by Kaptay [74] was explained in section 3.3.2. That method, however, is not capable of handling the situations when a phase becomes stable in a region, within which it should not exist. Besides, a utilization of Kaptay's formalism in practice is hampered by a necessity to re-write source codes upon which Gibbs energy minimizers and procedures for optimization are based.

An example of a heuristic approach can be found in [127], in which the results of optimization of the Bi-Zn system were presented. After it had been realized that the miscibility gap in the liquid phase should be convex, actual experimental points related to $L_1/L_1 + L_2$ and $L_1 + L_2/L_2$ phase boundaries were substituted with specially constructed values, for which convexity was guaranteed. Those artificial values were used in the course of assessment. The trick, which helped to make the miscibility gap flat and convex, had an unexpected favorable side effect: as Figure 33 shows, the description of the liquid phase did not suffer from the existence of an inverted miscibility gap at high-temperatures. This circumstance is quite surprising since the liquid phase was modeled by using the Redlich-Kister formalism with as many as six $A_i + B_i T$ terms, *i.e.* with totally twelve coefficients. Usually, it is sagaciously believed that the expression

$x(1-x)\sum_{i=0}^{\infty}(1-2x)^i(A_i+B_iT)$ with numerous coefficients is very prone to demonstrating post-optimization artifacts, but it seems that the constraint imposed (“the miscibility gap must be convex”) was an efficient remedy against an awkward behavior of the liquid phase at high-temperatures.

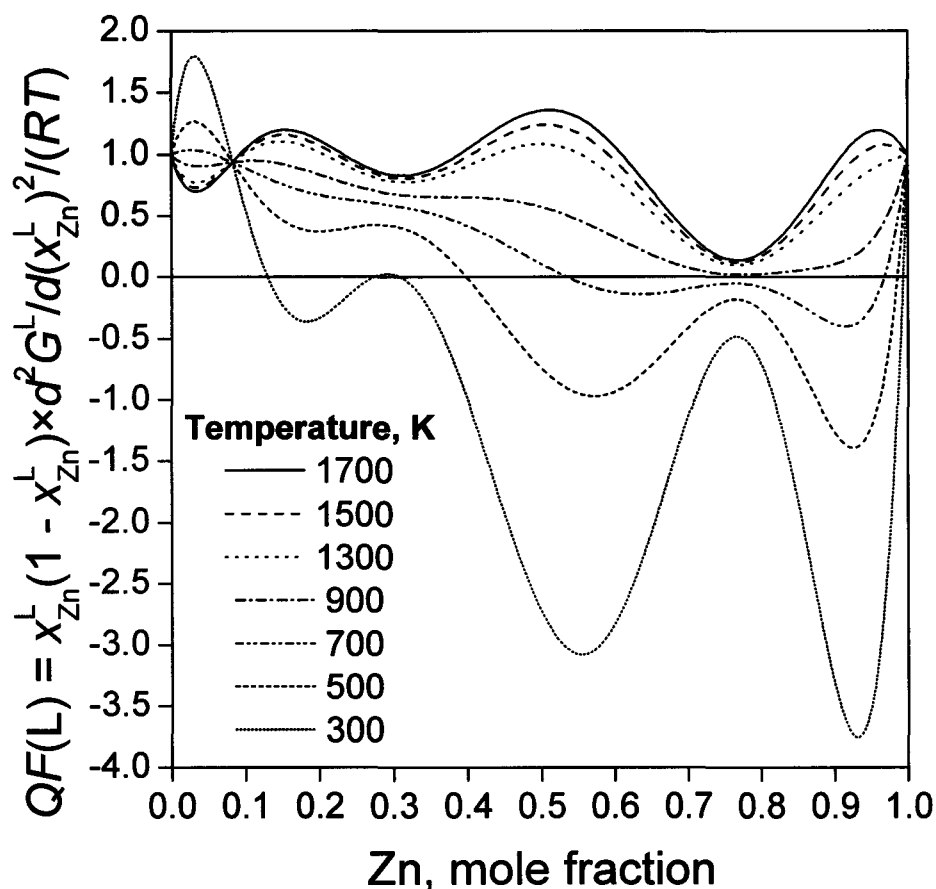


Figure 33: A plot of $QF(L)$ Vs mole fraction of Zn at different temperatures for the Bi-Zn liquid description in [127]

5.4 A non-thermodynamic example

Let us use a non-thermodynamic example for clarifying the essence of the optimization under topological constraints and introducing a specific terminology. The

kinetic example was chosen deliberately for emphasizing that the problem under consideration is rather general and not related exclusively to the CALPHAD method.

Let us consider an irreversible transformation of A to B. Assuming that this is a first-order reaction $A \rightarrow B$, one can write the following equation for the rate of transformation w_1 :

$$w_1 = -dC_A/dt = k_1 C_A \quad (5.3)$$

where C_A is a concentration of A, t is time and k_1 is the kinetic constant. Integration of (5.3) gives the expression relating a current concentration of A to time:

$$C_A = C_A^0 \exp(-k_1 t) \quad (5.4)$$

where C_A^0 is the initial concentration of A. If the transformation is thought to be a second-order reaction $2A \rightarrow B$, the rate of transformation w_2 is described by the following equation:

$$w_2 = -dC_A/dt = 2k_2 C_A^2 \quad (5.5)$$

where k_2 is the kinetic constant. Integration of (5.5) results in the following expression showing how a concentration of A varies with time:

$$C_A = C_A^0 / (1 + 2k_2 C_A^0 t) \quad (5.6)$$

Now let us consider an imaginary experiment, in which concentrations of A were measured at various times. Even though a detailed mechanism of the reaction may be unknown, it is very tempting to describe kinetics of transformation by using physically feasible models, *i.e.* by employing (5.4) or (5.6). Figure 34 shows that none of these

equations provides an acceptable accuracy of fitting of “experimental data”, which indicates that transformation of A to B is likely a multi-stage process.

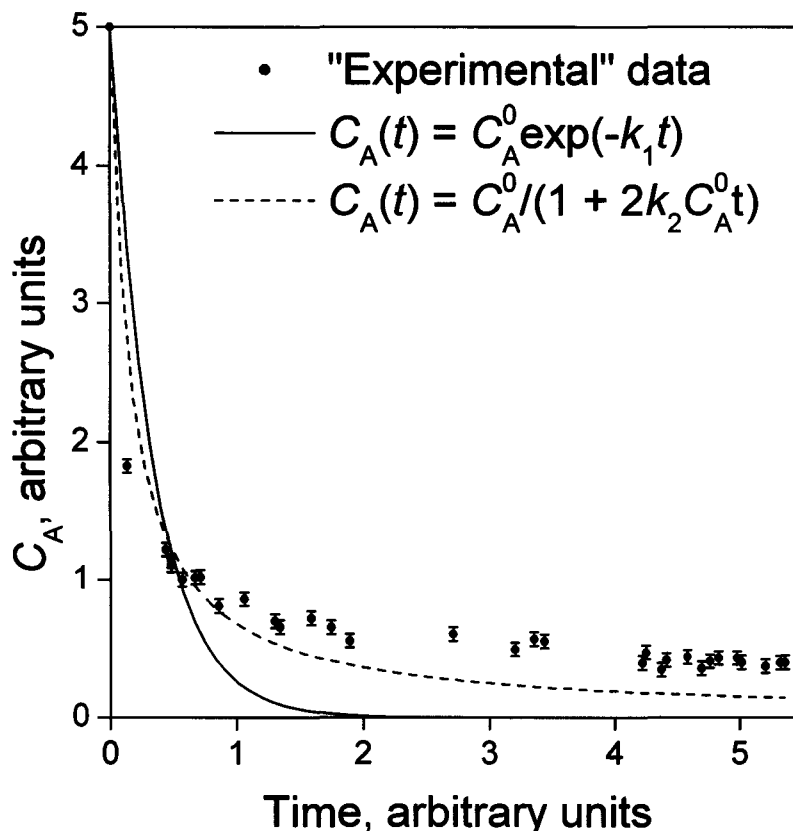


Figure 34: Fitting of kinetic data with physically feasible models

If the mechanism of the transformation is revealed, then its rate can be described by an expression, which would not be as simple as (5.4) and (5.6), but which will be physically justified. What is one supposed to do if the mechanism is not comprehended yet?

Although there is no unambiguous answer to this question, various mathematical

expressions can be tried for describing the $C_A(t)$ dependence. Let us take a polynomial fractional function as such expression:

$$C_A(t) = \frac{\sum_{i=0}^m a_i t^i}{\sum_{j=0}^n b_j t^j} \equiv P_m(t)/P_n(t) \quad (5.7)$$

Unknown coefficients \bar{a} and \bar{b} in (5.7) can be found by solving the following non-linear least squares problem:

$$\sum_{k=1}^N \omega_k \left(C_{A,k}^{\text{exp}} - \frac{\sum_{i=0}^m a_i t_k^i}{\sum_{j=0}^n b_j t_k^j} \right)^2 \rightarrow \min(\bar{a}, \bar{b}) \quad (5.8)$$

where N is a total number of measurements, $C_{A,k}^{\text{exp}}$ is the concentration of A measured at time t_k , and $\omega_k = (\Delta C_{A,k}^{\text{exp}})^{-2}$ is the statistical weight of the k -th measurement. Before proceeding with the optimization, it is worth pointing to certain relationships existing between the adjustable coefficients.

Since $C_A(t=0) = C_A^0$, it can be concluded that $a_0/b_0 = C_A^0$. However, such a conclusion is wrong since the value of C_A^0 is known only approximately; the condition $a_0/b_0 = C_A^0$ should be replaced with requirement that a_0 and b_0 have the same sign.

When time tends to infinity, the concentration of A should approach zero and remain positive. It can easily be shown that this requirement is satisfied if $n > m$, and a_m and b_n have the same sign.

Now let us recall that the transformation of A to B is deemed an irreversible one. If so, the following two conditions must be fulfilled: $(dC_A/dt)_{t=0} < 0$ and

$\lim_{t \rightarrow \infty} (dC_A/dt) = 0^-$. While the latter condition does not impose new constraints on \bar{a} and \bar{b} , the former one demands that $a_1 b_0 < a_0 b_1$. Since the constraints imposed by the physical nature of the transformation of A to B are related not to positions of individual experimental points but to such basic properties of the $C_A(t)$ function as its sign and shape, they can be named topological or geometrical constraints. An optimization under such constraints can be named isogeometrical or isotopological optimization.

Now let us try to fit the “experimental” kinetic data by using the function $P_m(t)/P_n(t)$ defined by (5.7). If due to some reasons it is intended to describe the “experimental results” very accurately, then it seems justified to use a polynomial fractional function with a great number of coefficients. Let us, for instance, try the function with $n = 4$ and $m = 5$. Although Figure 35 demonstrates that the experimental quantities were reproduced with superb accuracy, the mathematical “model” used is incorrect and should be rejected. This verdict is based on the fact that the reaction is irreversible and that, therefore, the concentration of A can only decrease in time.

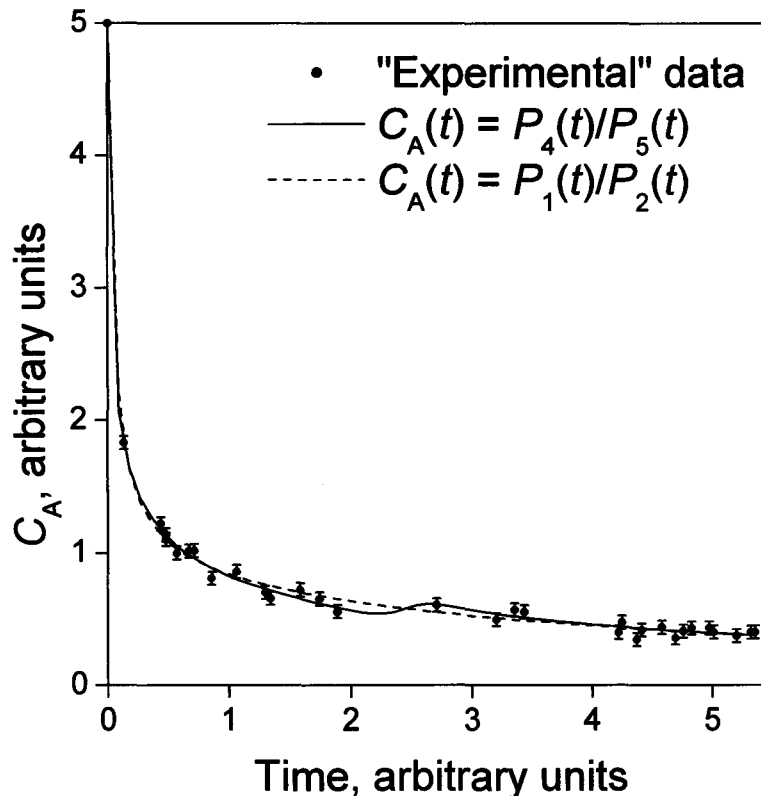


Figure 35: Fitting of kinetic data with formal mathematical expressions

Figure 35 suggests that an acceptable description of experiment can be obtained if a function with a lesser number of parameters is utilized. However, the approach “let us use different m and n and see what will happen” is not very attractive. Is it possible to arrive at a physically sound expression without being overly concerned with the number of adjustable coefficients in the polynomial fractional function? For answering this question, let us realize that an expression used for describing $C_A(t)$ can be declared physically feasible if at least the following conditions are satisfied

$$C_A(t) > 0, 0 \leq t < \infty \quad (5.9)$$

$$dC_A(t)/dt < 0, 0 \leq t < \infty \quad (5.10)$$

The three conditions derived above (a_0 and b_0 have the same sign, a_m and b_n have the same sign and $a_1 b_0 < a_0 b_1$) were related to two limiting cases: $t = 0$ and $t \rightarrow \infty$. Even if the above conditions are fulfilled, it is not guaranteed that the conditions (5.9) and (5.10) are satisfied for an arbitrarily taken time. Moreover, even the following $2N$ conditions

$$P_m(t_i)/P_n(t_i) > 0, i = 1, \dots, N$$

$$\left(d(P_n(t)/P_m(t))/dt \right)_{t=t_i} < 0, i = 1, \dots, N$$

do not ensure that (5.9) and (5.10) would be valid since the polynomial fractional function may still demonstrate an extremum or have a negative value between the experimental points or beyond the region where the experiment was conducted. For making an analytical expression describing the rate of transformation of A to B physically reasonable, a sufficiently dense mesh of knots, $\tau_j, j = 1, \dots, M$ has to be introduced. Positions of the knots τ_j are not necessarily related to times t_i , at which the concentrations of A were measured. It is quite possible that there will be several knots between t_i and t_{i+1} , and that the mesh will stretch well beyond t_N . Once the mesh is generated, the following conditions can be imposed on the solution of the least-squares problem (5.8):

$$P_m(\tau_j)/P_n(\tau_j) > 0, j = 1, \dots, M$$

$$\left(d(P_n(\tau)/P_m(\tau))/d\tau \right)_{\tau=\tau_j} < 0, j = 1, \dots, M$$

The curvature of the $P_m(t)/P_n(t)$ function can be controlled in the same fashion.

If, for instance, due to some physical reasons it is believed that the dependence $C_A(t)$ is

concave, additional topological constraints $(d^2(P_n(\tau)/P_m(\tau))/d\tau^2)_{\tau=\tau_j} > 0, j = 1, \dots, M$

should be imposed. The essence of the method, which will be used in the following section for a re-optimization of the Mg-Sb system, is straightforward: introduce a sufficiently dense mesh of knots, define topological constraints in the knots, and solve an optimization problem (in particular, a non-linear least squares problem) under these constraints. It is worth reiterating that the topological constraints are not related to the coordinated of discrete experimental points. They reflect such basic properties of an expression used for fitting as its sign, and signs of its first and second derivatives.

5.5 Re-optimization of the Mg-Sb system

5.5.1 Aim

The assessment of the Mg-Sb system proposed in [86] is not completely satisfactory. Firstly, not all experimental data available were taken into account. For instance, an important paper by Zabdyr and Moser [128], in which activities of Mg were measured in antimony-rich melts in a wide temperature range by means of the EMF method, was cited in [86], but was not actually taken into account. As another example, it can be mentioned that only electromotive force measurements at 850°C reported in [121] were utilized, although Eckert *et al.* presented the dE/dT values at various compositions as well.

Secondly, instead of dealing with raw experimental data, the authors of [86] made use of “processed data”. For clarifying this point, let us recall that Rao and Patil [120] employed the EMF technique for measuring activities of Mg in the liquid phase at different temperatures. Those quantities were used for calculating the enthalpy of mixing

of the liquid phase through the integration of the Gibbs-Duhem equation. Instead of using the values of activities directly, Balakumar and Medraj utilized the enthalpies of mixing, *i.e.* “processed data”. A list of such examples can be continued.

From this angle, it is not surprising that it was decided to re-assess the thermodynamic properties of the liquid phase in the Mg-Sb system by taking into account all literature data available. It should be highlighted that in this work, a complete full-fledged re-evaluation of the magnesium-antimony system was not endeavored. In particular, the thermodynamic models proposed in [86] for α -Mg₃Sb₂ and β -Mg₃Sb₂ remained intact. The reason is that this system was chosen as example, on which principles of optimization under topological constraints can be explained and exemplified.

Moreover, the liquid phase was described by the Redlich-Kister formalism with the same number of terms as used in [86]. This was done deliberately for illustrating that the model for the liquid phase could be drastically improved without changing a number of adjustable parameters.

5.5.2 Experimental data

Table 1 specifies experimental observations utilized in the present assessment. In almost all works, activities of Mg in the melt were studied by using the EMF technique, except the examination [119], in which tensimetric measurements were carried out. Characteristics of invariant equilibria were taken from [20, 124].

Table 1: Experimental data used in the present re-optimization of the magnesium-antimony system

Investigated region	Experimental errors	No. of points	Data source
Activity of magnesium in the liquid phase			
$1073 \leq T \leq 1173$ $0.03 \leq x_{\text{Mg}} \leq 0.9$	$\Delta T = 2, \Delta x = 0.01$ $\Delta E = 3 \text{ mV}$	105	[121]
$T = 1133, 1193$ $0.34 \leq x_{\text{Mg}} \leq 0.9$	$\Delta T = 2, \Delta x = 0.005$ $\Delta P_{\text{Mg}}^0 = 0.01 P_{\text{Mg}}^0$ $\Delta P_{\text{Mg}} = 0.03 P_{\text{Mg}}$	16	[119]
$T = 1123$ $0.1 \leq x_{\text{Mg}} \leq 0.9$	$\Delta T = 2, \Delta x = 0.005$ $\Delta E = 2 \text{ mV}$	8	[129]
$991 \leq T \leq 1250$ $0.0582 \leq x_{\text{Mg}} \leq 0.511$	$\Delta T = 2, \Delta x = 0.0005$ $x_{\text{Mg}} \neq 0.511: \Delta E = 1.5 \text{ mV}$ $x_{\text{Mg}} = 0.511: \Delta E = 10 \text{ mV}$	65	[120]
$911 \leq T \leq 1016$ $0.01 \leq x_{\text{Mg}} \leq 0.14$	$\Delta T = 2, \Delta x = 0.001$ $\Delta E = 2 \text{ mV}$	155	[128]
Enthalpy of mixing of the liquid phase			
$T \approx 925$ $0.8 \leq x_{\text{Sb}} \leq 0.85$	$\Delta T = 2, \Delta x = 0.015$ $\Delta(\Delta H) = 500 \text{ J/mol}$	2	[130]

Investigated region	Experimental errors	No. of points	Data source
$T = 1133$ $0.1 \leq x_{\text{Sb}} \leq 0.9$	$\Delta T = 3, \Delta x = 0.005$ $\Delta(\Delta H) = 0.065\Delta H \text{ J/mol}$	6	[20]
Phase diagram			
$0.05 \leq x_{\text{Sb}} \leq 0.95$	$T \leq 1273 : \Delta T = 2$ $1273 < T \leq 1473 : \Delta T = 3$ $T > 1473 : \Delta T = 4$ $\Delta x = 0.0025$	28	[123]
$2.2 \cdot 10^{-4} \leq x_{\text{Sb}} \leq 0.01$	$\Delta T = 3, \Delta x = 0.001$	15	[131]

5.5.3 Unconstrained thermodynamic optimization

In [86] the excess Gibbs energy of the liquid Mg-Sb was described as:

$$\Delta^E G^L = x_{\text{Mg}} x_{\text{Sb}} \sum_{i=0}^3 {}^i L (x_{\text{Mg}} - x_{\text{Sb}})^i \quad (5.11)$$

$$\text{and } {}^i L = A_i + B_i T \quad (5.12)$$

One of the aims of the Mg-Sb re-assessment is to show that a wrong model description can be improved without changing the number of adjustable parameters. Hence, initially, an unconstrained optimization was performed using the same number of model parameters used in the assessment [86] for the Mg-Sb system.

The phase diagram presented in Figure 36 demonstrates a thermodynamically impossible shape of the liquidus line HCP+L/L originating from the Mg melting point. Such a behavior is a clear indication that there is a miscibility gap in the liquid phase.

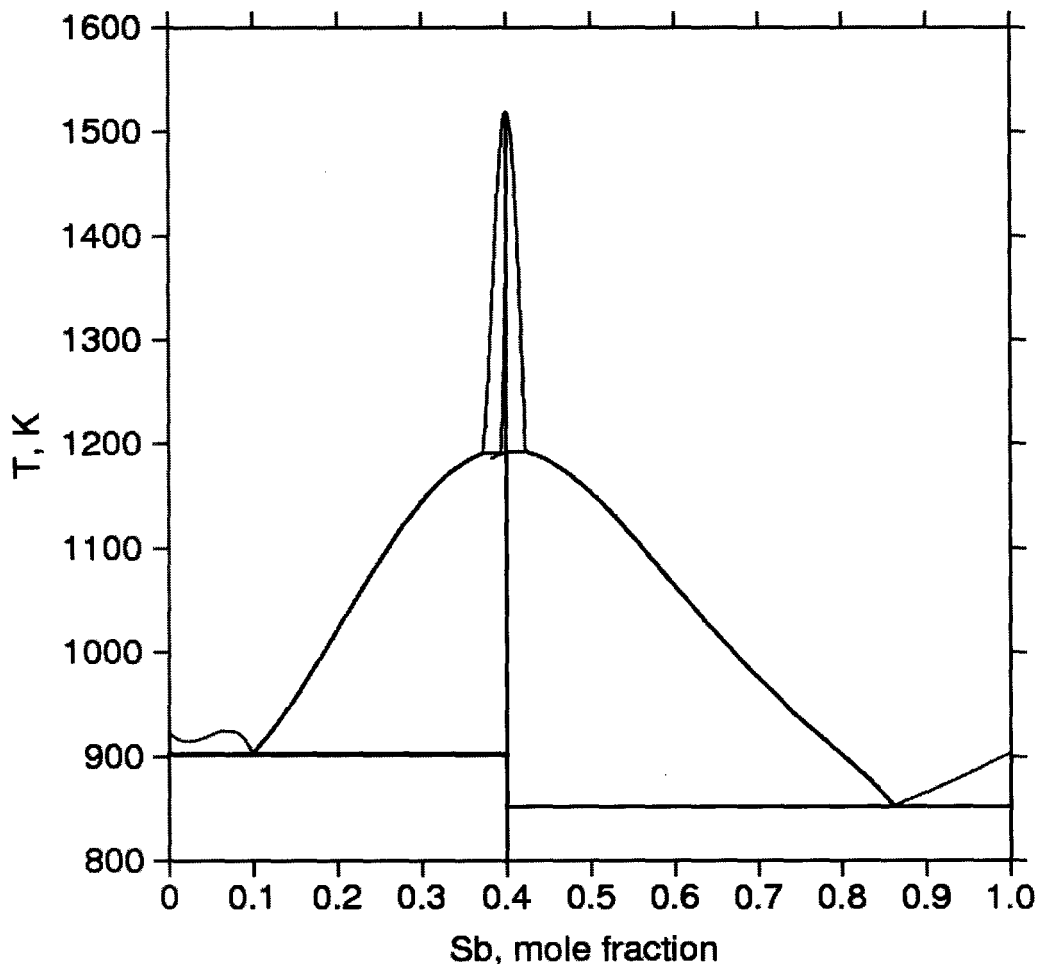


Figure 36: Phase diagram of the Mg-Sb system resulted from an unconstrained optimization

After Thermo-Calc had explained that the miscibility gap should be taken into account (this can be done by either the `AMEND_PHASE_DESCRIPTION` command in the `GIBBS_ENERGY_SYSTEM` module or the `SPECIAL_OPTIONS` command in the `POLY_3` module), the phase diagram presented in Figure 37 was calculated.

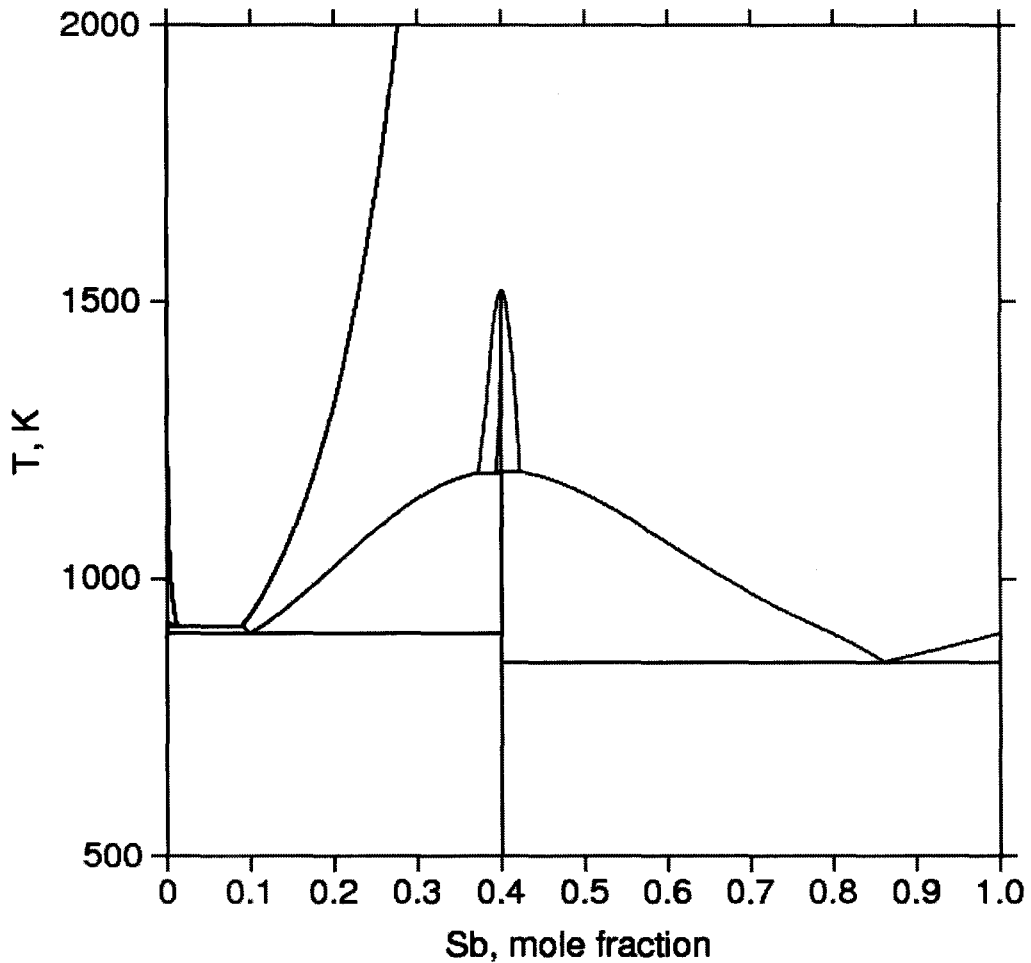


Figure 37: Phase diagram of the Mg-Sb system resulted (by the use of the Thermo-Calc command, AMEND_PHASE_DESCRIPTION) from an unconstrained optimization

Moreover, a plot of $QF\langle L \rangle$ Vs mole fraction of Sb is drawn to find the possible temperature and composition regions of inverted miscibility gap(s). An inspection of Figure 38 leads to a conclusion that another miscibility gap in the antimony-rich region will inevitably be observed at high-temperatures if additional composition sets are introduced.

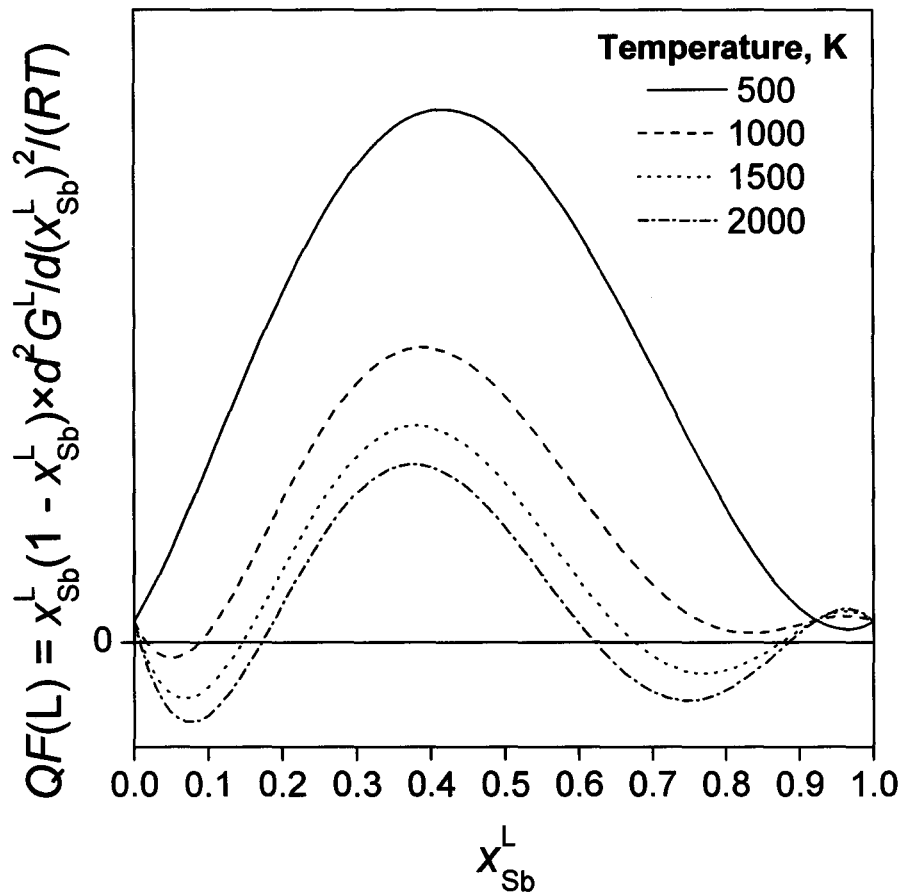


Figure 38: A plot of $QF\langle L \rangle$ Vs mole fraction of Sb at elevated temperatures: for the unconstrained optimization

From this angle, the unconstrained optimization undertaken in this work is not better than that reported in [86].

5.5.4 Topologically constrained thermodynamic optimization

Let us try to make the optimization results more reasonable. Firstly, let us focus attention on the HCP+L/L liquidus. What is known about this phase boundary? It is known that temperature decreases when the fraction of antimony increases, *i.e.* that the derivative taken along this boundary is negative

$$\frac{dT^{\text{liquidus}}}{dx_{\text{Sb}}^{\text{L}}} < 0 \quad (5.13)$$

Let us introduce a reasonably dense mesh of knots $x_{\text{Sb}}^{\text{L}} = 0.005, 0.010, \dots, 0.100$ and demand that the condition in (5.13) is satisfied in these knots. Syntax adopted for POP files allows one to do this easily:

```

CREATE_NEW_EQUILIBRIUM 970 1
ENTER_SYMBOL FUNCTION DTDX=T.X(SB) ;
CHANGE_STATUS PHASE LIQUID = FIXED 1
CHANGE_STATUS PHASE HCP_A3 = FIXED 0
SET_CONDITION P=1E5 X(SB)=0.005

LABEL ADER

EXPERIMENT DTDX<0:1E-6

TABLE_HEAD 971

CREATE_NEW_EQUILIBRIUM @@ 1
CHANGE_STATUS PHASE LIQUID = FIXED 1
CHANGE_STATUS PHASE HCP_A3 = FIXED 0
SET_CONDITION P=1E5 X(SB)=@1
EXPERIMENT DTDX<0:1E-6

LABEL ADER

TABLE_VALUES

0.010

.....

```

0.100

TABLE_END

It is worth mentioning that the mesh introduced is not related to the positions of experimental points along the HCP+L/L liquidus. This, in particular, means that the density of the mesh can be increased if necessary. Figure 39 shows the phase diagram resulted from the optimization when the condition (5.13) was employed.

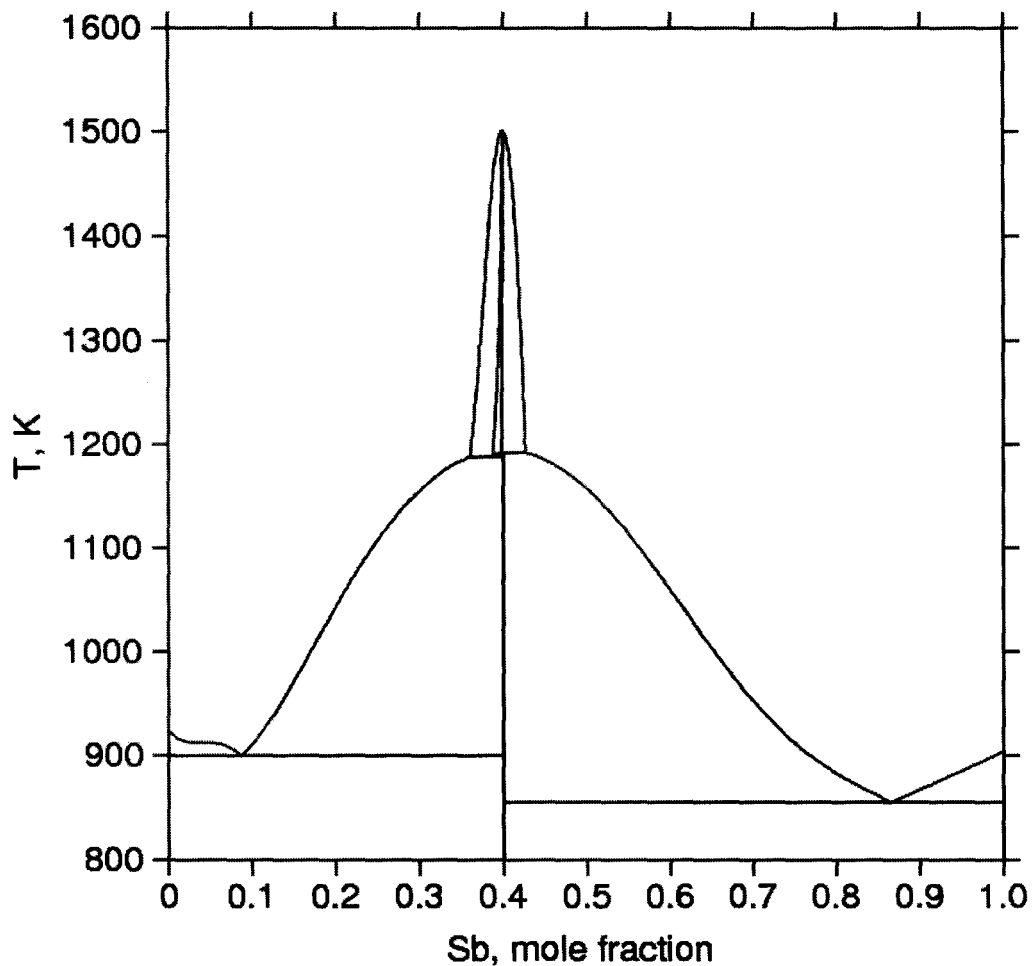


Figure 39: Phase diagram of the Mg-Sb system resulted from an optimization in the course of which topological constraints were imposed on the HCP+L/L liquidus

Figure 39 evinces that the miscibility gap in the Mg-rich region has been suppressed.

Moreover, as can be seen from Figure 40, the tendency for separation in the liquid phase in the Sb-rich region is now noticeably weaker compared to the situation shown in Figure 38. Although the tendency for separation in the liquid phase was diminished, a non-existing miscibility gap still presents in the Sb-rich region at elevated temperatures. This situation is indicated by the negative $QF(L)$ values in the Sb region at 2000 K in Figure 40.

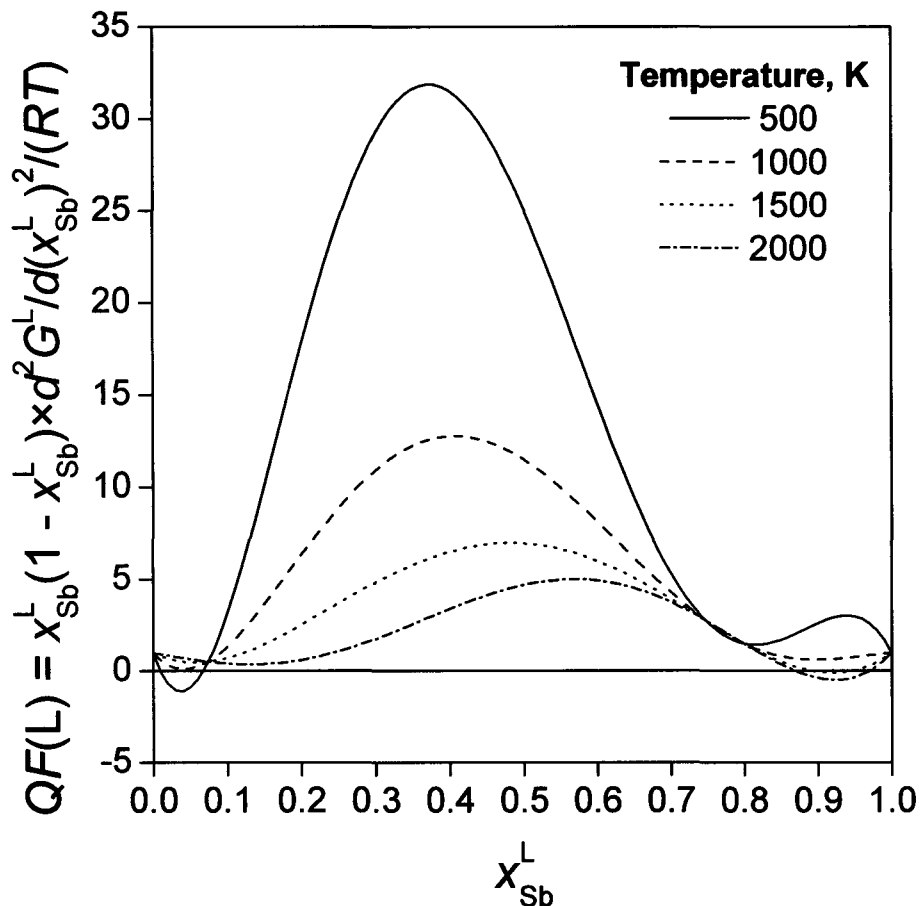


Figure 40: A plot of $QF(L)$ Vs mole fraction of Sb at elevated temperatures: topological constraints were imposed on the HCP+L/L liquidus

It is worth emphasizing that exactly the same array of experimental observations was used in the optimization, and that statistical weights of data points were not altered. The only thing brought into the optimization was the knowledge about the behavior of the liquidus line originating from the melting point of Mg.

In order to eliminate the miscibility gap in the liquid phase in the Sb-rich region at high-temperatures, let us introduce two meshes. There are no rules regulating how dense these meshes should be. In this work, the following knots were used:

$x_{\text{Sb}} = 0.02, 0.04, \dots, 0.98$ (49 x-knots), $T = 800, 1100, \dots, 2000$ (5 T-knots). Here one could wonder why the T-mesh is limited to 2000 K? The reason for the 2000 K maximum limit for the T-mesh is that the lattice stabilities for both Mg-Sb are defined only up to 2000 K.

Now let us imagine 49 vertical lines passing through the x-knots and 5 horizontal lines passing through the T-knots. These lines intersect in 245 points. Let us require that the second derivative of the Gibbs energy of the liquid phase is positive in all these intersections. This condition can be formulated by using the syntax adopted for POP files:

```
TABLE_HEAD 500
CREATE_NEW_EQUILIBRIUM @@ 1
CHANGE_STATUS PHASE LIQUID = FIXED 1
SET_CONDITION P=1E5 X(SB)=@1 T=@2
EXPERIMENT QF(LIQUID) > 0:1E-6
LABEL ATOP
TABLE_VALUES
```

0.020000 800.00

0.040000 800.00

.....

0.960000 2000.00

0.980000 2000.00

TABLE_END

By introducing such constraints, the optimization procedure was in fact explained in explicit and unambiguous terms how the Gibbs energy of the liquid phase was supposed to behave at high-temperatures. The phase diagram resulting from this “assisted assessment” and shown in Figure 41 is as good as that in Figure 39.

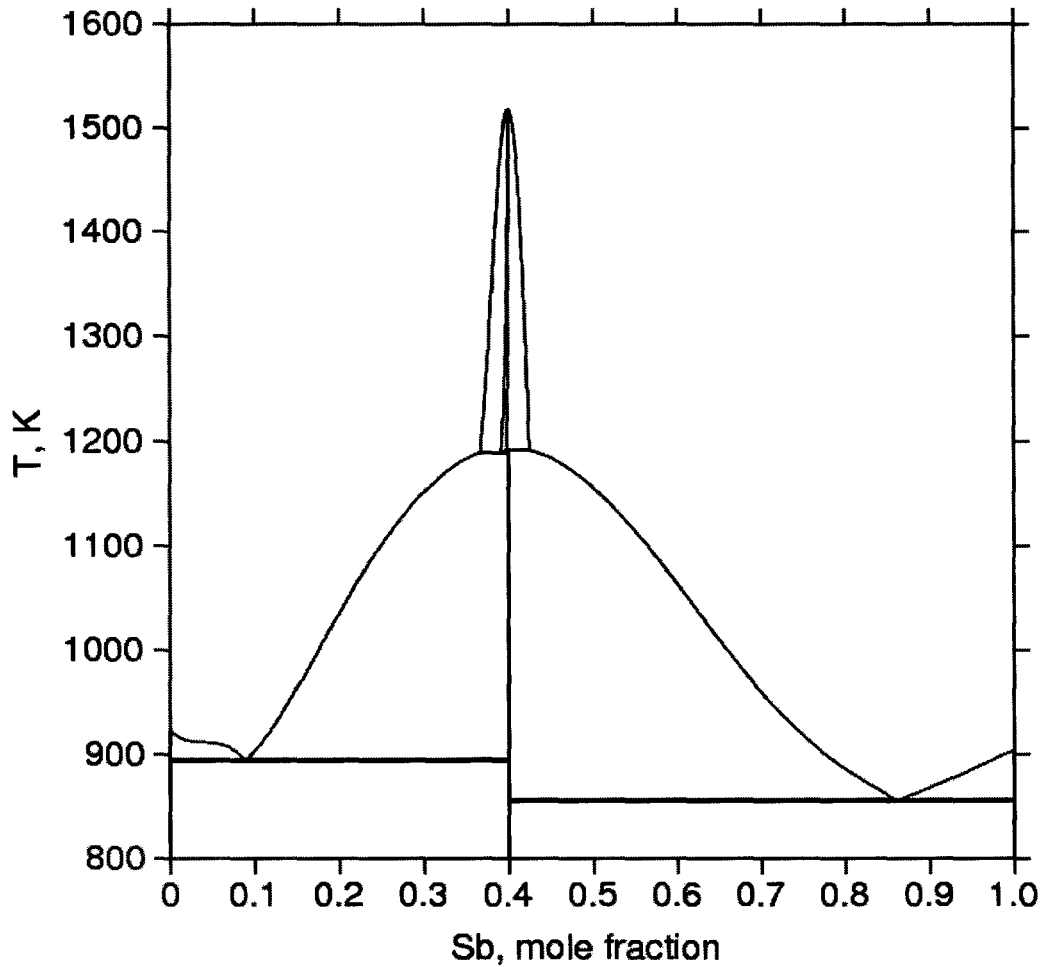


Figure 41: Phase diagram of the Mg-Sb system resulted from an optimization in the course of which topological constraints were imposed on the HCP+L/L liquidus and on the sign of $\partial^2 G^L / \partial (x^L)^2$

Figure 42 evidences that high-temperature miscibility gaps do not spoil any longer the analytical expression for the Gibbs energy of the liquid phase, which is still the habitual Redlich-Kister expression with the interaction parameters given in the last column of Table 2.

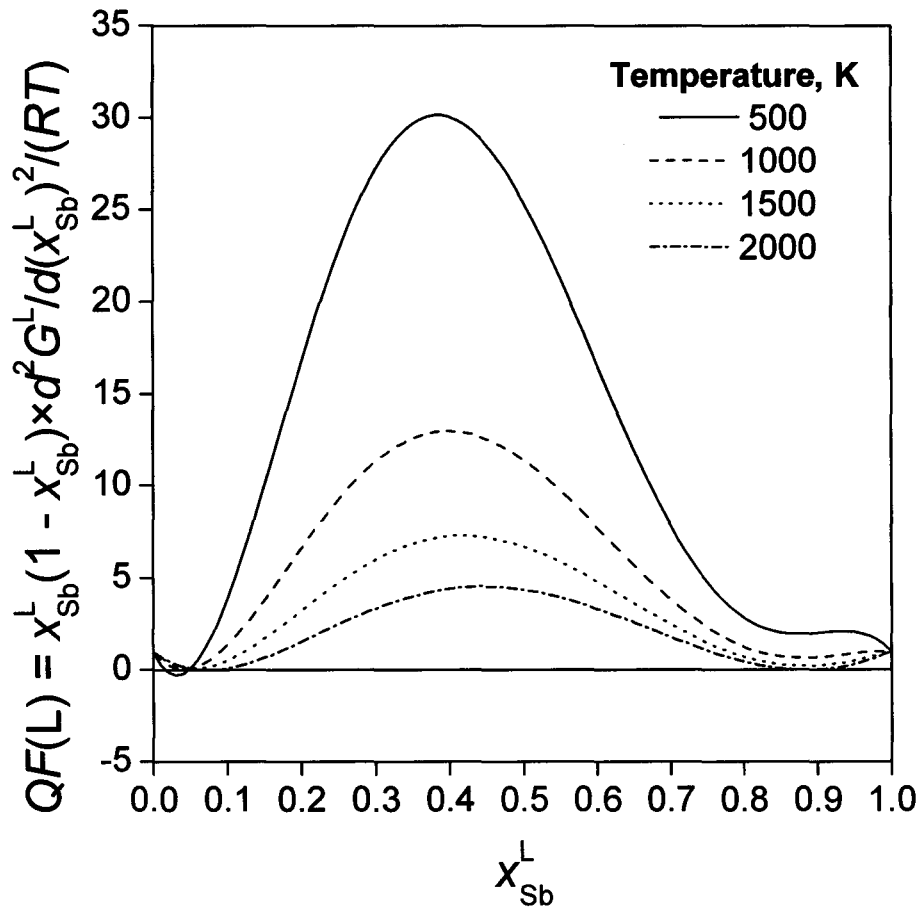


Figure 42: A plot of $QF\langle L \rangle$ Vs mole fraction of Sb at elevated temperatures: topological constraints were imposed on the HCP+L/L liquidus and on the sign of $\partial^2 G^L / \partial (x^L)^2$

At 2000 K, the positive $QF\langle L \rangle$ values, which can be seen from the above Figure 42 shows that the optimization under topological constraints suppressed all inverted miscibility gaps.

Table 2: Numerical values of the interaction parameters resulted from unconstrained and constrained optimizations of the Mg-Sb system (a reference to a figure showing a phase diagram calculated with the given set of coefficients is given in the parentheses)

Redlich-Kister Interaction parameter	Coefficient	[86] (Figure 31)	Unconstrained optimization (Figure 37)	Good HCP+L/L liquidus (Figure 39)	Good HCP+L/L liquidus and suppressed miscibility gaps (Figure 41)
0L	A_0	-172660.521	-204268.913	-190531.145	-196161.385
	B_0	44.865	77.7094660	61.6683793	68.1905674
1L	A_1	-157139.842	-20740.8120	-100388.175	-72628.8468
	B_1	123	-33.5415735	59.5786533	27.0279537
2L	A_2	29500	642.281385	36066.3661	37618.5447
	B_2	10.637	49.3656803	9.69794077	7.18917507
3L	A_3	127386.016	-42532.6243	89854.6138	53838.3015
	B_3	-98.78	93.3910054	-59.9231317	-19.3458399

5.5.5 Discussion

Figure 43 shows that the calculated molar Gibbs energies at $T = 1000$ K are quite similar for various assessments, which is not surprising since all assessments took into account numerous experimental observations in the vicinity of this temperature. The Gibbs energies, however, become very different at $T = 2000$ K .

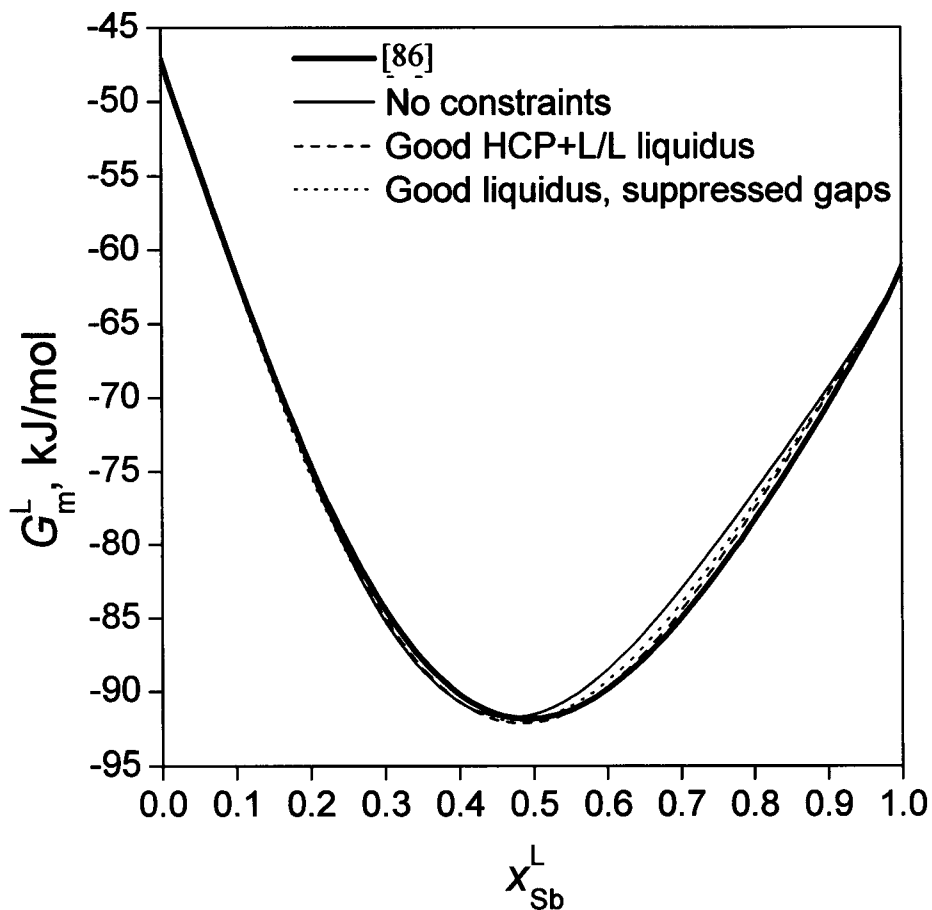


Figure 43: Comparison of the molar Gibbs energies of the liquid phase at 1000 K resulted from unconstrained and topologically constrained optimizations

Figure 44 depicts a beneficial effect the topological constraints have upon the behavior of G_m^L at elevated temperatures.

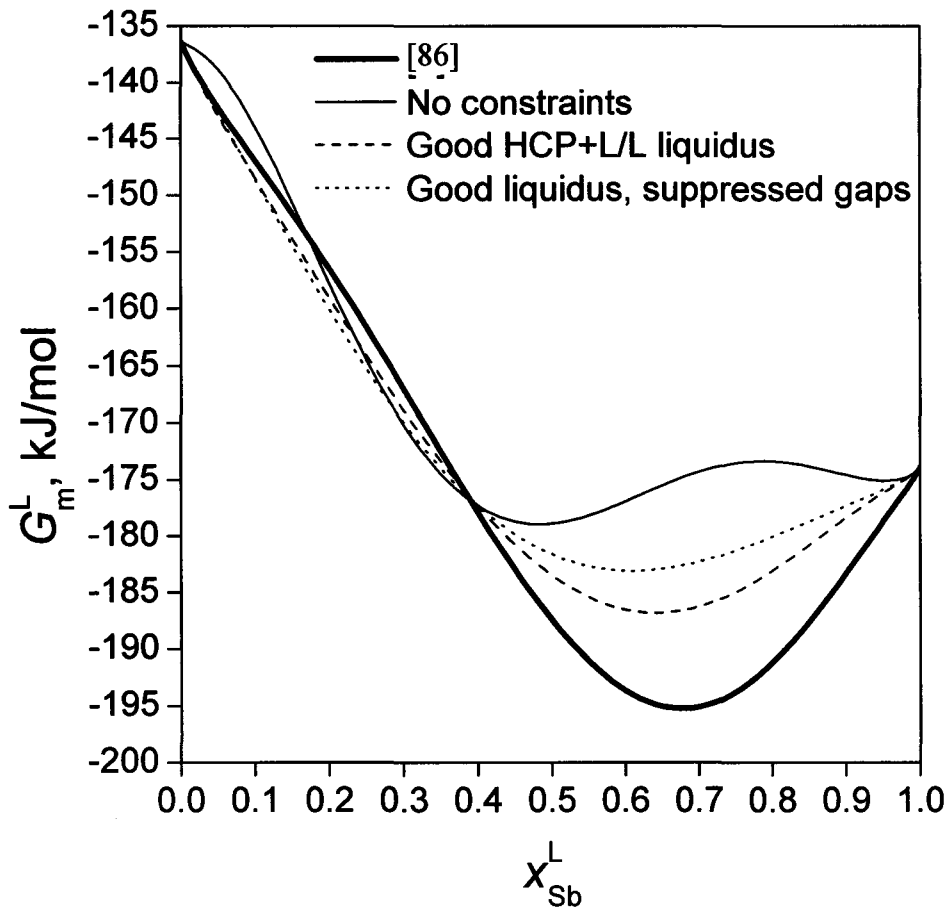


Figure 44: Comparison of the molar Gibbs energies of the liquid phase at 2000 K resulted from unconstrained and topologically constrained optimizations

The example considered means that one already has useful tools within the PARROT module for struggling against the “phantoms of optimization.” If, for instance, a solid phase becomes stable again at high-temperatures, *i.e.* at temperatures when only the liquid phase should exist, one can introduce x- and T-meshes and require that in corresponding points the molar Gibbs energy of the solid phase must be greater than that of the liquid phase. In the example above, both the x-mesh and the T-mesh were equidistant ones, but a more sophisticated choice of points, in which the condition

$G_m^L(x, T) - G_m^\alpha(x, T) < 0$ is to be enforced, can be made. If the liquid phase becomes unnaturally stable at low-temperatures, then by using the same approach, its molar Gibbs energy can be forced to be greater than the molar Gibbs energy of any solid phase. However, there are cases, for which Thermo-Calc in general and its PARROT module in particular are not equipped with necessary tools. If, for instance, a phase boundary is burdened with an excessive number of inflexion points, then one might want to control the curvature sign in knots introduced. Regretfully, second derivatives cannot be directly computed by Thermo-Calc, which means that the sign of d^2T/dx^2 cannot be forced to be positive or negative in certain knots.

5.6 Conclusions

A classical CALPHAD-style assessment is essentially a solution of an unconstrained non-linear least squares problem. The optimality criterion requires that the sum of weighted residuals should be minimal, which means that nothing can be used in the optimization procedure but discrete results of experimental observations and statistical weights assigned to them. In this chapter, it is proposed to take into account not only quantitative data but also qualitative knowledge about the behavior of the Gibbs energies of phases and phase boundaries.

By using a re-optimization of the Mg-Sb system as an example, it was shown that topological constraints defined on a specially constructed mesh of knots could dramatically improve the reliability of the CALPHAD method.

A reasonable temperature range to introduce topological constraints could be a temperature range within which the lattice stabilities are defined for both components of the system.

It also was demonstrated that at least one of the existing programs tailored for carrying out the thermodynamic assessment, namely PARROT, already has features allowing the optimization under topological constraints.

CHAPTER 6

Topological constraints in quick corrections to eliminate inverted miscibility gaps

6.1 Introduction

The successful application of topological constraints in eliminating inverted miscibility gap during thermodynamic optimization was presented in CHAPTER 5. Generally, correcting a phase description from such a full-scale thermodynamic optimization is a time consuming process. To make this correction process faster, two quick correction methods are proposed in this chapter.

The quick correction methods proposed in this chapter eliminate inverted miscibility gaps in the liquid phase at elevated temperatures *via* a computationally straightforward correction of the excess Gibbs energy of the melt are proposed. Both methods employ optimization under topological constraints controlling the sign of the second derivative of the Gibbs energy of mixing with respect to concentration. Their applicability is exemplified on the Sn–Zr system whose thermodynamic description incorporated in the COST 507 database leads to an unintended inverted miscibility gap.

6.2 The Sn-Zr system

The selected Sn-Zr system to show the workability of the quick correction methods proposed in this chapter, has been assessed three times. As Table 3 shows, in all cases, the Redlich-Kister formalism $\Delta^{\text{ex}}G = x(1-x) \sum_{i=0}^n L_i (1-2x)^i$ with either constant or

linearly depending on temperature interaction parameters, $L_i = A_i + B_iT$, was employed for representing the properties of the melt.

Table 3: Interaction parameters used in previous assessments to describe the excess Gibbs energy of the liquid phase in the Sn–Zr system

0L	1L	2L	Data source
$-45520 - 95.46T$	$-80000 + 82.115T$	$-120000 + 80.0273T$	[79]
$-172073 - 48.377T$	Not used	Not used	[132]
-172881	-1108	Not used	[133]

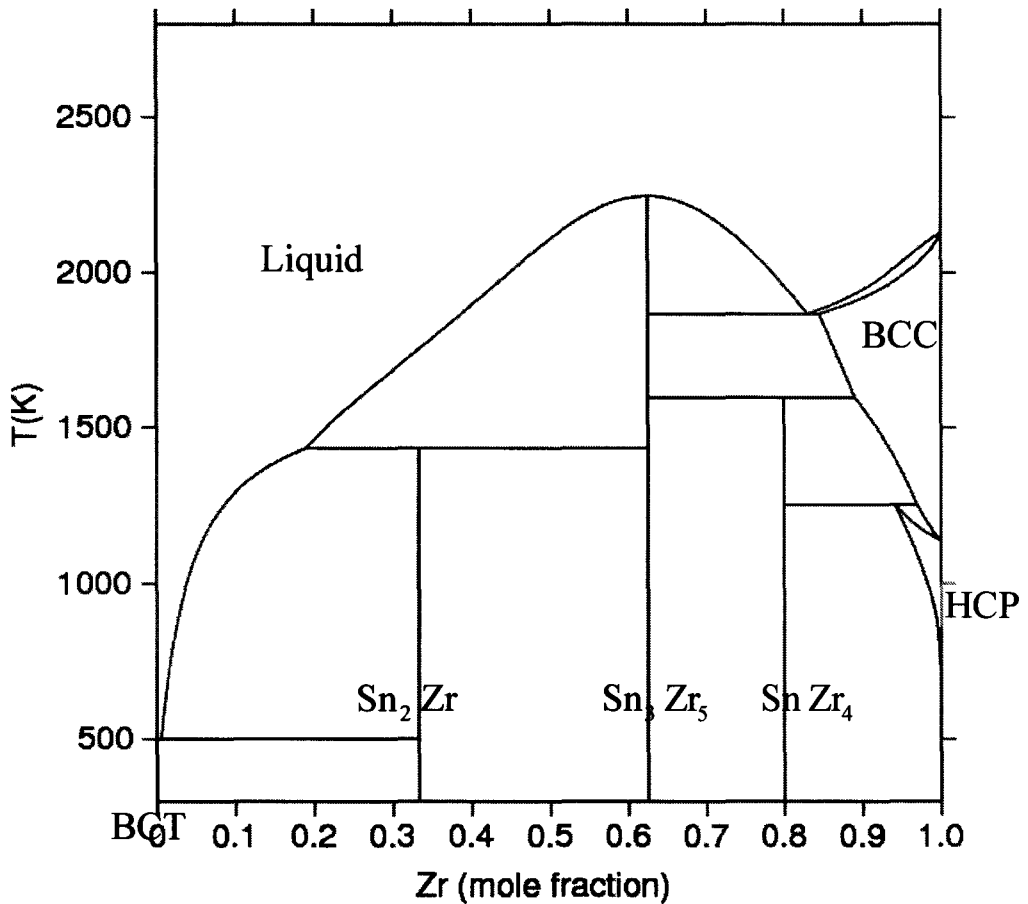


Figure 45: Phase diagram of the Sn–Zr system as presented in [79]

A calculated phase diagram of the Sn-Zr system shown in Figure 45 is identical to that in [79]. This is a normal looking diagram, but its normality stems from the fact that neither in 1996, when the system was optimized by Korb and Hack, nor in 1998, when the COST-507 database was made public, unintended equilibria were being hunted for.

After a hunting season had been opened by an availability of the next-generation phase diagram calculation software, an inverted miscibility gap in the liquid phase was discovered (see Figure 46).

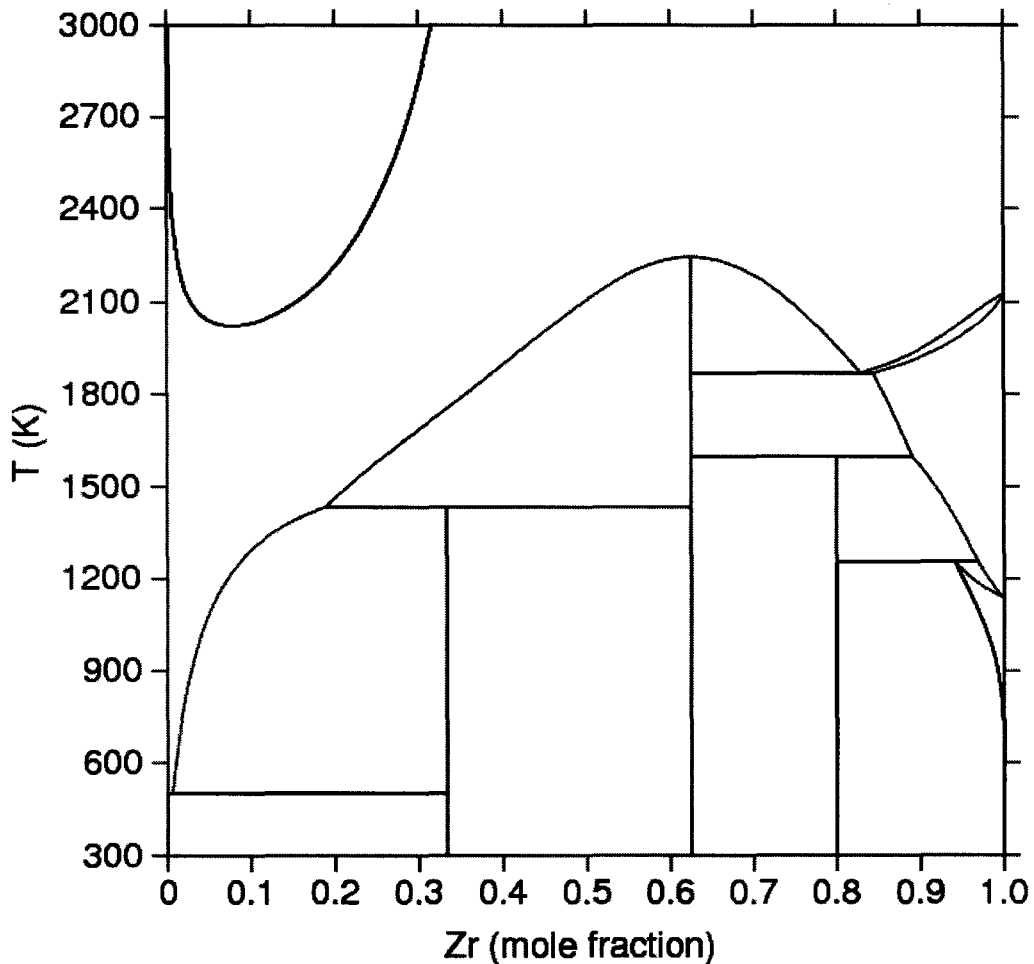


Figure 46: Phase diagram of the Sn–Zr system with an inverted miscibility gap discovered

It should be admitted that the analytical expressions for the excess Gibbs energy of the liquid phase proposed in two subsequent re-assessments of this system [132] and [133] do not result in the aforementioned artifact.

6.3 Quick correction method (I): Using a system's fingerprint during optimization

6.3.1 Aim

Instead of discarding the thermodynamic description of the tin-zirconium system proposed in [79] and forgetting it ever existed, let us try to correct it by retaining the thermodynamic properties of BCT, HCP and BCC substitutional solutions as well as the properties of all three intermediate stoichiometric phases, but changing the description of the liquid phase. An alteration of the old model should be performed in such a manner that both the phase diagram and thermodynamics of the liquid in $x - T$ regions distant from the region of immiscibility remain virtually indistinguishable from those reported in [79]. It should be accentuated that this goal can in principle be achieved by a full-fledged re-optimization of the Sn–Zr system under topological constraints similar to how it was done in chapter 5. However, neither TCM nor POP file is likely available. Collecting all publications on thermodynamic properties and conditions of phase equilibria and meticulously analyzing them for building a new experimental data file is a lengthy and boring process.

6.3.2 Fingerprinting the system

The idea pursued in quick correction method (I) is a combination of a constrained optimization and a fingerprint of the system. By analogy with a real fingerprint

differentiating one individual from others, let us adopt that particularities of invariant equilibria distinguishes one binary system from another. The liquid phase participates in four invariant reactions in the Sn-Zr system whose characteristics are given in Table 4 (x^ζ is the mole fraction of Zr in phase ζ , all temperatures are in Kelvin).

Table 4: Characteristics of invariant equilibria in the Sn–Zr system

Invariant equilibrium	Its characteristics
Eutectic $L \rightleftharpoons \text{BCT} + \text{Sn}_2\text{Zr}$	$x^L = 0.0056, T = 502.01$
Peritectic $L + \text{Sn}_3\text{Zr}_5 \rightleftharpoons \text{Sn}_2\text{Zr}$	$x^L = 0.1894, T = 1433.15$
Distectic $L \rightleftharpoons \text{Sn}_3\text{Zr}_5$	$x^L = x^{\text{Sn}_3\text{Zr}_5} = 0.625, T_m = 2244.99,$ $\Delta H^{\text{Sn}_3\text{Zr}_5 \rightarrow L}(T_m) = 89604$
Eutectic $L \rightleftharpoons \text{Sn}_3\text{Zr}_5 + \text{BCC}$	$x^L = 0.8292, x^{\text{BCC}} = 0.8444, T = 1868.52$

In a majority of cases, a table similar to Table 4 is an inevitable part of a publication devoted to the optimization of a certain system. This implies that a fingerprint of the system is readily available, and that it can directly be used for creating a POP file. While a canonical POP file contains genuine experimental data, a POP file built in our case will be composed of processed data.

It is worth emphasizing that one is not prohibited from putting up an extended fingerprint through carrying out simple calculations based on the model published. For instance, it can be speculated that not only the compositions of three phases participating in an invariant reaction are important, but a heat effect of this reaction as well. It is quite

natural to see the enthalpy of a congruent melting of Sn_3Zr_5 in Table 4, but it would not be bizarre to have this table furnished with such quantities as

$$\Delta H^{L \rightarrow \text{BCT} + \text{Sn}_2\text{Zr}} = 7080 \text{ J/mol}, \quad \Delta H^{\text{Sn}_2\text{Zr} \rightarrow \text{L} + \text{Sn}_3\text{Zr}_5} = 42890 \text{ J/mol},$$

$$\Delta H^{L \rightarrow \text{Sn}_3\text{Zr}_5 + \text{BCC}} = 31454 \text{ J/mol} \quad (\text{mol in J/mol means one mole of phase in the left-hand}$$

side of a corresponding reaction equation), and to use these enthalpies of invariant transformations in the course of assessment. Also, it will not be very challenging, for instance, to calculate liquidus temperatures for a series of mole fractions and then to them during optimization. In other words, the term fingerprint is not strictly defined. One can add more and more dermal papillae by calculating more and more thermodynamic properties and fragments of phase diagram for a system of interest by using a published model of this system. All these computations are to be performed far from an inverted miscibility gap that has to be suppressed because near it the model is not trusted.

6.3.3 Procedure

Let us recall that the old model of the liquid phase, *i.e.* the model to be improved, contains six coefficients given in Table 3. If a number of new interaction parameters to be found for the liquid phase is the same (three), and if each of them still linearly depends on temperature, then an optimization procedure fed with data from Table 4 will likely result in new coefficients virtually indistinguishable from the old ones. Clearly, something else is to be used in the course of optimization. This “something” must reflect the intention to suppress the inverted miscibility gap seen in Figure 46. More specifically, the condition $\partial^2 G / \partial x^2 > 0$ must be satisfied in a certain region Ω . Technically, this can be achieved

by requesting that $QF\langle L \rangle > 0$ in this region (the relationship between $\partial^2 G/\partial x^2$ and $QF\langle L \rangle$ has already been explained in CHAPTER 5).

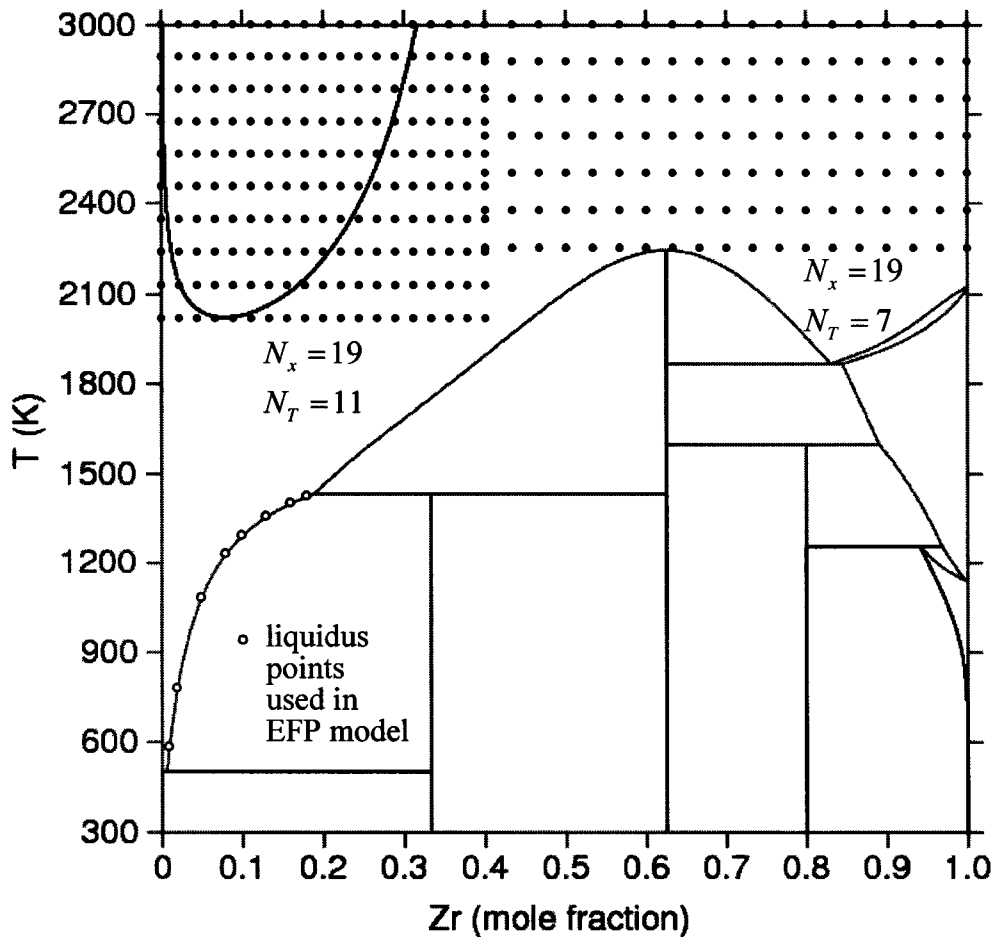


Figure 47: Location of knots at which the topological constraint $\partial^2 G/\partial x^2$ was used

Although the aforementioned region Ω within which the topological constraint $\partial^2 G/\partial x^2 > 0$ must be fulfilled can hardly be chosen in a rigorous and unambiguous manner, a reasonable choice can usually be made quite easily. A selection of the region

for the Sn-Zr system is illustrated in Figure 47. It is worth accentuating that a continuous topological constraint

$$(\partial^2 G / \partial x^2)_T > 0, \forall (x, T) \in \Omega \quad (6.1)$$

cannot be directly employed. Instead, its discrete modification

$$(\partial^2 G / \partial x^2)_T \Big|_{\substack{x=x_i \\ T=T_i}} > 0, (x_i, T_i) \in \Omega, i = 1, \dots, N \quad (6.2)$$

should be utilized. By increasing a number of knots, N , and by arranging them in such a manner that the maximum Euclidian distance between two knots is getting smaller when N is increasing, one can always ensure that (6.2) will work quite similar to (6.1). There is no rigorous and unambiguous fashion in choosing the knots within Ω . In a simple case when Ω is a rectangle in the $x-T$ space, one can introduce N_x equidistant x -knots and N_T equidistant T -knots, and then use $N = N_x \times N_T$ pairs of (x_i, T_i) needed in (6.2). As Figure 47 illustrates, in the case under consideration, Ω is comprised of two rectangles Ω_1 and Ω_2 . In total, $N = N(\Omega_1) + N(\Omega_2) = 19 \times 11 + 19 \times 7 = 342$ (x_i, T_i) pairs are used in (6.2). Despite this large number, only a fraction of topological constraints is likely active. In particular, they are inactive when $x \rightarrow 0$ or $x \rightarrow 1$ since the liquid phase is stable in dilute solution regions (the term $RT/(x(1-x))$ in $\partial^2 G / \partial x^2$ dominates).

What will happen if the Redlich-Kister formalism with three interaction parameters linearly depending on temperature is used? It can be anticipated that since the topological constraints are imposed, the phase diagram of the Sn-Zr system as well as low-temperature thermodynamic characteristics of the liquid phase may differ from those

resulting from [79], *i.e.* that they may not be in a good agreement with the experimental data the optimization [79] was based upon. If such a “spoiling effect” of constrained optimization is observed, a greater number of adjustable coefficients can be tried. At first glance, this contradicts the recommendation “Never increase the number of model parameters without an ultimate necessity” adopted by the CALPHAD community. This advice is reasonable in the case of unconstrained optimization, indeed. However, it should not be blindly followed in the case when topological constraints imposed on the Gibbs energy do not allow it to behave weirdly.

The following expression was employed for building a new excess Gibbs energy of the liquid phase:

$$\Delta^{\text{ex}}G = x(1-x) \sum_{i=0}^n {}^iL(1-2x)^i, \quad {}^iL = A_i + B_iT + C_iT \ln T \quad (6.3)$$

In addition to the basic fingerprint itemized by Table 4, an extended fingerprint was also made use of. The only difference between them is that in the latter case, 8 points belonging to the L/L + Sn₂ Zr liquidus were taken into consideration during the optimization (see Figure 47). The thermodynamic assessment was carried out by using the PARROT module of Thermo-Calc.

6.3.4 Results

Optimal numerical values of model coefficients resulting from the optimization are presented in Table 5. FP means that the basic FingerPrint was utilized; EFP delineates that the Extended FingerPrint was in use.

Table 5: Statistically optimum values of adjustable parameters in (6.3) for describing the excess Gibbs energy of the liquid phase by two alternative models

i	A_i	B_i	C_i
FP			
0	-49989.3	-72.3831	-2.80083
1	-90254.1	209.444	-16.5085
2	-165574	515.420	-55.1953
3	55.6598	-0.350371	-0.342975
EFP			
0	-56658.0	-0.668241	-11.9166
1	172907	644.961	-73.2846
2	-89001.6	56.6216	Not used

At first glance, for both FP and EFP models, a number of coefficients is dramatically greater than in the original model [79]. However, a direct comparison of these numbers is not justified since constraints employed do not allow one to treat the coefficient as truly independent.

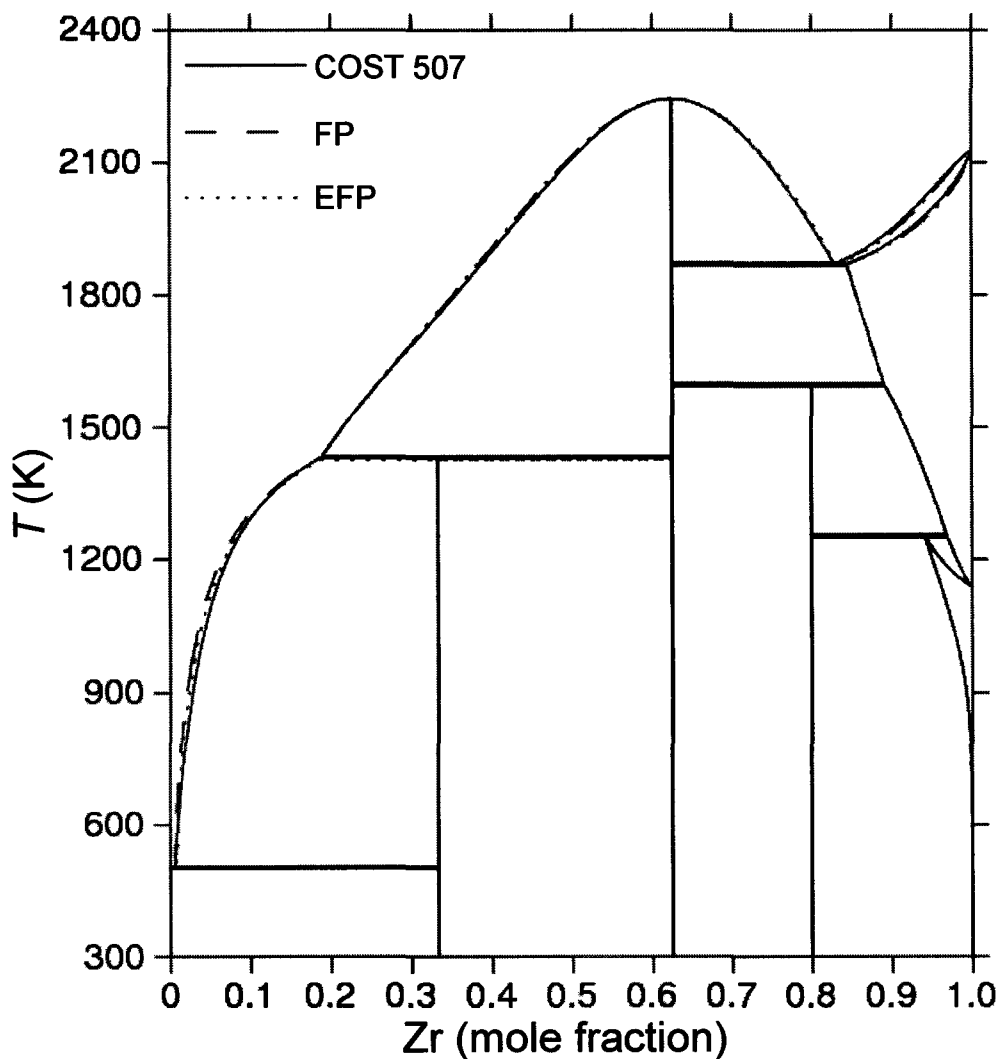


Figure 48: Phase diagrams constructed with the old and new models

Phase diagrams computed with various models are compared in Figure 48. A usage of the basic fingerprint led to the phase diagram, which is in a good agreement with the original one except the position of $L/L + \text{Sn}_2\text{Zr}$. By employing the extended fingerprint, this defect was fully eliminated. Concentration dependencies of the Gibbs energy of mixing, the enthalpy of mixing and activities of Sn and Zr resulting from

various models were compared at three different temperatures: at 1250 K (far from the inverted miscibility gap), at 1750 K (approaching the gap) and at 2750 K (the original model is invalid). As seen from Figure 49-Figure 51, low-temperature thermodynamic properties predicted by two new models closely resemble those coming from the old one.

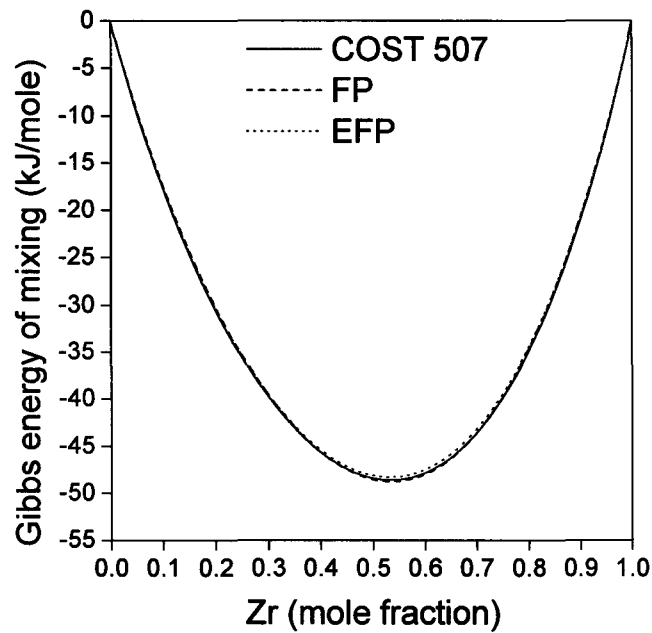


Figure 49: Molar Gibbs energies of mixing at 1250 K resulting from the old and new models

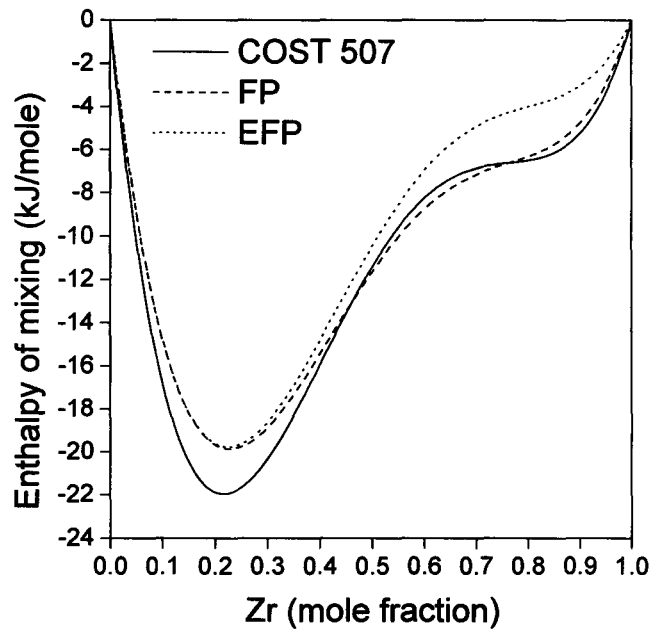


Figure 50: Molar enthalpies of mixing at 1250 K computed with the old and new models

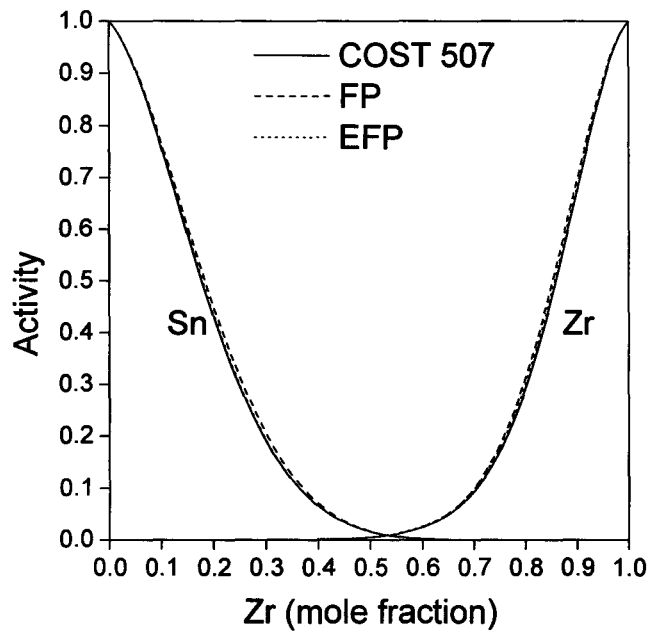


Figure 51: Activities of Sn and Zr in the liquid phase at 1250 K calculated with the old and new models

According to Figure 52-Figure 54, even when the inverted miscibility gap is being approached, *i.e.* at $T = 1750$ K, one still has a fairly good agreement between the old and new models, which is hardly surprising since a necessity to reproduce the characteristics of invariant equilibrium firmly holds new models in place.

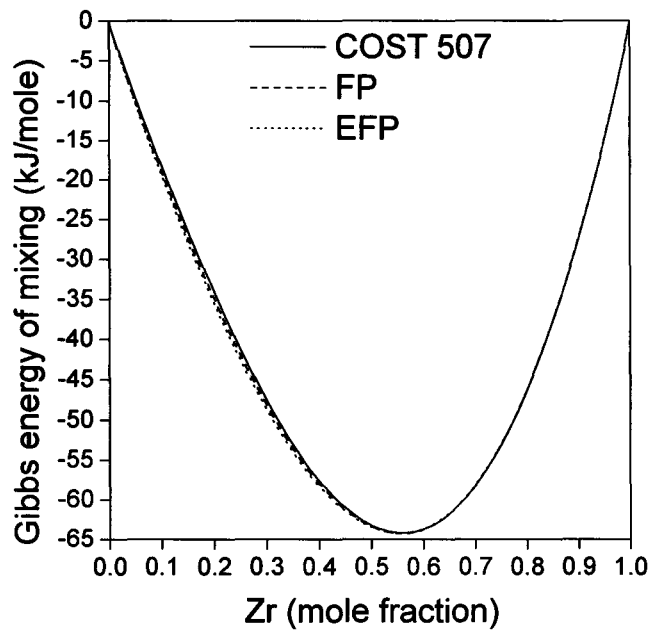


Figure 52: Molar Gibbs energies of mixing at 1750 K resulting from the old and new models

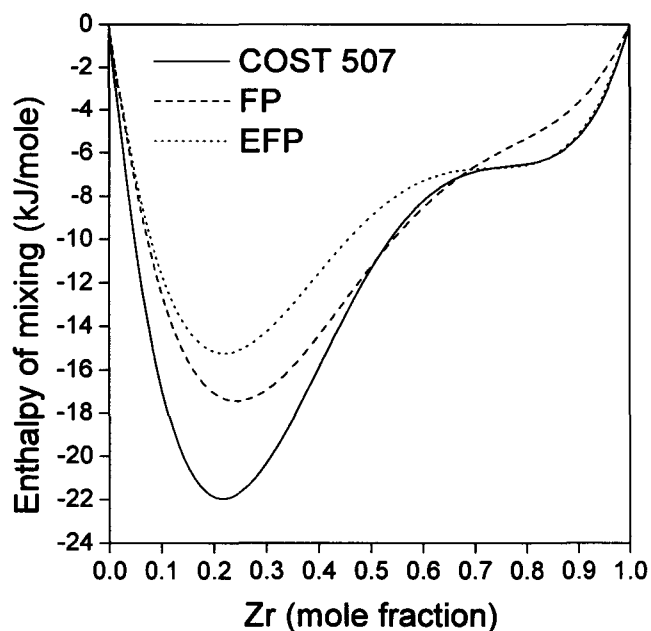


Figure 53: Molar enthalpies of mixing at 1750 K computed with the old and new models

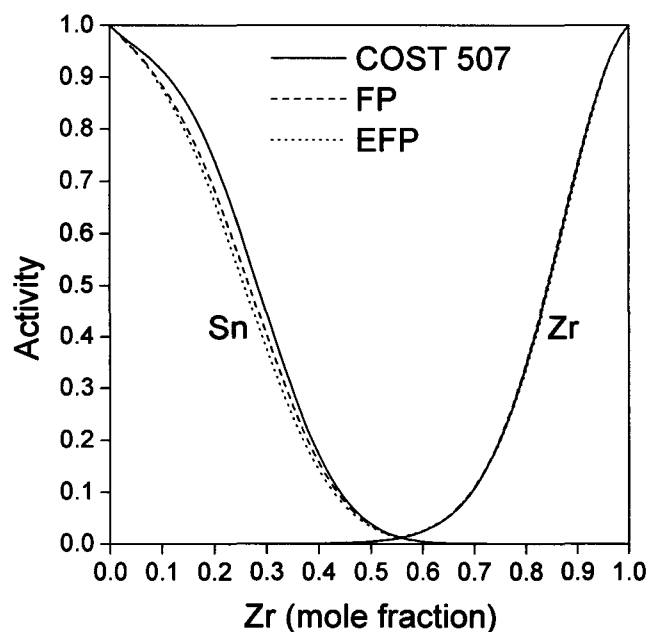


Figure 54: Activities of Sn and Zr in the liquid phase at 1750 K calculated with the old and new models

As Figure 55-Figure 57 suggest the new models deviate significantly from the old model at $T = 2750$ K. This departure is exactly what is needed, because without such a divergence the artifact could not be suppressed.

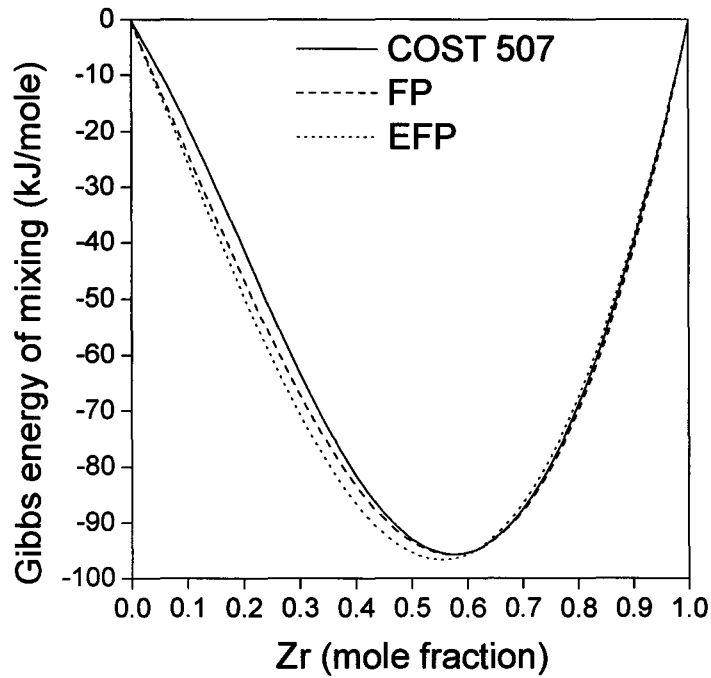


Figure 55: Molar Gibbs energies of mixing at 2750 K resulting from the old and new models

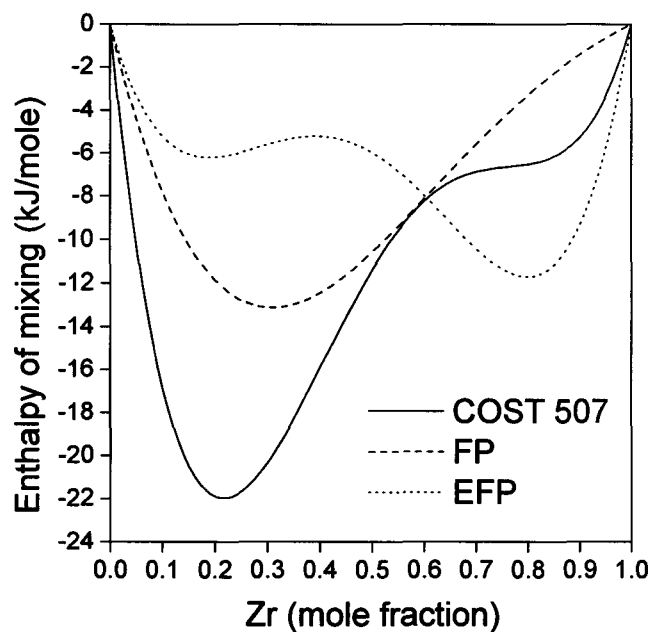


Figure 56: Molar enthalpies of mixing at 2750 K computed with the old and new models

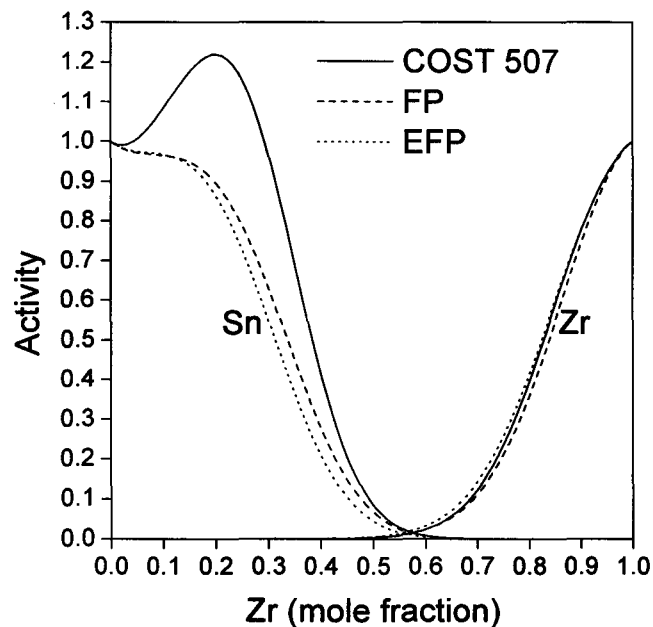


Figure 57: Activities of Sn and Zr in the liquid phase at 2750 K calculated with the old and new models

6.3.5 Discussion

It can be asked why only two particular new models are presented and discussed in this work, why a specific number of interaction parameters was utilized, *etc.* Before answering these questions explicitly, let us realize that the situation is not different from that encountered when the classical CALPHAD-type optimization is proceeded. In both cases, if a convenient mathematical formalism rather than a physically sound model is used, there is no guidance in choosing the best expression for the excess Gibbs energy a priori. Most of the time, a great deal of expressions is tried, and the best one as often as not results from trials and errors as well as from experience and sheer luck. The two particular models (see Table 5) are presented here because they work. Their existence per se stipulates that if a published assessment of a system is not perfect in the sense that it leads to a high-temperature inverted miscibility gap, then this blemish can be gotten rid of by performing an optimization under topological constraints on data easily extractable from the same publications. From the practical angle, this method is not computationally cumbersome and time-consuming.

6.4 Quick correction method (II): Retaining a correct description of the molar Gibbs energy at lower temperatures while suppressing inverted miscibility gaps at elevated temperatures

6.4.1 Aim

Let $G(x, T)$ be a function describing the Gibbs energy of the liquid phase in a binary system. This function resulted from a thermodynamic optimization of the system. It provides a good match between calculated and experimental phase diagrams as well as

between calculated thermodynamic properties and their observed counterparts. The only misfortune is that $G(x, T)$ leads to an inverted miscibility gap at elevated temperatures.

Our goal is to construct a new function $\hat{G}(x, T)$, which will be similar to G at relatively low-temperatures (e.g. inside a temperature region within which quantities used in assessment were acquired) but which will not lead to the unwanted artifact.

6.4.2 Defining the similarity

First and foremost, it is necessary to define the exact meaning of the term “similar”. When a phase diagram is calculated, both G and $\partial G/\partial x$ are used.

Thermodynamic characteristics one is normally interested in include chemical potentials (or activities), enthalpy, entropy, heat capacity along with corresponding partial molar properties. It can be concluded that if one declared G and \hat{G} as similar, then in addition to their proximity per se, propinquities of at least the following derivatives should be ensured: $\partial G/\partial x$ (chemical potentials, phase diagram), $\partial G/\partial T$ (enthalpy and entropy), $\partial^2 G/\partial x \partial T$ (partial enthalpies and entropies), $\partial^2 G/\partial T^2$ (heat capacity) and $\partial^3 G/\partial x \partial T^2$ (partial heat capacities). In general, if G and \hat{G} are to be made similar, minimization of the following objective function is to be considered:

$$\Phi = \sum_{p=0} \sum_{q=0} \alpha_{pq} \frac{\left\| \frac{\partial^{p+q} G^{\text{ex}}}{\partial x^p \partial T^q} - \frac{\partial^{p+q} \hat{G}^{\text{ex}}}{\partial x^p \partial T^q} \right\|}{\beta_{pq}} \quad (6.4)$$

where α_{pq} is a dimensionless weight (a relative importance) allocated to a corresponding derivative, and β_{pq} is a scalar whose value is equal to unity and whose dimensionality

coincides with the dimensionality of $\frac{\partial^{p+q} G^{\text{ex}}}{\partial x^p \partial T^q}$. It is natural to normalize the weight,

$\sum_p \sum_q \alpha_{pq} = 1$, and to demand that $\alpha_{00} \neq 0$ since a function cannot be restored from its

partial derivatives. $\|\varphi, \psi\|$ is a norm chosen for quantifying the difference between

functions φ and ψ . If the Euclidian norm is habitually chosen, then $\|\varphi, \psi\| = (\varphi - \psi)^2$. If

\hat{G} is a linear combination of certain basis functions, *i.e.* if $\hat{G}^{\text{ex}} = \sum_{i=1}^n g_i(x, T) \times \hat{C}_i$, then

the minimization problem (6.4) can be written as $\Phi(\hat{C}, \vec{\alpha}) \rightarrow \min$. The presence of

weights increases a dimension of the minimization space thus making the problem not easy to solve.

Instead of dealing with (6.4), let us consider a much simpler minimization problem in which only functions and their first derivatives with respect to the mole fraction are taken into account:

$$\Phi = (1 - \alpha) I_0 + \alpha I_1 \rightarrow \min(\hat{C}, \alpha) \quad (6.5)$$

where $0 \leq \alpha < 1$. I_0 and I_1 in (6.5) are defined by the following expressions:

$$I_0 = \int_{T_1}^{T_2} \int_0^1 \left(G^{\text{ex}}(x, T, C) - \hat{G}^{\text{ex}}(x, T, \hat{C}) \right)^2 dx dT \quad (6.6)$$

$$I_1 = \int_{T_1}^{T_2} \int_0^1 \left(\frac{\partial G^{\text{ex}}(x, T, C)}{\partial x} - \frac{\partial \hat{G}^{\text{ex}}(x, T, \hat{C})}{\partial x} \right)^2 dx dT \quad (6.7)$$

T_1 and T_2 are the lower and upper limits of a temperature interval within which a new excess Gibbs energy is to be similar to the old excess Gibbs energy. Integration limits in the second integral mean that \hat{G} should be made similar to G within the whole range of mole fractions from 0 to 1.

6.4.3 Procedure

Let us define τ_1 and τ_2 as the lower and upper limits of a temperature region within which the new function \hat{G}^{ex} should be correct in the sense that it does not lead to an inverted miscibility gap. Such a requirement can be formulated as the following constraint:

$$\frac{RT}{x(1-x)} + \frac{\partial^2 \hat{G}^{\text{ex}}}{\partial x^2} > 0, \forall x \in [0,1], \forall T \in [\tau_1, \tau_2] \quad (6.8)$$

where $RT/(x(1-x))$ is the second derivative of the ideal Gibbs energy of mixing.

In general, (6.5) and (6.8) represent a non-linear least squares problem with non-linear constraints whose solution may involve a numerical integration. If, however, both G^{ex} and \hat{G}^{ex} are linear with respect to corresponding parameters C and \hat{C} , *i.e.* if

$$G^{\text{ex}} = \sum_{i=1}^m f_i(x, T) \times C_i, \hat{G}^{\text{ex}} = \sum_{i=1}^n g_i(x, T) \times \hat{C}_i$$

and if the basis functions f_i and g_i are integrable, then the problem can be reduced to a linear least squares problem with linear constraints. This problem becomes especially undemanding for the case when the Redlich-Kister formalism with interaction parameters linearly depending on temperature is utilized for describing both G^{ex} and \hat{G}^{ex} , *i.e.* when

$$G^{\text{ex}} = x(1-x) \sum_{i=0}^m (1-2x)^i (C_{2i+1} + C_{2i+2}T) \quad (6.9)$$

$$\hat{G}^{\text{ex}} = x(1-x) \sum_{i=0}^n (1-2x)^i (\hat{C}_{2i+1} + \hat{C}_{2i+2}T) \quad (6.10)$$

For finding the minimum of the objective function Φ in (6.5), one has to solve the following system composed of $2(n+1)$ equations:

$$\partial\Phi/\partial C_{2k+2} = (1-\alpha) \times \partial I_0 / \partial \hat{C}_{2k+2} + \alpha \times \partial I_1 / \partial \hat{C}_{2k+2} = 0, k = 0, \dots, n \quad (6.11)$$

$$\partial\Phi/\partial C_{2k+1} = (1-\alpha) \times \partial I_0 / \partial \hat{C}_{2k+1} + \alpha \times \partial I_1 / \partial \hat{C}_{2k+1} = 0, k = 0, \dots, n \quad (6.12)$$

By using the expressions (6.6), (6.7), (6.9) and (6.10) in (6.11) and by carrying out tedious but straightforward rearrangements and simplifications, one arrives at a $2(n-1) \times 2(n-1)$ system of linear equations with respect to \hat{C} . For revealing the structure of this system, it is convenient to handle it as a combination of two systems of equations with one corresponding to partial derivatives with respect to I_0 , and another related to partial derivatives with respect to I_1 .

The first system is composed of the following $2(n-1)$ equations:

$$\sum_{i=0}^n \hat{C}_{2i+1} \Delta \psi_2(i+k) + \frac{\sum_{i=0}^n \hat{C}_{2i+2} \Delta^2 \psi_2(i+k)}{2} = \sum_{i=0}^m C_{2i+1} \Delta \psi_2(i+k) + \frac{\sum_{i=0}^m C_{2i+2} \Delta^2 \psi_2(i+k)}{2} \quad (6.13)$$

$$\frac{\sum_{i=0}^n \hat{C}_{2i+1} \Delta^2 \psi_2(i+k)}{2} + \frac{\sum_{i=0}^n \hat{C}_{2i+2} \Delta^3 \psi_2(i+k)}{3} = \frac{\sum_{i=0}^m C_{2i+1} \Delta^2 \psi_2(i+k)}{2} + \frac{\sum_{i=0}^m C_{2i+2} \Delta^3 \psi_2(i+k)}{3} \quad (6.14)$$

where k varies from 0 to n , $\Delta \equiv T_2 - T_1$, $\Delta^2 \equiv T_2^2 - T_1^2$, and $\Delta^3 \equiv T_2^3 - T_1^3$. A function $\psi_2(l)$ defined for an integer non-negative argument is:

$$\psi_2(l) \equiv \int_0^1 x^2 (1-x)^2 (1-2x)^l dx = \frac{1+(-1)^l}{4(1+l)(3+l)(5+l)}$$

The second system looks even scarier, but it is still a simple system of linear equations with respect to unknown coefficients \hat{C} :

$$\begin{aligned} & \sum_{i=0}^n \hat{C}_{2i+1} \Delta (\psi_0(i+k+2) - 2k\psi_1(i+k)) + \sum_{i=1}^n 2\hat{C}_{2i+1} \Delta (-i\psi_1(i+k) + 2ik\psi_2(i+k-2)) \\ & + \frac{\sum_{i=0}^n \hat{C}_{2i+2} \Delta^2 (\psi_0(i+k+2) - 2k\psi_1(i+k))}{2} + \sum_{i=1}^n \hat{C}_{2i+2} \Delta^2 (-i\psi_0(i+k) + 2ik\psi_2(i+k-2)) \\ & = \sum_{i=0}^m C_{2i+1} \Delta (\psi_0(i+k+2) - 2k\psi_1(i+k)) + \sum_{i=1}^n 2C_{2i+1} \Delta (-i\psi_1(i+k) + 2ik\psi_2(i+k-2)) \\ & + \frac{\sum_{i=0}^m C_{2i+2} \Delta^2 (\psi_0(i+k+2) - 2k\psi_1(i+k))}{2} + \sum_{i=1}^m C_{2i+2} \Delta^2 (-i\psi_0(i+k) + 2ik\psi_2(i+k-2)) \end{aligned} \quad (6.15)$$

$$\begin{aligned}
& \frac{\sum_{i=0}^n \hat{C}_{2i+1} \Delta^2 (\psi_0(i+k+2) - 2k\psi_1(i+k))}{2} + \frac{\sum_{i=1}^n 2\hat{C}_{2i+1} \Delta^2 (-i\psi_1(i+k) + 2ik\psi_2(i+k-2))}{2} \\
& + \frac{\sum_{i=0}^n \hat{C}_{2i+2} \Delta^3 (\psi_0(i+k+2) - 2k\psi_1(i+k))}{3} + \frac{\sum_{i=1}^n 2\hat{C}_{2i+2} \Delta^3 (-i\psi_0(i+k) + 2ik\psi_2(i+k-2))}{3} \\
& = \frac{\sum_{i=0}^m C_{2i+1} \Delta^2 (\psi_0(i+k+2) - 2k\psi_1(i+k))}{2} + \frac{\sum_{i=1}^n C_{2i+1} \Delta^2 (-i\psi_1(i+k) + 2ik\psi_2(i+k-2))}{2} \\
& + \frac{\sum_{i=0}^m C_{2i+2} \Delta^3 (\psi_0(i+k+2) - 2k\psi_1(i+k))}{3} + \frac{\sum_{i=1}^m 2C_{2i+2} \Delta^3 (-i\psi_0(i+k) + 2ik\psi_2(i+k-2))}{3}
\end{aligned} \tag{6.16}$$

where functions $\psi_0(l)$ and $\psi_1(l)$ defined for an integer non-negative argument are:

$$\psi_0(l) \equiv \int_0^1 (1-2x)^l dx = \frac{1+(-1)^l}{2(1+l)}$$

$$\psi_1(l) \equiv \int_0^1 x(1-x)(1-2x)^l dx = \frac{1+(-1)^l}{4(1+l)(3+l)}$$

When (6.13) and (6.14) multiplied by $1-\alpha$ are added to (6.15) and (6.16) multiplied by α , one ends up with a system of equations from which all unknown $2(n+1)$ component of the vector \hat{C} can be calculated. However, so far the constraint “No inverted miscibility gaps, please!” has not been taken into account.

Let us take the second derivative of the right hand side of (6.10) and substitute it in (6.8):

$$\begin{aligned} & \frac{RT}{x(1-x)} - 2 \sum_{i=0}^n (i+1)(1-2x)^i (\hat{C}_{2i+1} + \hat{C}_{2i+2}T) - 2 \sum_{i=1}^n i(1-2x)^i (\hat{C}_{2i+1} + \hat{C}_{2i+2}T) \\ & + 4x(1-x) \sum_{i=2}^n i(i-1)(1-2x)^{i-2} (\hat{C}_{2i+1} + \hat{C}_{2i+2}T) > 0, \forall x \in [0,1], \forall T \in [\tau_1, \tau_2] \end{aligned} \quad (6.17)$$

The condition (6.17) can easily be rearranged to accentuate the fact that it is a linear inequality constraint with respect to \hat{C} :

$$\begin{aligned} & \hat{C}_{2i+1} \left(- \sum_{i=0}^n (i+1)(1-2x)^i - \sum_{i=1}^n i(1-2x)^i + 2x(1-x) \sum_{i=2}^n i(i-1)(1-2x)^{i-2} \right) \\ & + \hat{C}_{2i+2} \left(- \sum_{i=0}^n (i+1)(1-2x)^i T - \sum_{i=1}^n i(1-2x)^i T + 2x(1-x) \sum_{i=2}^n i(i-1)(1-2x)^{i-2} T \right) > - \frac{RT}{2x(1-x)} \end{aligned} \quad (6.18)$$

The condition (6.18) is supposed to be valid at any point belonging to the $0 \leq x \leq 1$ and $\tau_1 \leq T \leq \tau_2$ rectangle. To make this condition suitable for applying in practice, “discrete constraints” should be introduced instead of the “continuous constraint” (6.18). This can be achieved in a fashion identical to that described in CHAPTER 5 as well as in the preceding section of this chapter:

$$\begin{aligned} & \hat{C}_{2i+1} \left(- \sum_{i=0}^n (i+1)(1-2x_p)^i - \sum_{i=1}^n i(1-2x_p)^i + 2x_p(1-x_p) \sum_{i=2}^n i(i-1)(1-2x_p)^{i-2} \right) \\ & + \hat{C}_{2i+2} \left(- \sum_{i=0}^n (i+1)(1-2x_p)^i T_q - \sum_{i=1}^n i(1-2x_p)^i T_q \right. \\ & \left. + 2x_p(1-x_p) \sum_{i=2}^n i(i-1)(1-2x_p)^{i-2} T_q \right) > - \frac{RT_q}{2x_p(1-x_p)}, p=1, \dots, N_x, q=1, \dots, N_T \end{aligned} \quad (6.19)$$

If N_x and N_T are made sufficiently large, then an effect of applying constraints (6.19) will be quite similar to that of employing (6.18). All mole fractions and temperatures seen in (6.19) are confined: $0 < x_p < 1, \forall p$ and $\tau_1 \leq T_q \leq \tau_2, \forall q$.

From the computational viewpoint, the problem in hand is a linear least-squares problem with linear constraints. Finding a solution of such a problem is challenging neither algorithmically [134] nor computationally.

For illustrative purposes, it was decided to use the following expression for the excess Gibbs energy of the liquid phase:

$$\hat{G}^{\text{ex}} = x(1-x) \sum_{i=0}^2 (1-2x)^i (\hat{C}_{2i+1} + \hat{C}_{2i+2}T)$$

It has the same number of interaction parameters as the model in [79], and all parameters linearly depend on temperature. Figure 58 shows the similarity region used in computations along with knots used in (6.19).

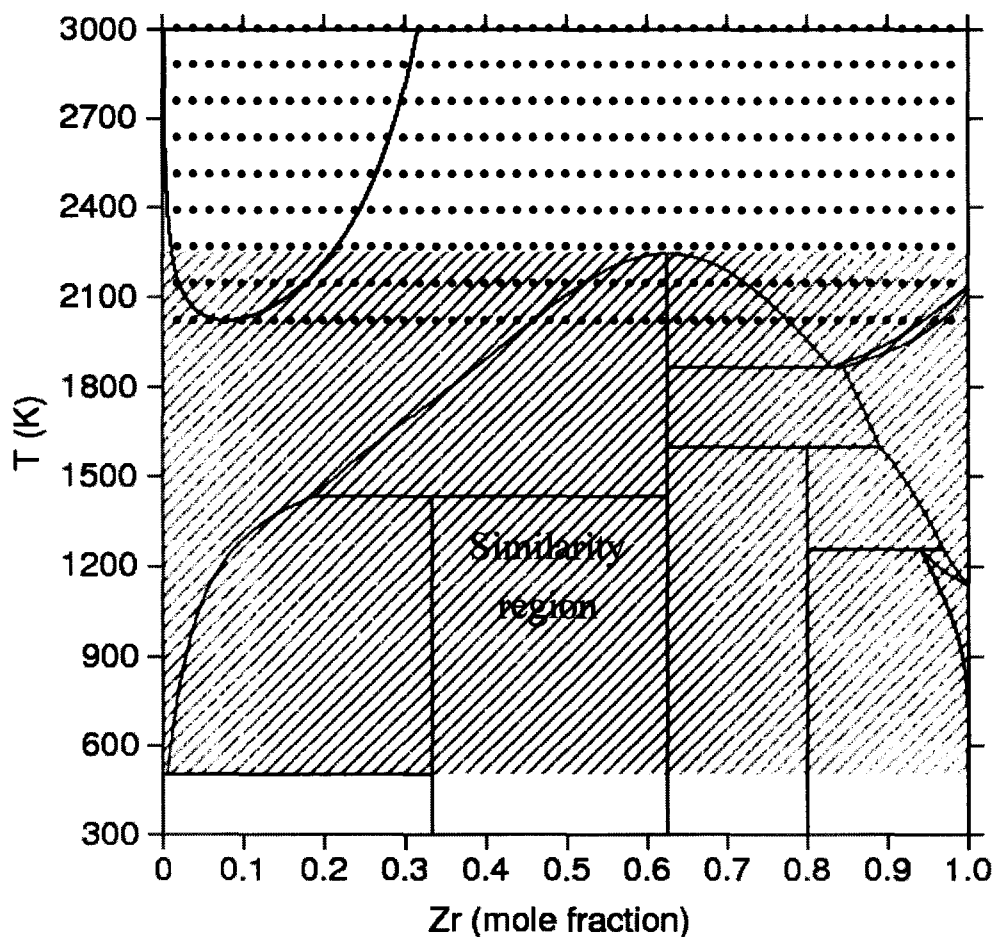


Figure 58: Hatched area is a “similarity region” within which a new model is made similar to the old model. • are knots at which the topological constraint $\partial^2 G / \partial x^2$ was employed

It may seem surprising that some knots are situated within the hatched region, but this is not an internal contradiction: similarity between the old and new models is formulated in terms of their Gibbs energies and first derivatives with respect to mole fraction, while constraints are imposed on a new model only in terms of the second derivative. A Fortran program was written for solving the system (6.13)-(6.16) with constraints (6.19).

6.4.4 Results

The optimum values of the interaction parameters found are:

$${}^0L = -58256.9 - 86.4477T, {}^1L = -77303.0 + 80.2067T, {}^2L = -33005.8 + 18.4726T$$

(6.20)

The phase diagram of the Sn–Zr system calculated with (6.20) is matched against the diagram from [79] in Figure 59.

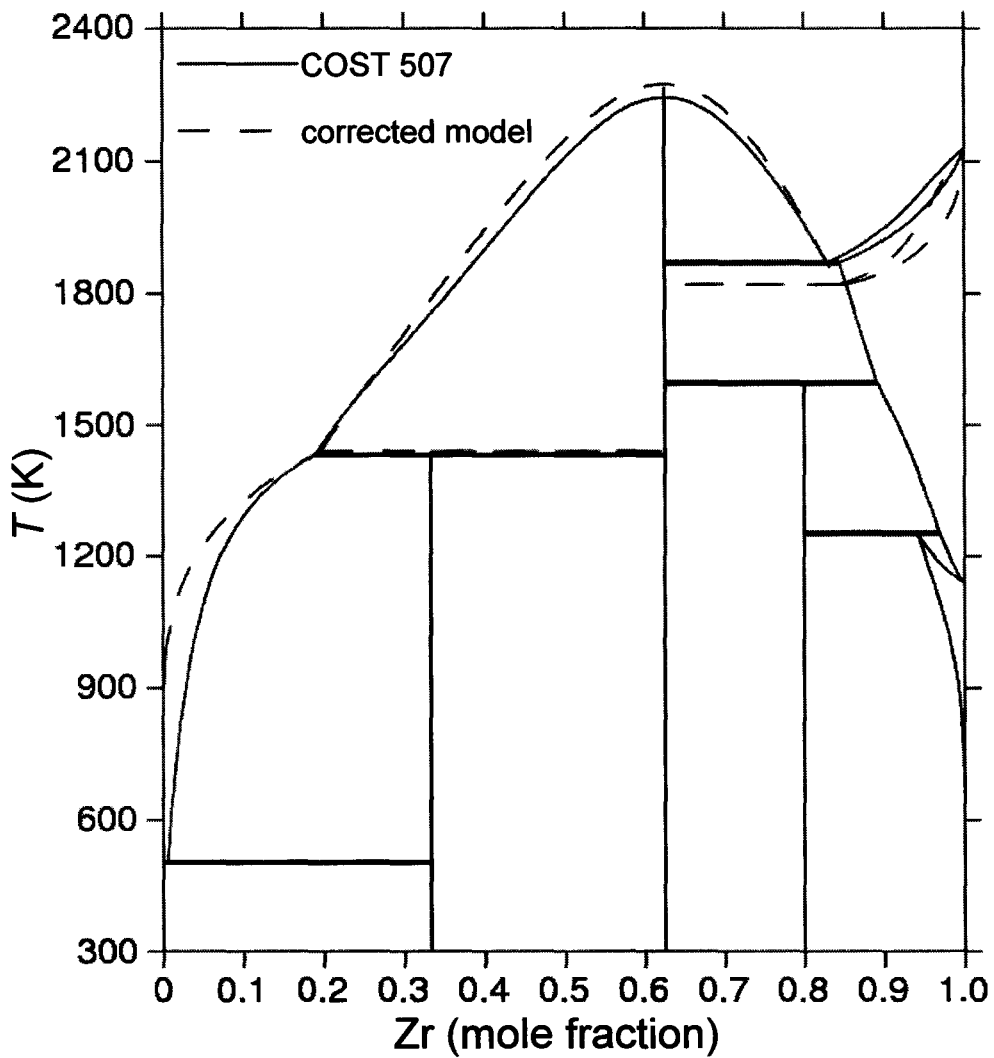


Figure 59: Phase diagrams constructed with the old and new models

An accord between two diagrams is not very impressive, which is hardly surprising since exactly the same number of coefficients was used in both expressions for the excess Gibbs energy. It can be said that this discrepancy is the price one has to pay for eliminating the post-optimization phantom without changing a mathematical essence of the old model. Temperature-independent enthalpies of mixing are compared in Figure 60.

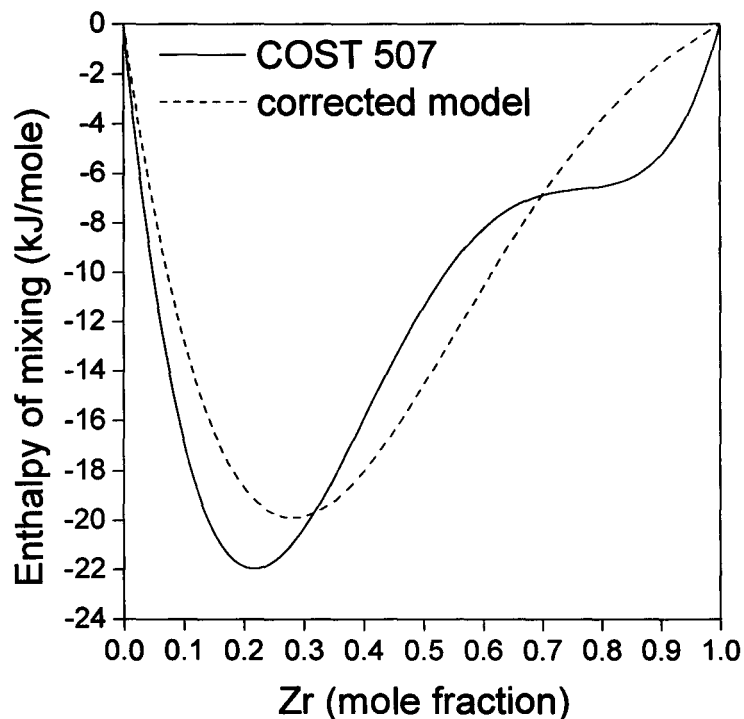


Figure 60: Temperature-independent molar enthalpies of mixing computed with the old and new models

A less wavy character of $\Delta_{\text{mix}} H(x)$ demonstrated by the new model can likely be attributed to the constraints employed. Concentration dependencies of the Gibbs energy of mixing and activities of Sn and Zr are compared at 1250 K (the old model can be trusted), 1750 K (a vicinity of the inverted miscibility gap is being approached), and

2750 K (the old model is not reliable). As Figure 61-Figure 64 suggest, an agreement between the thermodynamic properties resulting from two models is quite satisfactory at low and intermediate temperatures.

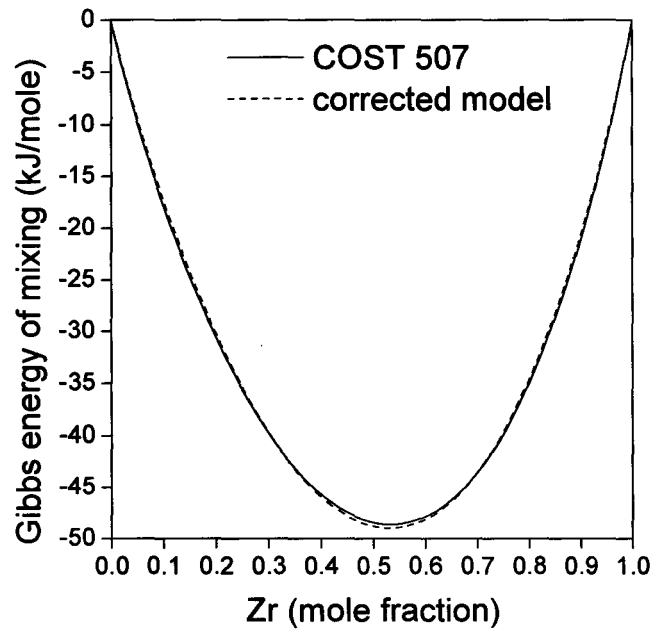


Figure 61: Molar Gibbs energies of mixing at 1250 K resulting from the old and new models

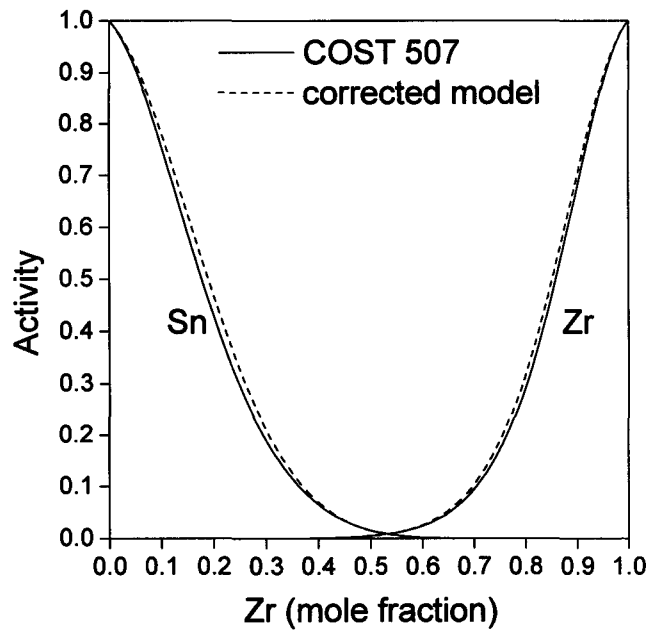


Figure 62: Activities of Sn and Zr in the liquid phase at 1750 K calculated with the old and new models

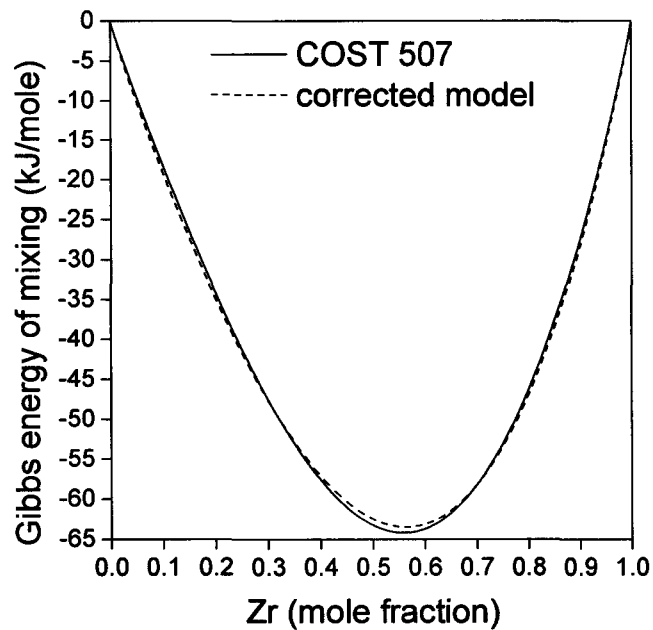


Figure 63: Molar Gibbs energies of mixing at 1750 K predicted by the old and new models

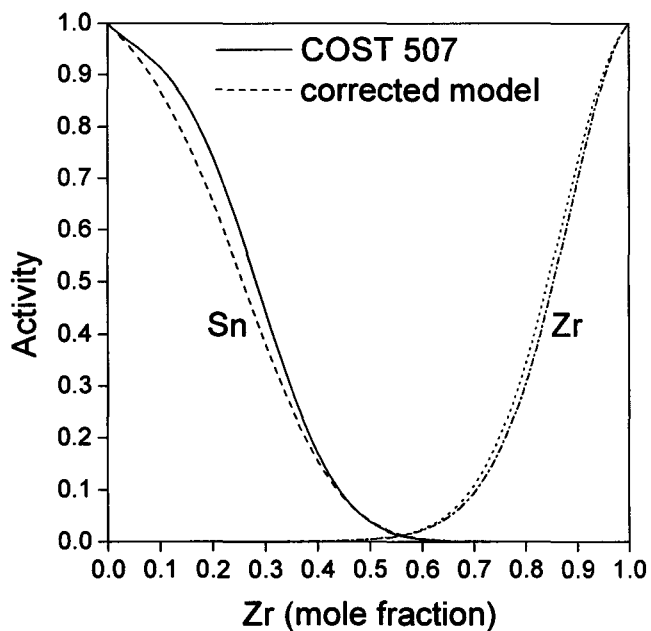


Figure 64: Activities of Sn and Zr in the liquid phase at 1750 K computed with the old and new models

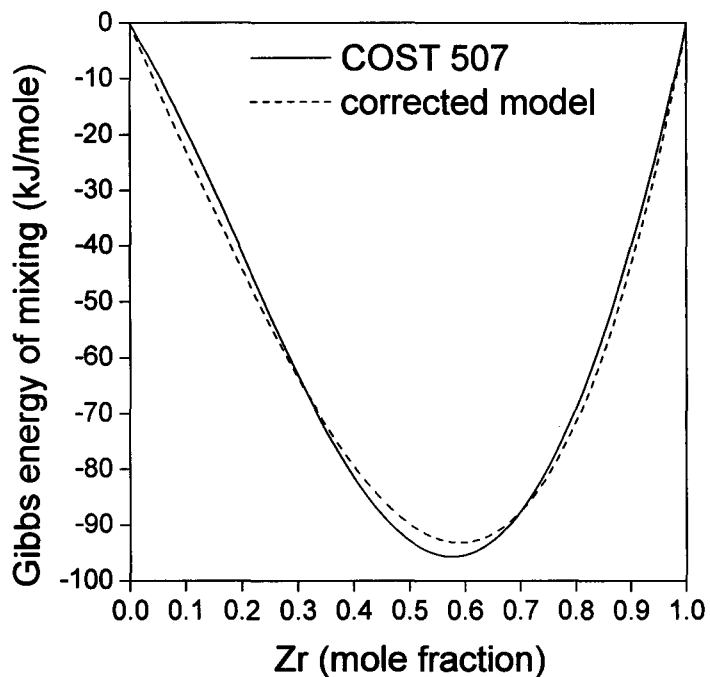


Figure 65: Molar Gibbs energies of mixing at 2750 K predicted by the old and new models

A difference between absolute values of the Gibbs energies of mixing shown in Figure 65 is not huge, but it is not a magnitude of the divergence that is important.

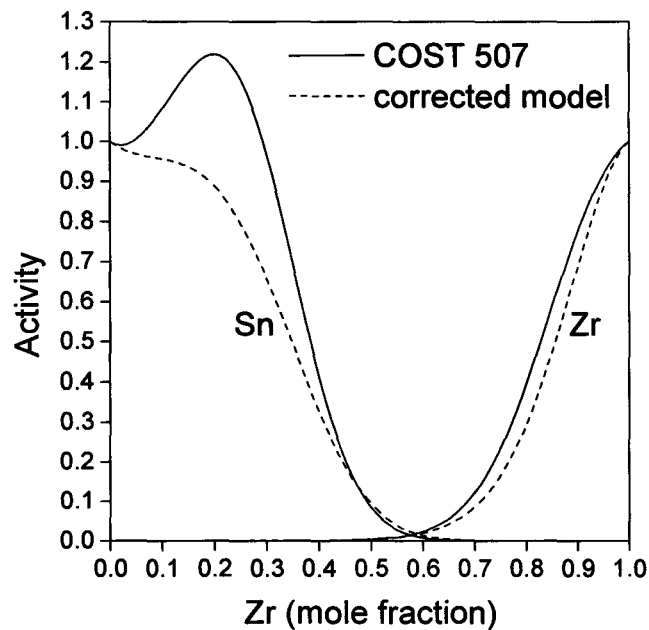


Figure 66: Activities of Sn and Zr in the liquid phase at 2750 K according to the old and new models

It is significant that the new $\Delta_{\text{mix}}G(x)$ is always convex downward while the old one is not. A beneficial effect of the topological constraints is clearly seen in Figure 66. Since $\partial a_i / \partial x_i > 0, i = \text{Sn, Zr}$, the liquid phase is internally stable.

6.5 Conclusions

Two approaches proposed in this chapter are intended for a computationally not challenging elimination of an inverted miscibility gap in the liquid phase unexpectedly discovered in a published assessment of a system. Both methods utilize the same idea. A new expression for the excess Gibbs energy of liquid was constructed in such a manner that it closely resembles the old model within a lower temperature region where no

questionable features are observed (usually it is related to the region where experimental observations used for optimization were acquired) but differs from the old formula at higher temperatures being free from the unwanted artifact.

When the first tactic is applied, the similarity between the old and new models is provided by utilizing the old formula to calculate characteristics of invariant equilibria involving the liquid phase (and, if time allows, other quantities) and then by using this information to perform a topologically constrained optimization leading to the new expression. When the second scheme is implemented, the similarity is provided by minimizing the differences between the old and new models and their partial derivatives with respect to the mole fraction within a certain $x - T$ rectangle.

In both cases, the absence of inverted miscibility gaps is guaranteed by making the Hessian of the Gibbs energy positive definite. While the first method has a fair chance to be tried by the CALPHAD community, the second method seems to be too extravagant to have a similar fate.

CHAPTER 7

Undulated phase boundaries

7.1 Introduction

Usually, an inflection point on a phase boundary is considered as an unambiguous indication that one of phases participating in the equilibrium is internally unstable, *i.e.*

that it is prone to separation.

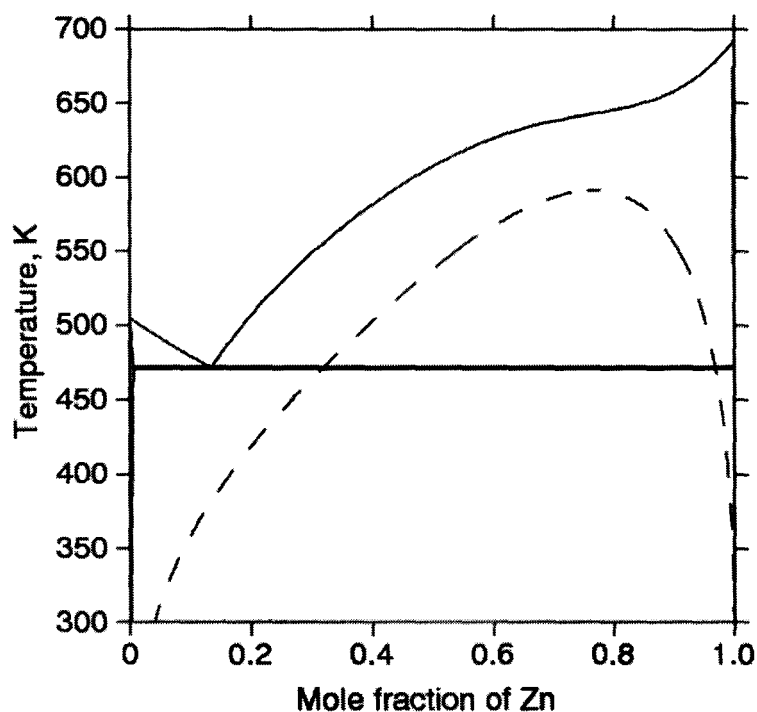


Figure 67: A metastable miscibility gap in the liquid phase (dashed curve) superimposed on the equilibrium Sn–Zn phase diagram

For example, the phase diagram resulting from thermodynamic assessment of the Sn–Zn system by Fries and Lukas [79] is shown in Figure 67 (solid lines). Let us notice

an inflection point on liquidus. A traditional way of explaining such a shape (known as an “S-shape”) is to assume that the liquid phase is prone to separation at temperatures below the liquidus. A dashed line representing a metastable miscibility gap in the liquid suggests that in this particular case, the rationalization is valid.

In this chapter, it is shown that such an explanation is not universal. This is done by deriving general expressions for the slope and curvature of a phase boundary for the case when a binary solution is in equilibrium with a stoichiometric binary phase. Then these expressions are simplified by assuming that the solution is ideal. Finally, through a straightforward mathematical analysis, a condition resulting in the appearance of an inflection point is formulated.

7.2 Calculation of slope and curvature of the phase boundary

Let us consider the equilibrium between a binary solution phase L and a binary stoichiometric phase α as shown in Figure 68.

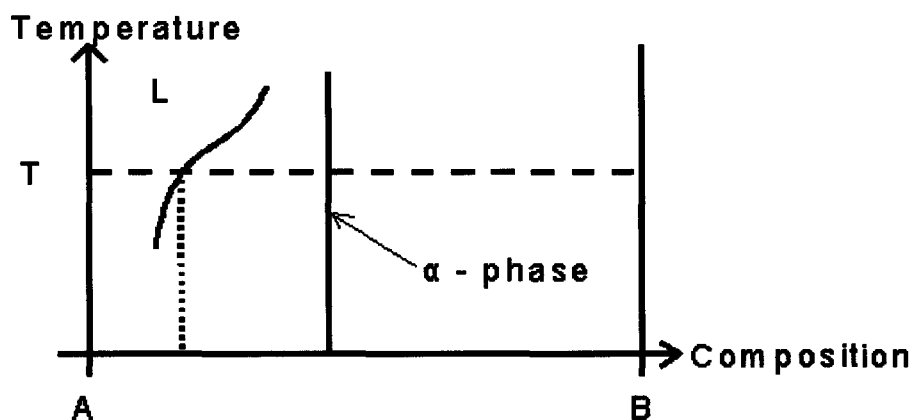


Figure 68: A schematic diagram shows the phase equilibrium boundary between a solution phase L and a stoichiometric phase α in an imaginary A-B binary system

For the sake of determinacy, let us assume that L is a simple single lattice substitutional solution. The Gibbs energies of L and α are given by (7.1) and (7.2), correspondingly:

$$G^L = (1-x^L)\Delta G_1^{0L} + x^L\Delta G_2^{0L} + RT\left((1-x^L)\ln(1-x^L) + x^L\ln x^L\right) + \Delta^{\text{ex}}G^L \quad (7.1)$$

$$G^\alpha = (1-x^\alpha)\Delta G_1^{0\alpha} + x^\alpha\Delta G_2^{0\alpha} + \Delta_f G^\alpha \quad (7.2)$$

$\Delta G_i^{0\gamma}$ is the Gibbs energy of transformation of the i -th component from the structure associated with its reference state to the structure of the γ phase. A general expression (7.2) reduces to $G^\alpha = \Delta G_1^{0\alpha}$ if $x^\alpha = 0$ and to $G^\alpha = \Delta G_2^{0\alpha}$ if $x^\alpha = 1$.

The condition of equilibrium between L and α can be written as:

$$G^L + (x^\alpha - x^L)G_L^L - G^\alpha = 0 \quad (7.3)$$

In (7.3) and below, the notation $\varphi_{\underbrace{LL\dots LL}_{m \text{ times}}\underbrace{TT\dots T}_{n \text{ times}}} \equiv \frac{\partial^{m+n}\varphi}{\partial(x^L)^m \partial T^n}$ is used for making expressions

shorter and easier to handle.

7.2.1 Slope of the phase boundary

A great deal of attention has been paid in literature to calculating slopes of phase boundaries [135, 136]. Despite of this circumstance, it seems justified to start derivations from scratch for ensuring a cohesiveness of the present work as well as for enforcing its internal logic.

Let us denote the LHS of (7.3) as F . Since F remains equal to zero along the phase boundary, one can use implicit differentiation and write:

$$F_L + F_T \frac{dT}{dx^L} = 0 \quad (7.4)$$

The expression for the slope of the phase boundary immediately follows from (7.4):

$$\frac{dT}{dx^L} = -\frac{F_L}{F_T} \quad (7.5)$$

where

$$F_L = (x^\alpha - x^L) G_{LL}^L \quad (7.6)$$

$$F_T = G_T^L + (x^\alpha - x^L) G_{LT}^L - G_T^\alpha \quad (7.7)$$

Having expressions (7.1) and (7.2), one can write partial derivatives of the Gibbs energies in (7.6) and (7.7) as:

$$G_{LL}^L = \frac{RT}{(1-x^L)x^L} + \Delta^{\text{ex}} G_{LL}^L \quad (7.8)$$

$$G_T^L = -(1-x^L) \Delta S_1^{0L} - x^L \Delta S_2^{0L} + R \left((1-x^L) \ln(1-x^L) + x^L \ln x^L \right) - \Delta^{\text{ex}} S^L \quad (7.9)$$

$$G_{LT}^L = \Delta S_1^{0L} - \Delta S_2^{0L} + R \ln \frac{x^L}{1-x^L} - \Delta^{\text{ex}} S_L^L \quad (7.10)$$

$$G_T^\alpha = -(1-x^\alpha) \Delta S_1^{0\alpha} - x^\alpha \Delta S_2^{0\alpha} - \Delta_f S^\alpha \quad (7.11)$$

Substitution of (7.8) in (7.6) gives:

$$F_L = (x^\alpha - x^L) \left(\frac{RT}{(1-x^L)x^L} + \Delta^{\text{ex}} G_{LL}^L \right) \quad (7.12)$$

Substitution of (7.9)-(7.11) in (7.7) yields:

$$F_T = R \left((1-x^\alpha) \ln(1-x^L) + x^\alpha \ln x^L \right) - (1-x^\alpha) \Delta S_1^{0\alpha \rightarrow L} - x^\alpha \Delta S_2^{0\alpha \rightarrow L} - \Delta^{\text{ex}} S^L - (x^\alpha - x^L) \Delta^{\text{ex}} S_L^L + \Delta_f S^\alpha \quad (7.13)$$

By inserting (7.12) and (7.13) in (7.5), the slope can be computed. It is worth mentioning that since there are no fundamental restrictions preventing F_T in (7.13) from being equal to zero, infinite slopes are not prohibited by thermodynamics. Slopes tending to $+\infty$ or $-\infty$ are inevitable if $T \rightarrow 0$, because all entropies of formations and transformations become infinitesimally small. It may happen that both the numerator and denominator in (7.5) are equal to zero. An analysis of this exotic situation is beyond the scope of the present work.

In a particular case when $x^\alpha = 0$ and $x^L \rightarrow 0^+$, it can easily be shown (a finiteness of $\Delta^{\text{ex}}G_{\text{LL}}^L$ should be recalled) that $\frac{dT}{dx^L} = -\frac{RT_1}{\Delta S_1^{0\alpha \rightarrow L}(T_1)} < 0$, where T_1 is the melting point of the first component when it is in the α structure. If $x^\alpha = 1$ and $x^L \rightarrow 1^-$, then $\frac{dT}{dx^L} = \frac{RT_2}{\Delta S_2^{0\alpha \rightarrow L}(T_2)} > 0$. These two expressions for limiting slopes are well known, indeed.

If $x^L \rightarrow x^\alpha$ and if $0 < x^\alpha < 1$, then F_L tends to zero. Since F_T becomes equal to entropy of melting of α taken with the opposite sign, *i.e.* since it is always negative, an indeterminacy $\frac{0}{0}$ is never encountered in (7.5). Subsequently, it can be concluded that

$$\left(\frac{dT}{dx^L} \right)_{x^L=x^\alpha} = 0.$$

7.2.2 Curvature of the phase boundary

In contrast to slopes, the calculation of curvatures of phase boundaries did not acquire much attention in the literature. An excellent work by Goodman *et al.* [137] is the

only publication available in which this problem was deeply and extensively discussed. Despite of an unquestionable relevance of that paper, the derivations below have a different mathematical and conceptual flavor, which is not surprising since the objective of this contribution differs quite significantly from that of [137].

Let us start with a terminological clarification. The curvature of the function $\psi(z)$, which is $\frac{d^2\psi/dz^2}{[1+(d\psi/dz)^2]^{3/2}}$, cannot be identified with its second derivative. In this chapter, however, for the sake of brevity, $d^2T/d(x^L)^2$ is named curvature. A justification of such a terminological frivolity is that the curvature and the second derivative either have the same sign or both are equal to zero.

Let us denote the LHS of (7.4) as Φ and recall that similar to F it remains equal to zero along the phase boundary. By using an implicit differentiation again, one obtains:

$$\Phi_L + \Phi_T \frac{dT}{dx^L} = 0 \quad (7.14)$$

where

$$\Phi_L = \frac{\partial}{\partial x^L} \left(F_L + F_T \frac{dT}{dx^L} \right) = F_{LL} + F_{LT} \frac{dT}{dx^L} + F_T \frac{d^2T}{d(x^L)^2} \quad (7.15)$$

$$\Phi_T = \frac{\partial}{\partial T} \left(F_L + F_T \frac{dT}{dx^L} \right) = F_{LT} + F_{TT} \frac{dT}{dx^L} \quad (7.16)$$

By inserting (7.15) and (7.16) in (7.14), the following expression for the second derivative can be arrived at:

$$\frac{d^2T}{d(x^L)^2} = -\frac{F_{LL} + 2F_{LT} \frac{dT}{dx^L} + F_{TT} \left(\frac{dT}{dx^L}\right)^2}{F_T} \quad (7.17)$$

By employing the definition of F and by making use of (7.1) and (7.2), the following formulae can be derived:

$$F_{LL} = -\left(\frac{RT}{(1-x^L)x^L} + \Delta^{\text{ex}}G_{LL}^L\right) + (x^\alpha - x^L) \left(\frac{RT(1-2x^L)}{((1-x^L)x^L)^2} + \Delta^{\text{ex}}G_{LLL}^L\right) \quad (7.18)$$

$$F_{LT} = (x^\alpha - x^L) \left(\frac{R}{(1-x^L)x^L} + \Delta^{\text{ex}}G_{LLT}^L\right) \quad (7.19)$$

$$F_{TT} = -(1-x^\alpha) \frac{\Delta C_{p1}^{0\alpha \rightarrow L}}{T} - x^\alpha \frac{\Delta C_{p2}^{0\alpha \rightarrow L}}{T} - \Delta^{\text{ex}}S_T^L - (x^\alpha - x^L) \Delta^{\text{ex}}S_{LT}^L + \Delta_f S_T^\alpha \quad (7.20)$$

Substitution of (7.18)-(7.20) along with F_T given by (7.13) and already calculated slope in (7.17) finalizes the computation of the curvature of the phase boundary.

7.3 Simplifications

Although one can write an explicit expression for the curvature, this formula will be monstrously long. Besides, it will not be very helpful unless $\Delta^{\text{ex}}G^L(x^L, T)$ in (7.1) and $\Delta_f G^\alpha(T)$ in (7.2) are defined. Instead of analyzing the general expression for the curvature (algebraic complexities make such an analysis virtually impossible), let us consider a trouble-free case by assuming that:

1. The solution phase is the ideal solution ($\Delta^{\text{ex}}G^L$ and its partial derivatives disappear in corresponding expressions): This assumption is made with an

intension to show that inflexion points could appear even in the case of an ideal solution;

2. $\Delta_f S^\alpha = 0$, *i.e.* $\Delta_f G^\alpha = \Delta_f H^\alpha$ (the last term in the RHS of (7.20) is equal to zero):

Since we are considering a stoichiometric solid phase in our analysis, this assumption is valid at this point;

3. ΔG_1^{0L} , ΔG_2^{0L} , $\Delta G_1^{0\alpha}$ and $\Delta G_2^{0\alpha}$ are linear functions of temperature (this entails that $\Delta C_{p1}^{0\alpha \rightarrow L}$ and $\Delta C_{p2}^{0\alpha \rightarrow L}$ in the RHS of (7.20) vanish): For the mathematical simplicity the curvature of the G VS. T is ignored. That is,

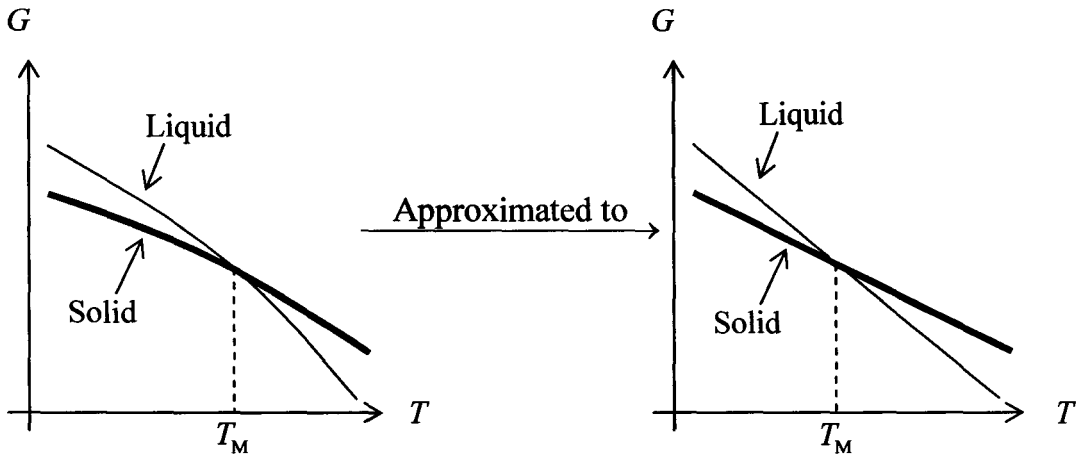


Figure 69: The relationship between Gibbs energy and temperature for stable phases

Instead of (7.12) and (7.13), one now has:

$$F_L = \frac{RT(x^\alpha - x^L)}{(1-x^L)x^L}$$

$$F_T = R\left((1-x^\alpha)\ln(1-x^L) + x^\alpha \ln x^L\right) - (1-x^\alpha)\Delta S_1^{0\alpha \rightarrow L} - x^\alpha \Delta S_2^{0\alpha \rightarrow L} \quad (7.21)$$

It is worth accentuating that the simplifications introduced make F_T always negative!

The slope is now given by:

$$\frac{dT}{dx^L} = - \frac{RT(x^\alpha - x^L)}{(1-x^L)x^L \left[R((1-x^\alpha)\ln(1-x^L) + x^\alpha \ln x^L) - (1-x^\alpha)\Delta S_1^{0\alpha \rightarrow L} - x^\alpha \Delta S_2^{0\alpha \rightarrow L} \right]} \quad (7.22)$$

The expressions (7.18)-(7.20) undergo a drastic simplification as well:

$$F_{LL} = - \frac{RT}{((1-x^L)x^L)^2} \left((x^\alpha - x^L)^2 + x^\alpha(1-x^\alpha) \right) \quad (7.23)$$

$$F_{LT} = \frac{R(x^\alpha - x^L)}{(1-x^L)x^L} \quad (7.24)$$

$$F_{TT} = 0$$

The last equality eliminates the term $F_{TT} \left(\frac{dT}{dx^L} \right)^2$ in the numerator of (7.17) thus yielding

the following much simpler expression for the curvature:

$$\frac{d^2T}{d(x^L)^2} = - \frac{F_{LL} + 2F_{LT} \frac{dT}{dx^L}}{F_T} \quad (7.25)$$

Although the formula (7.25) is valid regardless of whether the solution is in equilibrium with a pure component ($x^\alpha = 0$ or $x^\alpha = 1$) or a binary compound ($0 < x^\alpha < 1$), it is instructive to consider these cases separately.

Firstly, let us consider the situation when $x^\alpha = 0$. If $x^L \rightarrow 0^+$, then instead of (7.23), (7.24) and (7.21) one has: $F_{LL} = -RT_1$, $F_{LT} = -R$, $F_T = -\Delta S_1^{0\alpha \rightarrow L}$. Keeping in mind that $\frac{dT}{dx^L} = -\frac{RT_1}{\Delta S_1^{0\alpha \rightarrow L}}$, one arrives at the following expression:

$$\frac{d^2T}{d(x^L)^2} = -\frac{-RT_1 - 2R\left(-\frac{RT_1}{\Delta S_1^{0\alpha \rightarrow L}}\right)}{-\Delta S_1^{0\alpha \rightarrow L}} = \frac{RT_1}{\Delta S_1^{0\alpha \rightarrow L}} \left(-1 + \frac{2R}{\Delta S_1^{0\alpha \rightarrow L}}\right) \quad (7.26)$$

It is clearly seen from (7.26) that the sign of curvature in the vicinity of pure first component is determined by the magnitude of $\Delta S_1^{0\alpha \rightarrow L}(T_1)$: if entropy of fusion is less than $2R$, then the curvature is positive (the phase boundary is convex downward); if

$\Delta S_1^{0\alpha \rightarrow L}(T_1) > 2R$, then $\frac{d^2T}{d(x^L)^2} < 0$ (the phase boundary is convex upward). Will the

curvature of the phase boundary retain the sign it possesses in the vicinity of the pure first component if x^L departs from zero?

The second case when $x^\alpha = 1$ and $x^L \rightarrow 1^-$ can be analyzed in the same manner. Instead of (7.23), (7.24) and (7.21) one has: $F_{LL} = -RT_2$, $F_{LT} = R$, $F_T = -\Delta S_2^{0\alpha \rightarrow L}$. Since

the limiting slope is now equal to $\frac{RT_2}{\Delta S_2^{0\alpha \rightarrow L}(T_2)}$, the curvature is given by:

$$\frac{d^2T}{d(x^L)^2} = -\frac{-RT_2 + 2R\left(\frac{RT_2}{\Delta S_2^{0\alpha \rightarrow L}(T_2)}\right)}{-\Delta S_2^{0\alpha \rightarrow L}} = \frac{RT_2}{\Delta S_2^{0\alpha \rightarrow L}} \left(-1 + \frac{2R}{\Delta S_2^{0\alpha \rightarrow L}}\right)$$

The conclusion is exactly the same as before: if $\Delta S_2^{0\alpha \rightarrow L} < 2R$, then $\frac{d^2T}{d(x^L)^2} > 0$;

if $\Delta S_2^{0\alpha \rightarrow L}$ exceeds $2R$, the curvature is negative. The question we would like to answer is virtually identical to the previously asked: Will the curvature of the phase boundary keep the sign it has in the proximity of the pure second component when x^L goes away from unity?

Finally, if $0 < x^\alpha < 1$ and $x^L = x^\alpha$, then $\frac{dT}{dx^L} = 0$, and the curvature becomes equal

to:

$$\frac{d^2T}{d(x^L)^2} = \frac{RT}{x^\alpha(1-x^\alpha)F_T}$$

Since $F_T < 0$ (see (7.21)), $\frac{d^2T}{d(x^L)^2} < 0$. Does this inequality hold if $x^L \neq x^\alpha$? Does, in

other words, the phase boundary always remain convex upward as it is near the stoichiometric compound α ?

7.4 Analysis

For answering the question whether the curvature can change its sign or not, the numerator of (7.25) has to be analyzed. If it is always negative, the curvature will hold its sign.

Let us start with the case when $x^\alpha = 0$. The expressions (7.23), (7.21) and (7.22) are reduced to:

$$F_{LL} = -\frac{RT}{(1-x^L)^2},$$

$$F_{LT} = -\frac{R}{(1-x^L)},$$

$$\frac{dT}{dx^L} = \frac{RT}{(1-x^L) \left[R \ln(1-x^L) - \Delta S_1^{0\alpha \rightarrow L} \right]}.$$

For the numerator of (7.25) one has:

$$\begin{aligned} F_{LL} + 2F_{LT} \frac{dT}{dx^L} &= -\frac{RT}{(1-x^L)^2} - 2 \frac{R^2 T}{(1-x^L)^2 \left[R \ln(1-x^L) - \Delta S_1^{0\alpha \rightarrow L} \right]} \\ &= -\frac{RT}{(1-x^L)^2} \left(1 + \frac{2}{\ln(1-x^L) - \frac{\Delta S_1^{0\alpha \rightarrow L}}{R}} \right) \end{aligned} \quad (7.27)$$

It has been already demonstrated that if $\frac{\Delta S_1^{0\alpha \rightarrow L}}{2} > R$, $\left(\frac{d^2 T}{d(x^L)^2} \right)_{x^L \rightarrow 0^+} < 0$. Now

let us show that if $\frac{\Delta S_1^{0\alpha \rightarrow L}}{2} > R$, $1 + \frac{2}{\ln(1-x^L) - \frac{\Delta S_1^{0\alpha \rightarrow L}}{R}}$ is always positive, i.e. that the

numerator remains negative.

$$1 + \frac{2}{\ln(1-x^L) - \frac{\Delta S_1^{0\alpha \rightarrow L}}{R}} > 0 \quad (7.28)$$

$$\frac{\ln(1-x^L) - \frac{\Delta S_1^{0\alpha \rightarrow L}}{R} + 2}{\ln(1-x^L) - \frac{\Delta S_1^{0\alpha \rightarrow L}}{R}} > 0$$

$$\ln(1-x^L) - \frac{\Delta S_1^{0\alpha \rightarrow L}}{R} + 2 < 0$$

$$\ln(1-x^L) < \frac{\Delta S_1^{0\alpha \rightarrow L}}{R} - 2 \quad (7.29)$$

Since the inequality (7.29) is undoubtedly true, the inequality (7.28) is also true. It can thus be concluded that if in the vicinity of the first component the phase boundary is convex upward, its curvature always remains negative.

It has been already shown that if $\frac{\Delta S_1^{0\alpha \rightarrow L}}{2} < R$, $\left(\frac{d^2T}{d(x^L)^2} \right)_{x^L \rightarrow 0^+} > 0$. But if

$$\frac{\Delta S_1^{0\alpha \rightarrow L}}{2} < R, \text{ the term } 1 + \frac{2}{\ln(1-x^L) - \frac{\Delta S_1^{0\alpha \rightarrow L}}{R}} \text{ in (7.27) will inevitably change its sign}$$

from positive to negative, and an inflection point will appear at

$$x^L = 1 - \exp\left(\frac{\Delta S_1^{0\alpha \rightarrow L}}{R} - 2\right).$$

It can thus be concluded that if in the vicinity of the first component the phase boundary is convex downward, its curvature will inevitably change its sign when x^L is increasing.

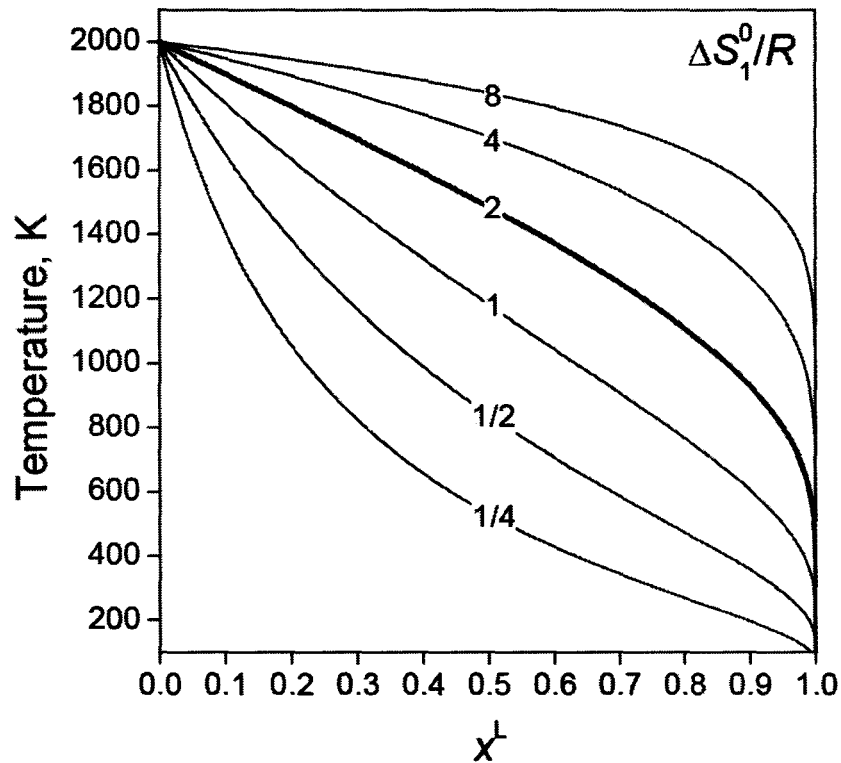


Figure 70: A family of phase boundaries corresponding to the equilibrium between the ideal solution and the pure solid first component constructed for various entropies of fusion

This is clearly demonstrated by Figure 70. It is worth repeating that whether phase

boundary is undulate or not is completely determined by the $\frac{\Delta S_1^{0\alpha \rightarrow L}}{R}$ ratio.

$$\text{If } x^\alpha = 1, F_{LL} = -\frac{RT}{(x^L)^2}, F_{LT} = \frac{R}{x^L}, \frac{dT}{dx^L} = -\frac{RT}{x^L [R \ln x^L - \Delta S_2^{0\alpha \rightarrow L}]}.$$

Subsequently, the numerator of (7.25) becomes:

$$\begin{aligned}
F_{LL} + 2F_{LT} \frac{dT}{dx^L} &= -\frac{RT}{(x^L)^2} - 2 \frac{R^2 T}{(x^L)^2 [R \ln x^L - \Delta S_2^{0\alpha \rightarrow L}]} \\
&= -\frac{RT}{(x^L)^2} \left(1 + \frac{2}{\ln x^L - \frac{\Delta S_2^{0\alpha \rightarrow L}}{R}} \right)
\end{aligned} \tag{7.30}$$

A remarkable similarity between (7.30) and (7.27) allows one to omit boring and trivial rearrangements and merely state that if in the vicinity of the first component the phase boundary is convex upward, its curvature always remains negative, but if it is convex downward, the curvature will inevitably changes its sign when x^L is decreasing. The position of the inflection point is $x^L = \exp\left(\frac{\Delta S_2^{0\alpha \rightarrow L}}{R} - 2\right)$.

Now let us write the numerator of (7.25) for the case when $0 < x^\alpha < 1$.

$$\begin{aligned}
F_{LL} + 2F_{LT} \frac{dT}{dx^L} &= -\frac{RT}{((1-x^L)x^L)^2} \left[(x^\alpha - x^L)^2 + x^\alpha(1-x^\alpha) \right. \\
&\quad \left. + \frac{R(x^\alpha - x^L)^2}{R((1-x^\alpha)\ln(1-x^L) + x^\alpha \ln x^L) - (1-x^\alpha)\Delta S_1^{0\alpha \rightarrow L} - x^\alpha \Delta S_2^{0\alpha \rightarrow L}} \right]
\end{aligned}$$

The curvature will remain negative if

$$(x^\alpha - x^L)^2 + x^\alpha(1-x^\alpha) + \frac{R(x^\alpha - x^L)^2}{R((1-x^\alpha)\ln(1-x^L) + x^\alpha \ln x^L) - (1-x^\alpha)\Delta S_1^{0\alpha \rightarrow L} - x^\alpha \Delta S_2^{0\alpha \rightarrow L}} > 0 \tag{7.31}$$

The first two summands in (7.31) are positive, but the last one is negative. Let us notice that if $x^L \rightarrow 0$ or $x^L \rightarrow 1$, the logarithmic term tends to $-\infty$, which translates into a

negative curvature. Instead of carrying out a general algebraic analysis of the inequality (7.31), let us visualize its LHS for various x^α , $\Delta S_1^{0\alpha \rightarrow L}$ and $\Delta S_2^{0\alpha \rightarrow L}$.

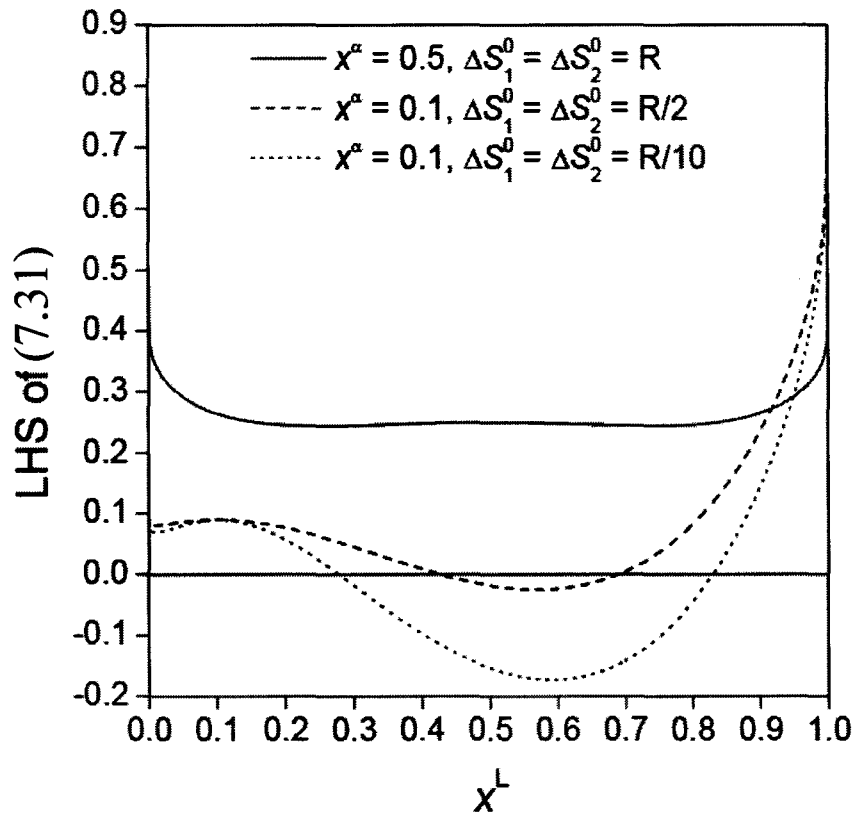


Figure 71: An example of concentration dependencies of the LHS of (7.31) for different entropies of fusion and compositions of the stoichiometric phase

Figure 71 clearly demonstrates that small entropies of fusion favor the undulation. It also is clear that since the term $x^\alpha (1 - x^\alpha)$ in (7.31) is maximized by $x^\alpha = 0.5$, the undulation is favored by a composition departing from the equimolar ratio.

Although Figure 71 is convincing, it might be instructive to actually construct a phase diagram with a wavy boundary. For the sake of determinacy, let us accept that:

1. The reference states are pure components having the structure of L phase, *i.e.*

ΔG_1^{0L} and ΔG_2^{0L} used in (7.1) are both equal to zero;

2. Lattice stabilities $\Delta G_1^{0\alpha}$ and $\Delta G_2^{0\alpha}$ employed in (7.2) are described by the same

linear function of temperature: $\Delta G_1^{0\alpha} = \Delta G_2^{0\alpha} = -1000 + 0.831451T$ J/mol;

3. The Gibbs energy of formation of the α phase is $\Delta_f G^\alpha = -5000$ J/mol.

The phase diagram resulting from these thermodynamic quantities is shown in Figure 72. It is not surprising that the inflection points are seen at the right boundary for which $(x^\alpha - x^L)^2$ in (7.31) undergoes a much greater variation in comparison with the left boundary.

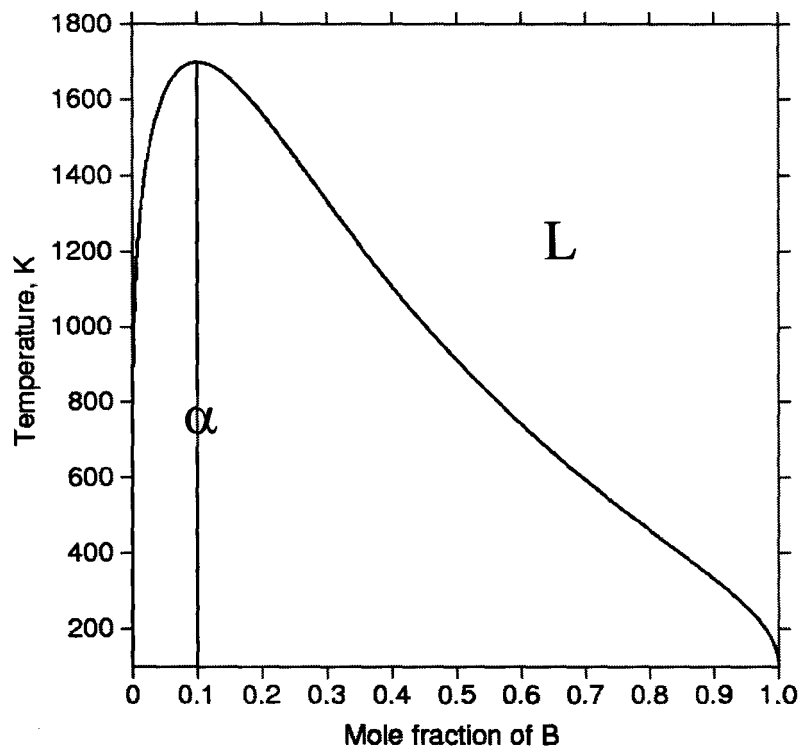


Figure 72: A phase diagram unambiguously demonstrating the presence of inflection points at the phase boundary for the case when the ideal solution is in equilibrium with a stoichiometric phase

7.5 Conclusion

It is not uncommon to see inflection points at phase boundaries. Usually, their existence is attributed to an internal instability of one of the phases coexisting along the boundary. It has been shown that this explanation is not universal. It has been proven that if a binary ideal solution is in equilibrium with a pure component, an inflection point at a corresponding phase boundary inevitably appears if the entropy of fusion is less than $2R$. If the solution is in equilibrium with a stoichiometric phase, inflection points are favored by small entropies of fusion as well as by a composition of the stoichiometric phase deviating from the equimolar ratio.

CHAPTER 8

Topological constraints in eliminating suspicious inflexion points on phase boundaries

8.1 Introduction

There are two thermodynamic reasons presented in CHAPTER 7 for the real existence of inflexion points on phase boundaries. They are,

- (i) when one of the phases participating in the equilibrium is internally unstable.
- (ii) when the entropy of fusion of component(s) have values less than $2R$ (a new finding presented in this thesis).

If existence of an inflexion point on a phase boundary of a calculated phase diagram cannot be justified by one of the above-mentioned reasons, then such an inflexion point should be considered as artifact, which resulted from an incorrect phase model of a phase participating in the equilibrium. Many examples for this type of artifact have already been shown in section 3.2.1.(b)

Generally non-real inflection points are observed on phase boundaries when the phases participating in the equilibrium are modeled with excess Gibbs energy terms. In many cases, modeling a system without excess Gibbs energy is unavoidable. Keeping this situation in mind, this chapter proposes topologically constrained thermodynamic optimization to avoid calculating phase boundaries with non real inflexion points.

8.2 Aim

Applicability of topological constraints in eliminating suspicious inflexion points on phase boundaries could be exemplified through re-optimization of any system shown in section 3.2.1.(b). However, such re-optimization is not covered in this chapter and the reason for not performing a real-reoptimization is explained below.

For instance let us consider a liquidus of a system with a suspicious inflexion point on it. In this case to eliminate the inflexion point, one might use either constraint

either $\frac{d^2T^{\text{liquidus}}}{d(x^L)^2} > 0$ or $\frac{d^2T^{\text{liquidus}}}{d(x^L)^2} < 0$ within a certain composition range. The current

Thermo-Calc version-R does not have the necessary tools to implement these constraints during thermodynamic optimizations. Hence, to implement the above-mentioned topological constraints in thermodynamic optimization, we have to develop our own Fortran program to calculate the second derivative of temperature with respect to composition.

Developing a general program to calculate the $\frac{d^2T^{\alpha/\beta}}{d(x^{\text{phase}})^2}$ *, which can be used for

any thermodynamic system is not focused in this thesis due to thermodynamic and programming complexities. Hence, we decided to develop a relatively simple program for a simple imaginary system with just two solutions such as liquid and solid. From this point we aimed two tasks to be accomplished. They are:

* α/β refers the phase boundary between the phases α and β , x^{phase} could be x^α or x^β

- (i) Generating a binary phase diagram for an imaginary isomorphous system (complete solubility of the two components in the liquid and solid phases) A-B with undulated liquidus and solidus. It is fair to argue that the generated phase diagram will have artifacts similar to the ones observed in the figures in section 3.2.1.(b).
- (ii) Optimizing the A-B system under topological constraints to eliminate the inflexion points on both liquidus and solidus. This task is equivalent to the elimination of suspicious inflexion points from a real system by re-optimization under topological constraints.

8.3 An imaginary A-B binary system with undulated liquidus and solidus

8.3.1 Generating the A-B phase diagram

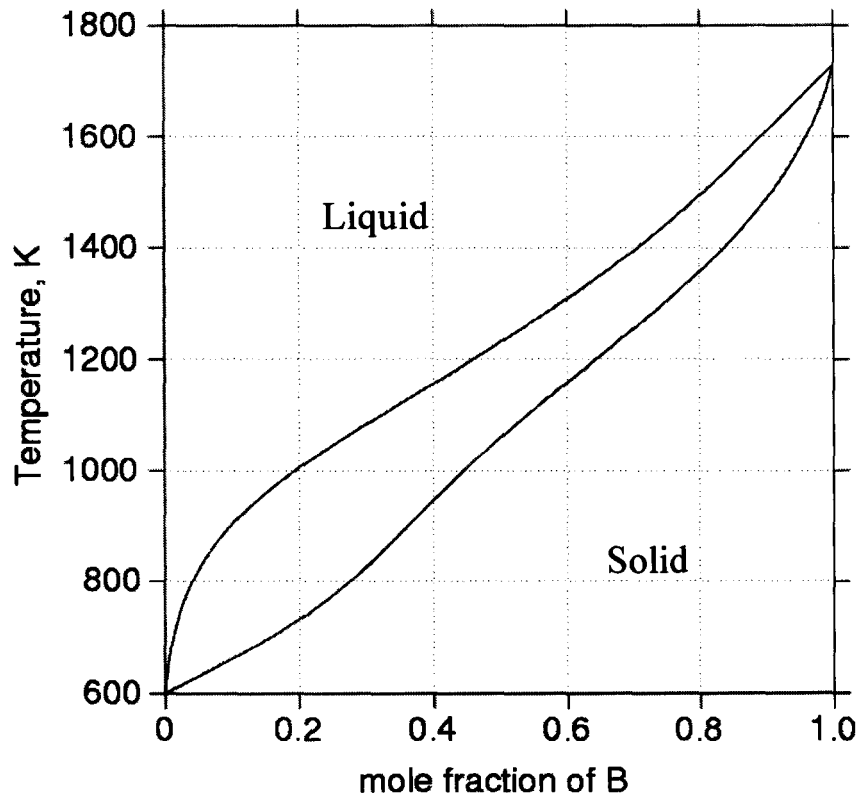


Figure 73: An imaginary A-B phase diagram

Figure 73 shows the imaginary A-B binary phase diagram with undulated liquidus and solidus. The excess Gibbs energies used to generate phase boundaries with inflexion points are,

$$\Delta_{\text{ex}} G(x^L, T) = x^L (1 - x^L) (18000 - 0.5T - 0.0185T^2) \quad (8.1)$$

$$\Delta_{\text{ex}} G(x^S, T) = x^S (1 - x^S) (10000 + 2.802T - 0.0135T^2) \quad (8.2)$$

for the liquid and solid phases respectively. To illustrate the way to reach the excess Gibbs energy descriptions in (8.1) and (8.2), let us consider the following Gibbs energies

$$G^L = (1 - x^L) \Delta_{\text{tr}} G(T)_A^{0\text{RS(A)} \rightarrow \text{L}} + x^L \Delta_{\text{tr}} G(T)_B^{0\text{RS(B)} \rightarrow \text{L}} + RT \left[(1 - x^L) \ln(1 - x^L) + x^L \ln x^L \right] + \Delta_{\text{ex}} G(x^L, T) \quad (8.3)$$

$$G^S = (1 - x^S) \Delta_{\text{tr}} G(T)_A^{0\text{RS(A)} \rightarrow \text{S}} + x^S \Delta_{\text{tr}} G(T)_B^{0\text{RS(B)} \rightarrow \text{S}} + RT \left[(1 - x^S) \ln(1 - x^S) + x^S \ln x^S \right] + \Delta_{\text{ex}} G(x^S, T) \quad (8.4)$$

for the liquid and solid phases respectively. In the above equations (8.1) and (8.2), RS(A) and RS(B) refers the reference states of components A and B respectively.

When calculating phase diagrams, the phase boundaries are detected via constructing common tangents to the G Vs x curves of phases that exist in the system at different temperatures.

Since the first derivative of the Gibbs energy with respect to the composition participates in finding the phase boundaries, let us take the first derivative of (8.3) and (8.4) with respect to composition.

$$\frac{\partial G^L}{\partial x^L} = -\Delta_{\text{tr}} G_A^{0\text{RS(A)} \rightarrow \text{L}} + \Delta_{\text{tr}} G_B^{0\text{RS(B)} \rightarrow \text{L}} + \frac{\partial [\Delta_{\text{ex}} G(x^L, T)]}{\partial x^L} \quad (8.5)$$

$$\frac{\partial G^S}{\partial x^S} = -\Delta_{tr} G_A^{0RS(A) \rightarrow S} + \Delta_{tr} G_B^{0RS(B) \rightarrow S} + \frac{\partial [\Delta_{ex} G(x^S, T)]}{\partial x^S} \quad (8.6)$$

Generally by choosing the proper reference state for the constituent components the contribution of Gibbs energy of transformation to the derivative $\partial G^{\text{phase}} / \partial x^{\text{phase}}$ can be minimized. Hence, we can conclude that $\partial G^{\text{phase}} / \partial x^{\text{phase}}$ is mainly determined by the contribution from the $\partial(\Delta_{ex} G^{\text{phase}}) / \partial x^{\text{phase}}$. From this point we can deduce that the erratic behavior of $\Delta_{ex} G^{\text{phase}}$ with temperature might lead to undulations in phase boundaries.

Moreover the enthalpic and excess entropic contribution to the excess Gibbs energy are related through,

$$\Delta_{ex} G^{\text{phase}} = \Delta_{ex} H^{\text{phase}} - T \Delta_{ex} S^{\text{phase}} \quad (8.7)$$

In (8.7) generally $\Delta_{ex} H^{\text{phase}}$ is independent of temperature. Now if we think of an expression for the $\Delta_{ex} S^{\text{phase}}$ with some unrealistic temperature dependence such as an expression with T^n terms then $\Delta_{ex} G^{\text{phase}}$ will be unpredictable with temperature. From this analysis we decided to use the expression for the $\Delta_{ex} G^{\text{phase}}$ as,

$$\Delta_{ex} G^{\text{phase}} = x^{\text{phase}} (1 - x^{\text{phase}}) (a + bT + cT^2) \quad (8.8)$$

The parameters a, b , and c in (8.8) for the liquid and solid phases of the A-B system in Figure 73 were obtained through several trials.

The liquidus and the solidus in Figure 73 shows two inflexion points on each boundary. In order to make the liquidus convex upward and to make the solidus convex downwards the constraints to be used are,

$$\frac{d^2 T^{\text{liquidus}}}{d(x^L)^2} < 0 \quad (8.9)$$

$$\frac{d^2 T^{\text{solidus}}}{d(x^S)^2} > 0 \quad (8.10)$$

Now let us see the intermediate steps involved in imposing the constraints (8.9) and (8.10) during the thermodynamic optimization.

8.3.2 Calculation of slopes and curvatures

The very first conditions to be considered in calculating the slopes and curvatures of equilibrium phase boundaries of the system shown in Figure 73 are,

$$F_1(x^L, x^S, T) = \mu_A^L - \mu_A^S = G^L - x^L \frac{\partial G^L}{\partial x^L} - G^S + x^S \frac{\partial G^S}{\partial x^S} = 0 \quad (8.11)$$

$$F_2(x^L, x^S, T) = \mu_B^L - \mu_B^S = G^L + (1 - x^L) \frac{\partial G^L}{\partial x^L} - G^S - (1 - x^S) \frac{\partial G^S}{\partial x^S} = 0 \quad (8.12)$$

The A-B binary system the above conditions (8.11) and (8.12) are satisfied along the liquidus and solidus. Now we can write the following equations similar to the one in (7.4) by taking x^S as a function of x^L and T as a function of x^L .

$$\frac{\partial F_1}{\partial x^L} + \frac{\partial F_1}{\partial x^S} \frac{dx^S}{dx^L} + \frac{\partial F_1}{\partial T} \frac{dT}{dx^L} = 0 \quad (8.13)$$

$$\frac{\partial F_2}{\partial x^L} + \frac{\partial F_2}{\partial x^S} \frac{dx^S}{dx^L} + \frac{\partial F_2}{\partial T} \frac{dT}{dx^L} = 0 \quad (8.14)$$

For selected descriptions of G^L and G^S the unknowns $\frac{dx^S}{dx^L}$ and $\frac{dT}{dx^L}$ can be calculated by solving equations (8.13) and (8.14). Now the similarities of (8.13) and (8.14), allows one to write the following equation.

$$\frac{\partial F_i}{\partial x^L} + \frac{\partial F_i}{\partial x^S} \frac{dx^S}{dx^L} + \frac{\partial F_i}{\partial T} \frac{dT}{dx^L} = 0, i=1,2 \quad (8.15)$$

Similar to (7.14) the following two equations can be written by taking LHS of (8.13) and (8.14) as Φ_1 and Φ_2 respectively.

$$\frac{\partial \Phi_1}{\partial x^L} + \frac{\partial \Phi_1}{\partial x^S} \frac{dx^S}{dx^L} + \frac{\partial \Phi_1}{\partial T} \frac{dT}{dx^L} = 0 \quad (8.16)$$

$$\frac{\partial \Phi_2}{\partial x^L} + \frac{\partial \Phi_2}{\partial x^S} \frac{dx^S}{dx^L} + \frac{\partial \Phi_2}{\partial T} \frac{dT}{dx^L} = 0 \quad (8.17)$$

Here again the similarities of (8.16) and (8.17) allows one to write the following equation.

$$\frac{\partial \Phi_i}{\partial x^L} + \frac{\partial \Phi_i}{\partial x^S} \frac{dx^S}{dx^L} + \frac{\partial \Phi_i}{\partial T} \frac{dT}{dx^L} = 0, i=1,2 \quad (8.18)$$

and

$$\Phi_i = \frac{\partial F_i}{\partial x^L} + \frac{\partial F_i}{\partial x^S} \frac{dx^S}{dx^L} + \frac{\partial F_i}{\partial T} \frac{dT}{dx^L} = 0, i=1,2 \quad (8.19)$$

Now when substituting (8.19) in (8.18) we get

$$\begin{aligned}
& \frac{\partial}{\partial x^L} \left(\frac{\partial F_i}{\partial x^L} + \frac{\partial F_i}{\partial x^S} \frac{dx^S}{dx^L} + \frac{\partial F_i}{\partial T} \frac{dT}{dx^L} \right) \\
& + \frac{\partial}{\partial x^S} \left(\frac{\partial F_i}{\partial x^L} + \frac{\partial F_i}{\partial x^S} \frac{dx^S}{dx^L} + \frac{\partial F_i}{\partial T} \frac{dT}{dx^L} \right) \frac{dx^S}{dx^L} \\
& + \frac{\partial}{\partial T} \left(\frac{\partial F_i}{\partial x^L} + \frac{\partial F_i}{\partial x^S} \frac{dx^S}{dx^L} + \frac{\partial F_i}{\partial T} \frac{dT}{dx^L} \right) \frac{dT}{dx^L} = 0, i = 1, 2
\end{aligned} \tag{8.20}$$

The differentiations in (8.20) give the following equation

$$\begin{aligned}
& \frac{\partial F_i}{\partial x^S} \frac{d^2 x^S}{d(x^L)^2} + \frac{\partial F_i}{\partial T} \frac{d^2 T}{d(x^L)^2} + \frac{\partial^2 F_i}{\partial (x^L)^2} + 2 \frac{dT}{dx^L} \frac{\partial^2 F_i}{\partial x^L \partial T} \\
& + \left(\frac{dx^S}{dx^L} \right)^2 \frac{\partial^2 F_i}{\partial (x^S)^2} + 2 \frac{dx^S}{dx^L} \frac{dT}{dx^L} \frac{\partial^2 F_i}{\partial x^S \partial T} + \left(\frac{dT}{dx^L} \right)^2 \frac{\partial^2 F_i}{\partial T^2} = 0, i = 1, 2
\end{aligned} \tag{8.21}$$

From (8.21) we can calculate the curvature of the liquidus $\frac{d^2 T}{d(x^L)^2}$ and the second order

derivative $\frac{d^2 x^S}{d(x^L)^2}$. Moreover from (8.21) one can deduce that the curvature of the

liquidus is non-linear with respect to the coefficients associated with the excess Gibbs energy terms.

In the case of solidus, slope and curvature can be calculated using similar equations of (8.13)-(8.21) by taking x^L as a function of x^S and T as a function of x^S .

8.3.3 Derivatives to calculate dx^S/dx^L , dT/dx^L , $d^2 x^S/d(x^L)^2$ and $d^2 T/d(x^L)^2$

All the necessary derivatives to calculate slope and curvature of phase boundaries are given in APPENDIX II.

From APPENDIX II we can find that to calculate slopes and curvatures of phase

boundaries the following eight derivatives such as $\frac{\partial G}{\partial x}$, $\frac{\partial G}{\partial T}$, $\frac{\partial^2 G}{\partial x^2}$, $\frac{\partial^2 G}{\partial x \partial T}$, $\frac{\partial^2 G}{\partial T^2}$, $\frac{\partial^3 G}{\partial x^3}$,

$\frac{\partial^3 G}{\partial x^2 \partial T}$, and $\frac{\partial^3 G}{\partial x \partial T^2}$ are necessary for the Gibbs energies of all phases that exist in the

system.

8.4 Thermodynamic optimization of the A-B system under topological constraints

To exemplify the application of topological constraints in eliminating suspicious inflexion points from phase boundaries, a topologically constrained thermodynamic optimization is performed on the imaginary A-B system described in the section 8.3. This thermodynamic optimization is performed using a “home grown” optimizer, which is capable of calculating the derivative d^2T/dx^2 . The necessity to use the “home grown” optimizer has already explained in the section 8.2.

8.4.1 Model selection

The topologically constrained thermodynamic optimization was performed twice on the A-B system. The first optimization used a regular solution model named “New but similar” for both the liquid and solid phases. The excess Gibbs energies of both of these phases were modeled using the following excess Gibbs energy equations:

$$\Delta_{ex}G(x^L, T) = x^L (1 - x^L) (C_1^L + C_2^L T + C_3^L T^2) \quad (8.22)$$

$$\Delta_{ex}G(x^S, T) = x^S (1 - x^S) (C_1^S + C_2^S T + C_3^S T^2) \quad (8.23)$$

The temperature dependencies in (8.22) and (8.23) are similar to the ones in (8.1) and (8.2).

The second optimization used a sub-regular solution model named “New” for both the liquid and solid phases. The excess Gibbs energies of both of these phases were modeled using the following excess Gibbs energy equations:

$$\Delta_{ex}G(x^L, T) = x^L (1 - x^L) \left[(C_1^L + C_2^L T + C_3^L T^2) + (C_4^L + C_5^L T)(1 - 2x^L) \right] \quad (8.24)$$

$$\Delta_{ex}G(x^S, T) = x^S (1 - x^S) \left[(C_1^S + C_2^S T + C_3^S T^2) + (C_4^S + C_5^S T)(1 - 2x^S) \right] \quad (8.25)$$

8.4.2 Optimization

Unlike other thermodynamic optimizations presented in the CHAPTER 5 and CHAPTER 6, the thermodynamic optimization on the A-B system was performed using own thermodynamic optimizer developed for the following non-linear least squares problem under non-linear constraints:

$$\begin{aligned} & \sum_i \omega_i \left(P_i^L - \hat{P}_i^L(\bar{C}^L) \right)^2 + \sum_i \omega_i \left(P_i^S - \hat{P}_i^S(\bar{C}^S) \right)^2 \\ & + \sum_i \omega_i \left(T_i^{\text{liquidus}} - \hat{T}_i^{\text{liquidus}}(\bar{C}^L, \bar{C}^S) \right)^2 \\ & + \sum_i \omega_i \left(T_i^{\text{solidus}} - \hat{T}_i^{\text{solidus}}(\bar{C}^L, \bar{C}^S) \right)^2 \rightarrow \min(\bar{C}^L, \bar{C}^S) \end{aligned} \quad (8.26)$$

$$\text{Subject to } \frac{d^2 T^{\text{liquidus}}}{d(x^L)^2} \leq 0, \forall x^L \in (0,1)$$

$$\frac{d^2 T^{\text{solidus}}}{d(x^S)^2} \geq 0, \forall x^S \in (0,1)$$

where P_i and \hat{P}_i are the experimental and calculated properties respectively.

In building a Fortran program for the optimization problem in (8.26) we utilized the subroutine NCONF [138] with other necessary subroutines and functions. The subroutine NCONF is written for solving, constrained non-linear programming problems. The total programming package contains 1601 lines of Fortran 90 codes in one main program, 4 modules, 12 functions, 21 subroutines, and a “grey box”. We used this “home grown” optimizer in eliminating the inflexion points on the liquidus and solidus of the A-B system illustrated in the Figure 73 through the Thermo-Calc user interface called the TQ interface.

8.4.3 Results

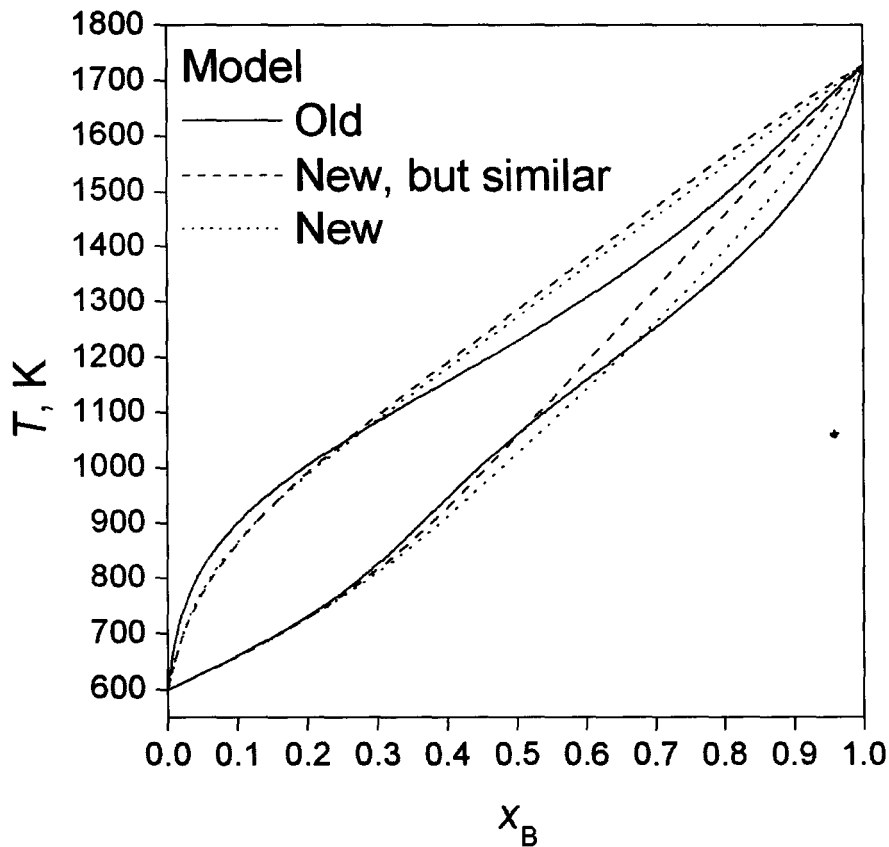


Figure 74: A comparison of different models in the calculation of the A-B imaginary binary phase diagram

It can be seen from Figure 74 that the topologically constrained thermodynamic optimization successfully eliminated the inflection points from the phase boundaries. Moreover it can be seen that the “New” model with five coefficients calculates phase boundaries closer to the original one than does the “New, but similar” model with three coefficients. The similar difference is observed in the calculated properties illustrated in Figure 75-Figure 78 as well.

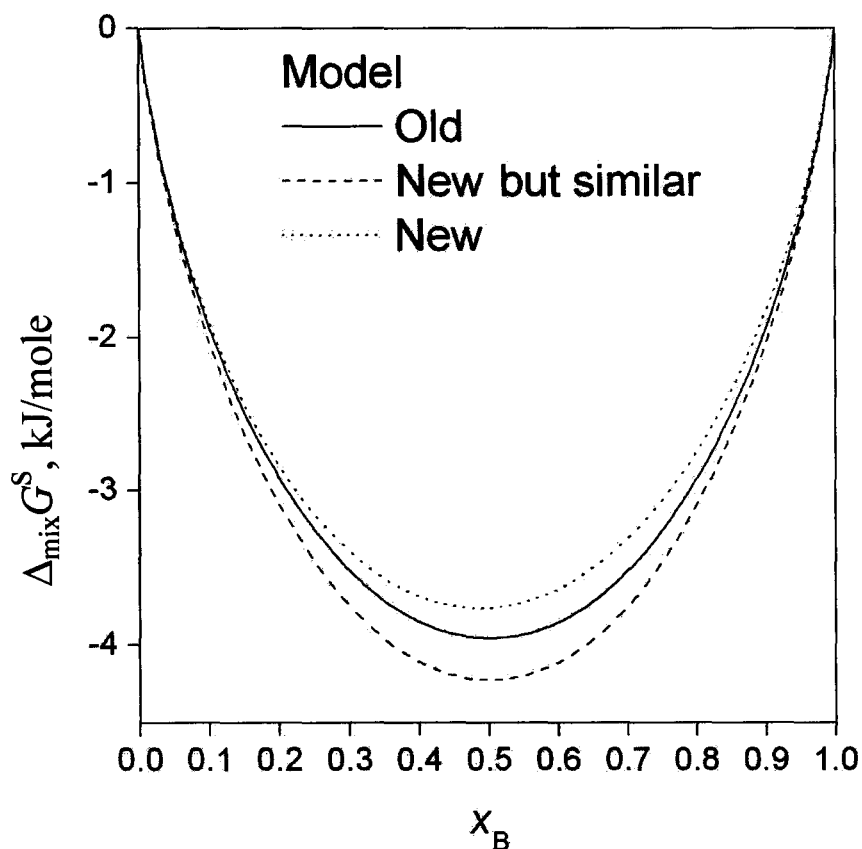


Figure 75: A comparison of different models in the calculation of $\Delta_{\text{mix}}G^S$ in A-B binary system at 823.15 K

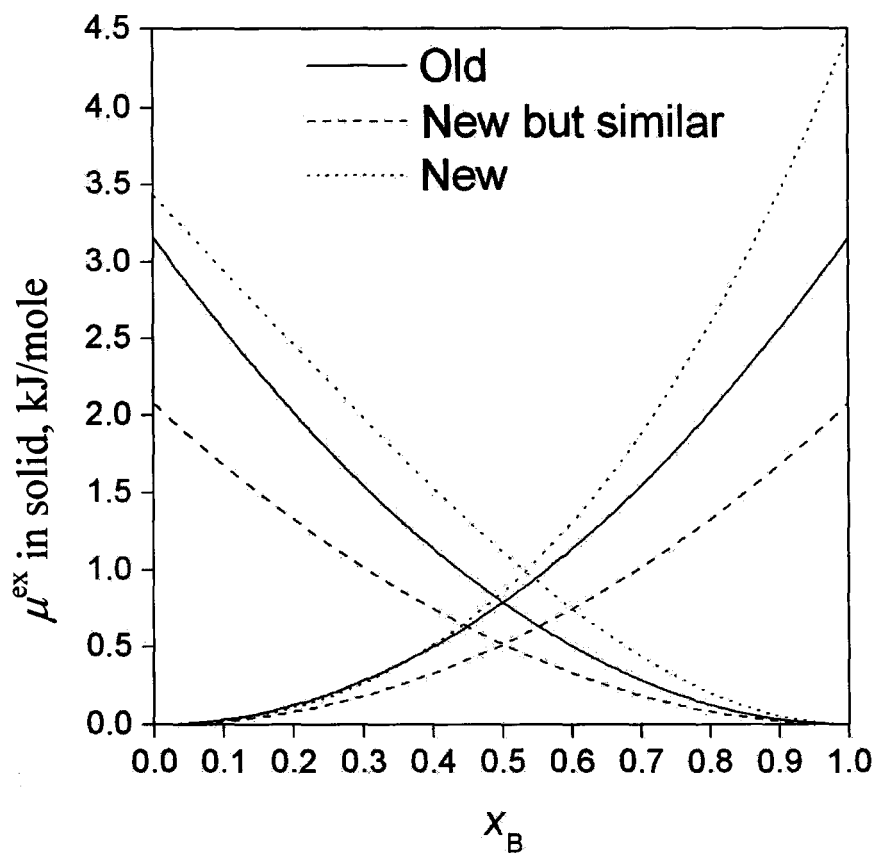


Figure 76: A comparison of different models in the calculation of μ^{ex} solid in A-B binary system at 823.15 K

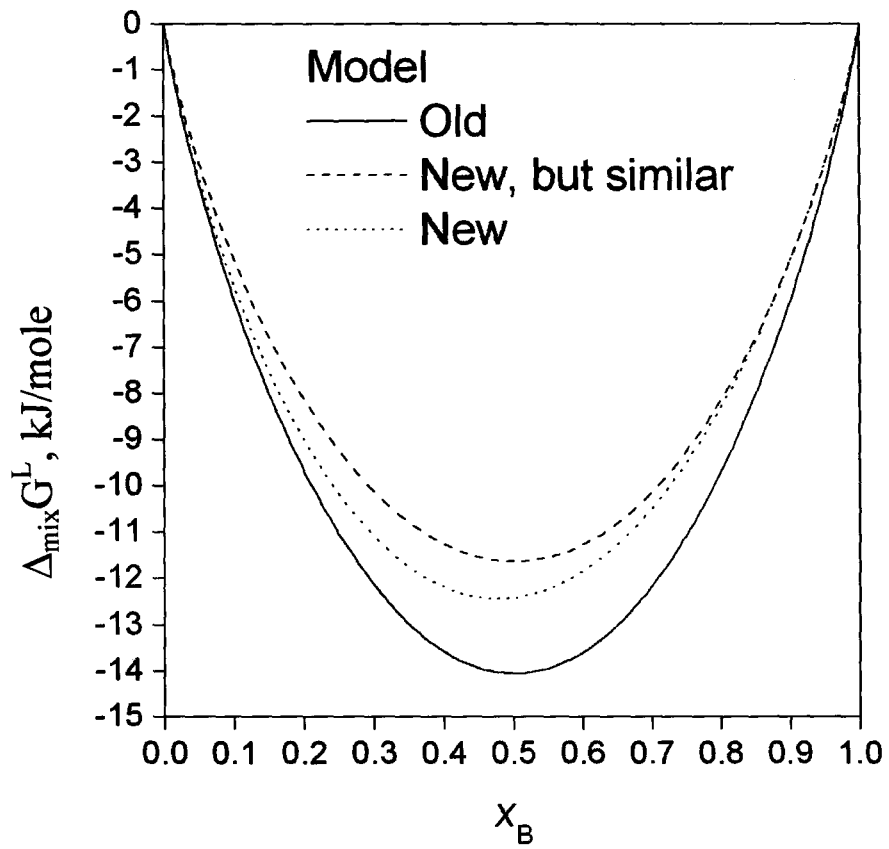


Figure 77: A comparison of different models in the calculation of $\Delta_{\text{mix}}G^L$ in A-B binary system at 1473.15 K

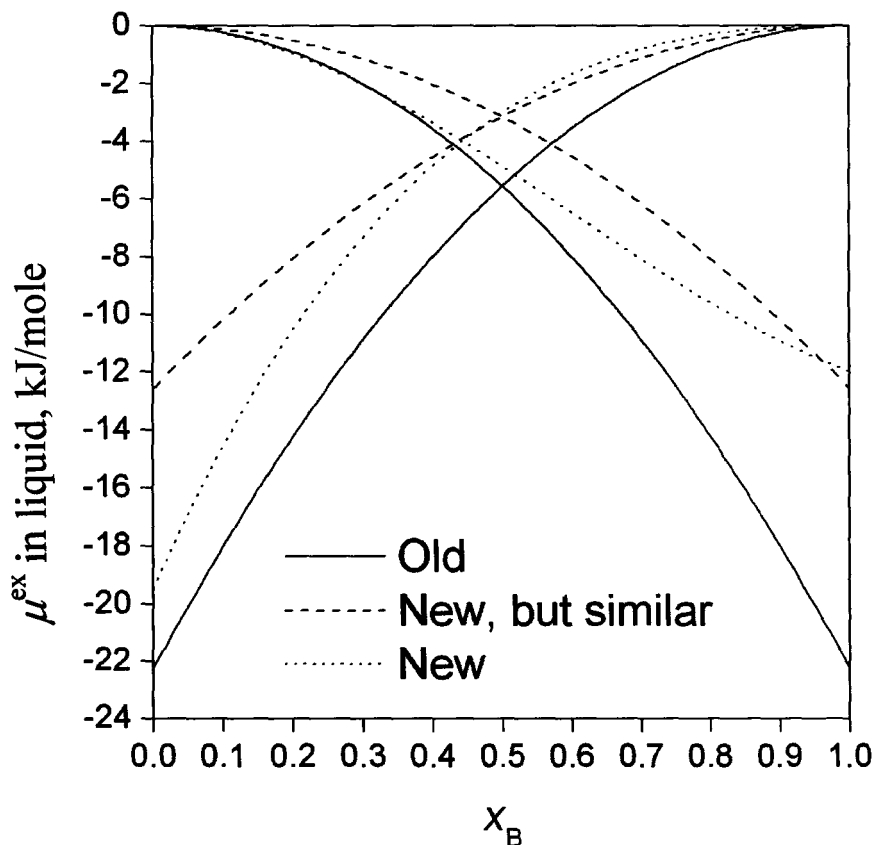


Figure 78: A comparison of different models in the calculation of μ^{ex} liquid in A-B binary system at 1473.15 K

8.5 Conclusions

- The present day version of Thermo-Calc is incapable of calculating second derivatives.
- Additional Fortran programming is necessary to perform a topologically constrained thermodynamic optimization in eliminating suspicious inflexion points from phase boundaries.
- Topological constraints in thermodynamic optimization are successful in eliminating phase boundary undulations.

CHAPTER 9

Concluding remarks and future directions

9.1 Concluding remarks

A new approach in thermodynamic optimization has been proposed in this thesis. In the new approach unlike traditional CALPHAD techniques (which is an unconstrained, non-linear least squares optimization technique), topological constraints have been imposed during thermodynamic optimization.

It has been shown that the topologically constrained thermodynamic optimization successfully eliminates the artifacts that resulted from traditional CALPHAD technique in the Mg-Sb (non real inverted miscibility gap at high temperatures), Sn-Zr (non real inverted miscibility gap at high temperatures), and A-B imaginary (wavy phase boundary) systems.

Moreover it has been shown that topological constraints in thermodynamic optimization could also be used for a simple refining of phase models. An exemplification of phase model refinement has been demonstrated in the Sn-Zr system.

Further it is shown that a suspicious feature is not necessarily an artifact. Instead, it might be an inherent feature of the system. A novel "2R rule" has been derived to show that the existence of wavy phase boundary in the equilibrium between an ideal liquid solution and a stoichiometric solid α .

Finally the algorithmic details have been formulated for a multi-component thermodynamic optimization under topological constraints.

9.2 Future directions

One of the extensions of this thesis work could be employing investigated and quantified topological properties of thermodynamic functions and phase boundaries for optimizing sophisticated multi-component systems. One of the system that could be investigated is the Zn-Fe-Al system in which an actually non-existing inverted miscibility gap in the liquid phase at high temperatures is predicted by the model of the liquid phase proposed by Nakano, Malakhov, Yamaguchi and Purdy [140]. Moreover, a topologically suspicious continuation of the calculated LIQUID/LIQUID+BCC phase boundary is seen in this system.

Another future extension of the research presented in this thesis could be the re-optimization of the Se-As system under topological constraints to eliminate the phase boundary undulations illustrated in Figure 19.

Further it will be interesting to investigate why while some models/formalisms are prone to produce artifacts, others are free of such a shortcoming. In other words, can it be said a priori that a usage of a particular model/formalism will likely be associated with unwanted features? Can corresponding criteria be formulated? For instance the following two cases could be analyzed in this regard:

- (i) Redlich-Kister [1] Vs partially ionic liquid [141]
- (ii) Cell model [142] Vs modified quasi-chemical formalism [143-145]

BIBLIOGRAPHY

1. Agren, J. "Calculation of phase diagrams: Calphad" *Current opinion in solid state and materials science* 1996, Vol.1, No.3, P.355-360
2. Y. A. Chang "Phase diagram calculations in teaching, research, and industry" *Metallurgical and materials transactions A: Physical metallurgy and materials science* 2006, Vol.37, No.2, P.273-305
3. M.G. Fahrman, G.D. Smith "Capitalizing on computational tools in industrial alloy development" *Journal of the minerals, metals and materials society* 2002, Vol.54, No.1, P.42-44
4. D.V. Malakhov "Thermodynamic assessment of the Bi-Zn system" *Calphad* 2000, Vol.24, No.1, P.1-147
5. D.V. Malakhov, X.J. Liu, I. Ohnuma, K. Ishida "Thermodynamic Calculation of Phase Equilibria of the Bi-Sn-Zn System" *Journal of phase equilibria* 2000, Vol.21, No.6, P.514-520
6. G.R. Purdy, D.V. Malakhov, A. Guha "Homogenization of multicomponent alloys via partial melting" *Journal of phase equilibria* 2001, Vol.22, No.4, P.439-450
7. G. Reumont, M. Mathon, R. Fourmentin, P. Perrot "The Fe-Cr-Zn system in relation with the galvanizing process in chromium-added zinc bath" *Zeitschrift fuer metallkunde/Materials research and advanced techniques* 2003, Vol.94, No.4, P.411-418

8. D.V. Malakhov “Confidence intervals of calculated phase boundaries” *Calphad* 1997, Vol.21, No.3, P.391-400
9. R. Zhang, Z. He, W. Jie “Prediction of solid-liquid interface stability and dendritic growth in multi-component alloys with calphad method” *The fifth pacific rim international conference on advanced materials and processing 2005*, Vol.475-479, No.4, P.2721-2724
10. Van Laar JJ. *Z Phys Chem* 1908;63:216
11. Van Laar JJ. *Z Phys Chem* 1908;64:257
12. J.L. Meijering “Segregation in regular ternary solutions, Part I” *Philips research reports 5* 1950, P.333-356
13. J.L. Meijering “Segregation in regular ternary solutions, Part II” *Philips research reports 6* 1951, P.183-210
14. J.L. Meijering and H.K. Hardy “Closed miscibility in ternary and quaternary regular alloy solutions” *Acta metallurgica* 1956, Vol.4, P.249-256
15. J.L. Meijering “Calculation of the nickel-chromium-copper phase diagram from binary data” *Acta metallurgica* 1957, Vol.5, P.257-264
16. J.L. Meijering Thermodynamical calculation of phase diagrams. In: Physical chemistry of metallic solutions and intermetallic compounds 1960, Chemical publishing company, Inc. (New York), P124–142
17. O. Kubaschewski and C.B. Alcock Metallurgical thermodynamic chemistry 1967, 4th ed., Oxford, UK, Pergamon press

18. O. Kubaschewski and C.B. Alcock Metallurgical thermodynamic chemistry 1979, 5th ed., Oxford, UK, Pergamon press
19. R. Hultgren, R. Orr, P. Anderson, and K.K. Kelley Selected values of the thermodynamic properties of binary alloys 1963, New York, John Wiley and Sons
20. R. Hultgren, P.D. Desai, D.T. Hawkins, M. Glesier, and K.K. Kelley Selected values of the thermodynamic properties of binary alloys 1973, Metals park, OH, American society for metals
21. L. Brewer, and R.H. Lamoreaux Thermochemical properties. In: Molybdenum: physico-chemical properties of its compounds and alloys 1908, International atomic energy agency, Vienna, P.11-191
22. L. Brewer, and R.H. Lamoreaux Phase diagrams. In: Molybdenum: physico-chemical properties of its compounds and alloys 1908, Vienna: International atomic energy agency, P-195-356
23. L. Kaufman, and H. Bernstein Computer calculation of phase diagrams 1970, New York academic press
24. C.G. Maier and K.K. Kelley “An equation for the representation of high temperature heat content data” *Journal of the American chemical society* 1932, Vol.54, No.8, P.3243-3246
25. F. D. Murnaghan “The compressibility of media under extreme pressures” *Proceedings of the national academy of sciences of the United States of America* 1944, Vol.30, No.9, P.244-247

26. G. Inden “Approximate description of the configurational specific heat during a magnetic order-disorder transformation,” *Project meeting Calphad V*, Session 111, Paper 4, Dusseldorf, W. Germany, 1976, P.1-13
27. M. Hillert, M. Jarl “A model for alloying effects in ferromagnetic metals” *Calphad* 1978, Vol.2, No.3, P.227-238
28. M.Margules “Über die Zusammensetzung der gesättigten Dämpfe von Mischungen” *Sitzungsber Akad Wiss Wien* 1895, Vol.104, P.1243-1278
29. R. Luoma “A Thermodynamic Analysis of the System Fe-Cr-Ni-C-O” in: Acta polytechnica scandinavica, Chemical technology series No: 292, Helsinki 2002, Published by the Finnish academies of technology, ISBN 951-666-615-9, ISSN 1239-0518
30. O. Redlich and A.T. Kister “Algebraic representation of thermodynamic properties and the classification of solutions” *Industrial and engineering chemistry* 1948, Vol.40, No.2, P.345-348
31. H.L. Lukas, S.G. Fries, and B. Sundman in Computational thermodynamics, the calphad method, Cambridge university press, United Kingdom, 2007, P.79-160
32. F. Kohler “Zur Berechnung der thermodynamischen Daten eines ternären Systems aus den zugehörigen binären Systemen / To the computation of the thermodynamic data of a ternary system from the associated binary systems” *Monatshefte für Chemie / Chemical Monthly* 1960, Vol.91, No. 4, P.738-740

33. G.W. Toop “Predicting ternary activities using binary data” *Transactions of the metallurgical society of American institute of mining engineers* 1965, Vol.233, No.5, P.850-855
34. Y.M. Muggianu, M. Gambino, J.P. Bros “Choices of an Analytical Representation of Integral and Partial Excess Quantities of Mixing” *Journal of chemical physics* 1975, Vol.72, No. 1, P.83-88
35. B. Sundman and J. Ågren “A regular solution model for phases with several components and sublattices, suitable for computer applications” *Journal of physics and chemistry of solids* 1981, Vol.42, No.4, P.297-301
36. F. Sommer “Influence of associate formation in alloy melts on the thermodynamic quantities” *Calphad* 1978, Vol.2, No.4, P.319-324
37. M. Hillert, B. Jansson, B. Sundman, and J. Ågren “Two-sublattice model for molten solutions with different tendency for ionization” *Metallurgical transactions A (Physical metallurgy and materials science)* 1985, Vol.16A, No.2, P.261-266
38. H.L. Lukas, E.Th. Henig, and B. Zimmermann “Optimization of phase diagrams by a least squares method using simultaneously different types of data” *Calphad* 1977, Vol.1, No.3, P.225-236
39. H.L. Lukas and S.G. Fries “Demonstration of the use of BINGSS with the Mg-Zn system as example” *Journal of phase equilibria* 1992, Vol.13, No.5, P.532-541

40. B. Jansson in Evaluation of parameters in thermochemical models using different types of experimental data simultaneously, TRITA-MAC-0234, Royal institute of technology, Sweden, 1984
41. http://www.crct.polymtl.ca/factsage/fs_optisage.php
42. A.T. Dinsdale “SGTE data for pure elements” *Calphad* 1991, Vol.15, No.4, P.317–425
43. F. Frandsen, K. Dam-Johansen, P. Rasmussen “A pure substance trace element thermochemical database” *Calphad* 1996, Vol.20, No.2, P.175-229
44. I. Ansara, C. Chatillon, H.L. Lukas, T. Nishizawa, H. Ohtani, K. Ishida, M. Hillert, B. Sundman, B.B. Argent, A. Watson, T.G. Chart, T. Anderson “Binary database for III-V compound semiconductor systems” *Calphad* 1994, Vol.18, No.2, P.177-222
45. A.D. Pelton “Database and sublattice model for molten salts” *Calphad* 1988, Vol.12, No.2, P.127-142
46. <http://www.metallpass.com/software/sw.aspx?CatID=12>
47. B. Sundman “Thermodynamic databanks, visions and facts” *Scandinavian journal of metallurgy* 1991, Vol.20, No.1, P.79-85
48. U.R. Kattner, W.J. Boettinger, S.R. Coriell “Application of Lukas' phase diagram programs to solidification calculations of multicomponent alloys” *International journal of materials research* 1996, Vol.87, No.7, P.522-528

49. N. Saunders and A. P. Miodownik in Calphad (Calculation of phase diagrams) A comprehensive guide, Pergamon materials series, Vol.1, Ed. R. W. Cahn, Oxford, 1998
50. S.G. Fries, B. Sundman “Development of multicomponent thermodynamic databases for use in process modelling and simulations” *Journal of physics and chemistry of solids, Proceedings of the 11th International Conference on High Temperature Materials Chemistry (HTMC-XI) 2005*, Vol.66, No.2-4, P.226-230
51. J. -O. Anderson, T. Helander, L. Höglund, P. Shi, and B. Sundman “Thermo-Calc and Dictra, computational tools for materials science” *Calphad 2002*, Vol.26, No.2, P.273-312
52. C.W. Bale, P. Chartrand, S.A. Degterov, G. Eriksson, K. Hack, R. Ben Mahfoud, J. Melançon, A.D. Pelton, and S. Petersen, “FactSage thermochemical software and databases” *Calphad 2002*, Vol.26, No.2, P.189-228
53. S. -L. Chen, S. Daniel, F. Zhang, Y.A. Chang, X.-Y. Yan, F.-Y. Xie, R. Schmid-Fetzer, and W.A. Oates, “The PANDAT software package and its applications” *Calphad 2002*, Vol.26, No.2, P.175-188
54. R.H. Davies, A.T. Dinsdale, J.A. Gisby, J.A.J. Robinson, and S.M. Martin, “MTDATA: Thermodynamic and phase equilibrium software from national physical laboratory” *Calphad 2002*, Vol.26, No.2, P.229-271
55. L.V. Gurvich “IVTANTHERMO data bank” *Vestnik AN SSSR 1983*, No.3, P.54-

56. B Jansson, Ph.D. Thesis “Computer operated method for equilibrium calculations and evaluation of thermochemical model parameters” 1984 Royal institute of technology, Stockholm, Sweden.
57. G. Eriksson “Thermodynamic studies of high-temperature equilibria, XII. SOLGASMIX, a computer program for calculation of equilibrium compositions in multiphase systems” *Chemica Scripta* 1975, Vol.8, P.100-103
58. G. Eriksson “Thermodynamic studies of high temperature equilibria, XII. SOLGAS, a computer program for calculating the composition and heat condition of an equilibrium mixture” *Acta chemica scandinavica* 1971, Vol.25, P.2651-2658
59. TCC, Thermo-Calc software user’s guide, version R, Stockholm, Sweden, 2006
60. K. Hack (editor) in: The SGTE casebook, Thermodynamics at work 1996, Scientific group thermodata europe, Institute of materials (London, England)
61. J. Agren, F. H. Hayes, L. Hoglund, U. R Kattner, R. Schmid-Fetzer, B. Legendre, “Applications of computational thermodynamics” *Zeitschrift fuer metallkunde/Materials research and advanced techniques* 2002, Vol.93, No.2, P.128-142
62. M. Hillert “Some viewpoints on the use of a computer for calculating phase diagrams” *Physica B: Condensed matter* 1981, Vol.103, No.1, P.31-40
63. J.H. Mathews in: Numerical methods for computer science, engineering, and mathematics, Englewood Cliffs, New Jersey, Prentice-Hall, 1987

64. H. Ohtani, M. Yamano, M. Hasebe “Thermodynamic analysis of the Fe-Al-C ternary system by incorporating ab initio energetic calculations into the calphad approach” *ISIJ International* 2004, Vol.44, No.10, P.1738-1747
65. H. Ohtani, M. Yamano, M. Hasebe “Thermodynamic analysis of the Co-Al-C and Ni-Al-C systems by incorporating ab initio energetic calculations into the CALPHAD approach” *Calphad* 2004, Vol.28, No.2, P.177-190
66. H. Ohtani, N. Hanaya, M. Hasebe, S. Teraoka, M. Abe “Thermodynamic analysis of the Fe-Ti-P ternary system by incorporating first-principles calculations into the CALPHAD approach” *Calphad* 2006, Vol.30, No.2, P.147-58
67. M. Palumbo, F.J. Torres, J.R. Ares, C. Pisani, J.F. Fernandez, M. Baricco “Thermodynamic and ab initio investigation of the Al-H-Mg system” *Calphad* 2007, Vol.31, No.4, P.457-467
68. N. Dupin, S.G. Fries, J.-M. Joubert, B. Sundman, M.H.F. Sluiter, Y. Kawazoe, A. Pasturel “Using first-principles results to calculate finite-temperature thermodynamic properties of the Nb-Ni μ phase in the Bragg-Williams approximation” *Philosophical magazine* 2006, Vol.86, No.12, P.1631-1641
69. Y.A. Chang, S. Chen, F. Zhang, X. Yan, F. Xie, R. Schmid-Fetzer, and W.A. Oates “Phase diagram calculation: past, present and future” *Progress in materials sciences* 2004, Vol.49, No.3-4, P.313–345
70. R. Schmid-Fetzer, A. Janz, J. Gröbner, and M. Ohno “Aspects of quality assurance in a thermodynamic Mg alloy database” *Advanced engineering materials* 2005, Vol.7, No.12, P.1142–1149

71. S.-L. Chen, K.-C. Chou, and Y. A. Chang “On a new strategy for phase diagram calculation 1. Basic principles” *Calphad* 1993, Vol.17, No.3, P.237-250
72. S.-L. Chen, K.-C. Chou, Y. A. Chang “On a new strategy for phase diagram calculation 2. Binary systems” *Calphad* 1993, Vol.17No.3, P.287-302
73. X.-Y. Yan, Y.A. Chang, F.-Y. Xie, S.-L. Chen, F. Zhang, S. Daniel “A thermodynamic approach for predicting the tendency of multicomponent metallic alloys for glass formation” *Journal of alloys and compounds* 2001, Vol.320, No.6, P.151–160
74. G. Kaptay “A new equation for the temperature dependence of the excess Gibbs energy of solution phases” *Calphad* 2004, Vol.28, No.2, P.115-124
75. S.-L. Chen, S. Daniel, F.Zhang, Y.A. Chang, W.A. Oates, R. Schmid-Fetzer “On the calculation of multicomponent stable phase diagrams” *Journal of phase equilibria* 2001, Vol.22, No.4, P.373–378
76. A. Davydov, U.R. Kattner “Thermodynamic assessment of the Co-Mo system” *Journal of phase equilibria* 1999, Vol.20, No.1, P.5-16
77. C. Vahlas, P.Y. Chevalier, and E. Blanquet, “Thermodynamic evaluation of four Si-M (M = Mo, Ta, Ti, W) binary systems” *Calphad* 1989, Vol.13, No.3, P.273-292
78. N. Saunders “The Al-Mo system (aluminum-molybdenum)” *Journal of phase equilibria* 1997, Vol.18, No.4, P.370-378

79. I. Ansara, A.T. Dinsdale, and M.H. Rand (Eds.): COST 507: Thermochemical database for light metals alloys, European communities, Luxembourg, ISBN 92-828-3902-8, 1998
80. M. Kurata, and Y. Sakamura “Thermodynamic assessment of systems of actinide or rare earth with Cd” *Journal of phase equilibria* 2001, Vol.22, No.3, P.232–240
81. D. Kevorkov, R. Schmid-Fetzer, F. Zhang “Phase equilibria and thermodynamics of the Mg-Si-Li system and remodeling of the Mg-Si system” *Journal of phase equilibria and diffusion* 2004, Vol.25, No.2, P.140–151
82. H. Feufel, T. Gödecke, H.L. Lukas, and F. Sommer “Investigation of the Al-Mg-Si system by experiments and thermodynamic calculations” *Journal of alloys compounds* 1997, Vol.247, P.31-42
83. X-Y. Yan, F. Zhang, and Y.A. Chang “A thermodynamic analysis of the Mg-Si system” *Journal of phase equilibria and diffusion* 2000, Vol.214, No.2, P.379-84
84. V. Grolier, R. Schmid-Fetzer “Thermodynamic analysis of the Pt-Sn system” *Journal of alloys and compounds* 2008, Vol.450, No.1-2, P.264-271
85. X. Su, F. Yin, M.Huang, Z. Li, C. Chen “Thermodynamic assessment of the Pt-Sn system” *Journal of alloys and compounds* 2001, Vol.325, No.1-2, P.109-12
86. T. Balakumar and M. Medraj “Thermodynamic modeling of the Mg-Al-Sb system” *Calphad* 2005, Vol.29, No.1, P.24-36
87. A.D. Pelton “The Cd-Na (Cadmium-Sodium) system” *Bulletin of alloy phase diagrams* 1988, Vol.9, No.1, P.41-46

88. A.D. Pelton “Thermodynamics and phase diagrams of materials” in: Phase transformations in materials, edited by G. Kostorz, Weinheim, New York Chichester. Wiley-VCH, 2001
89. B-J. Lee “Thermodynamic assessment of the Sn-Zn and In-Zn binary systems”, *Calphad* 1996, Vol.20, No.4, P.471-480
90. A.D. Pelton “Phase diagrams” in: Physical metallurgy, edited by R.W. Cahn and P. Haasen, Amsterdam, Elsevier, 1983
91. S.A. Degterov, A.D. Pelton, and J.D. L'Ecuyer, “Thermodynamic optimization of the selenium-arsenic (Se-As) system” *Journal of phase equilibria* 1997, Vol.18, No.4, P.357-368
92. C. Guo, Z. Du, C. Li “A thermodynamic description of the Gd-Mg-Y system” *Calphad* 2007, Vol.31, No.1, P.75-88
93. C. Servant “Thermodynamic assessments of the phase diagrams of the hafnium-vanadium and vanadium-zirconium systems” *Journal of phase equilibria and diffusion* 2005, Vol.26, No.1, P.39-49
94. L. Zhang, Y. Du, H. Xu, Z. Pan “Experimental investigation and thermodynamic description of the Co-Si system” *Calphad* 2006, Vol.30, No.4, P.470-481
95. W. Huang, M. Selleby “Thermodynamic assessment of the Nb-W-C system” *Zeitschrift fuer Metallkunde/Materials Research and Advanced Techniques* 1997, Vol.88, No.1, P.55-62
96. J-O. Andersson “Thermodynamic properties of Mo-C” *Calphad* 1988, Vol.12, No.1, P.1-8

97. P. Bellen, K.C. Hari Kumar, and P. Wollants “Thermodynamic assessment of the Ni-Ti phase diagram” *Zeitschrift fuer metallkunde/Materials research and advanced techniques* 1996, Vol.87, No.12, P.972-978
98. P. Gustafson “Thermodynamic evaluation of the Fe-C system” *Scandinavian Journal of Metallurgy* 1985, Vol.14, No.5, P.259-267
99. A. Gabriel, P. Gustafson, I. Ansara “Thermodynamic evaluation of the C-Fe-Ni system” *Calphad* 1987, Vol.11, No.3, P.203-218
100. N. Dupin, I. Ansara “Evaluation thermodynamique du systeme Al-Co (Thermodynamic assessment of the Al-Co system)” *Revue de Metallurgie* 1998, Vol.95, No.9, P.1121-1129
101. N. Dupin, I. Ansara “Thermodynamic assessment of the Cr-Ta system” *Journal of phase equilibria and diffusion* 1993, V.14, N.4, P.451-456
102. S-D. Choi “Thermodynamic analysis of the Co-Si system” *Calphad* 1992, Vol.16, No.2, P.151-159
103. S-A. Cho, and J.L. Ochoa “Detailed assessment of integral thermodynamic quantities of liquid Bi-Sn alloy solution system” *Metallurgical and materials transactions B: Process metallurgy and materials processing science* 1997, Vol.28, No.6, P.1081-1087
104. B-J. Lee “Revision of thermodynamic descriptions of the Fe-Cr & Fe-Ni liquid phases” *Calphad* 1993, Vol.17, No.3, P.251-268
105. E.A. Guggenheim in: Mixtures: the theory of the equilibrium properties of some simple classes of mixtures, solutions and alloys 1952, Oxford: Clarendon press

106. R. Kikuchi “A theory of cooperative phenomena” *Physical review* 1951, Vol.81, No.6, P.988-1003
107. C.H.P. Lupis, J.F. Elliott “Prediction of enthalpy and entropy interaction coefficients by the “Central Atoms” theory” *Acta metallurgica* 1967, Vol.15, P.265–267
108. R. Arroyave, Z.K. Liu “Thermodynamic modelling of the Zn-Zr system” *Calphad* 2006, Vol.30, No.1, P.1–13
109. R. Schmid-Fetzer, D. Andersson, P.Y. Chevalier, L. Eleno, O. Fabrichnaya, U.R. Kattner, B. Sundman, C. Wang, A. Watson, L. Zabdyr, and M. Zinkevich “Assessment techniques, database design and software facilities for thermodynamics and diffusion” *Calphad* 2007, Vol.31, No.1, P.38–52
110. D.W. Scott, R.W. Tapia, J.R. Thompson “Nonparametric probability density estimation by discrete penalized-likelihood criteria” *The annals of statistics* 1980, Vol.8, No.4, P.820–832
111. P. Lancaster, and K. Šalkauskas in: Curve and surface fitting, an introduction, London, Orland, Academic Press, 1986
112. B.I. Kvasov “Isogeometric interpolation by generalized splines” *Russian journal of numerical analysis and mathematical modeling* 1996, Vol.11, No.3, P.223
113. H. Akima “A new method of interpolation and smooth curve fitting based on local procedures” *Journal of the ACM* 1970, Vol.17, No.4, P.589–602

114. H. Akima “A method of bivariate interpolation and smooth surface fitting for irregularly distributed data points” *ACM Transactions on mathematical software* 1978, Vol.4, No.2, P.148–159
115. L.D. Irvine, S.P. Marin, P.W. Smith “Constrained interpolation and smoothing” *Constructive approximation* 1986, Vol.2, No.1, P.129–151
116. C.A. Micchelli, P.W. Smith, J. Swetits, J.D. Ward “Constrained Lp approximation” *Constructive approximation* 1985, Vol.1, No.1, P.93–102
117. D.V. Malakhov, S.V. Zykina, V.I. Kosyakov “Matching of phase equilibrium data. I. Foundations of the method” *Russian journal of physical chemistry* 1989, Vol.63, No.2, P.180–182
118. G.F. Voronin, and S.A. Degtyarev “Spline-approximation of thermodynamic properties of solutions” *Calphad* 1982, Vol.6, No.3, P.217-27
119. F.A. Vetter, and O. Kubaschewski “” *Zeitschrift für Elektrochemie* 1953, Vol.57, No., P.243-248
120. Y.K. Rao, B.V. Patil “Thermodynamic study of the Mg-Sb system” *Metallurgical transactions* 1971, Vol.2, No.7, P.1829-1835
121. C.A. Eckert, R.B. Irwin, J.S. Smith “Thermodynamic activity of magnesium in several highly-solvating liquid alloys” *Metallurgical transactions B (Process metallurgy)* 1983, Vol.14B, No.3, P.451-458
122. G. Grube “” *Zeitschrift für anorganische chemie* 1906, Vol.49, No., P.87
123. G. Grube, and R. Bornhak “” *Zeitschrift für elektrochemie* 1934, Vol.40, No., P.140

124. A.A. Nayeb-Hashemi, and J.B. Clark “” Bulletin of alloy phase diagrams 1985, Vol.5, No., P.579-584
125. B. Jönsson, and J. Ågren “Theoretical evaluation of chemical ordering and glass transition in liquid Mg-Sb alloys” *Metallurgical transactions A (Physical metallurgy and materials science)* 1987, Vol.18A, No.8, P.1395-1401
126. B. Jönsson, and J. Ågren “Chemical ordering and isentropic temperatures in Mg-Sb-Sn system” *Zeitschrift fuer metallkunde* 1987, Vol.78, No.11, P.810-814
127. D.V. Malakhov “Thermodynamic assessment of the Bi-Zn system” *Calphad* 2000, Vol.24, No.1, P.1-14
128. L. Zabdyr, and Z. Moser “Thermodynamic studies on Mg-Sb system” *Bulletin of the polish academy of sciences: Technical sciences* 1983, Vol.31, No.1-12, P.37-42
129. J.J. Egan “Thermodynamics of liquid magnesium alloys using CaF//2 solid electrolytes” *Journal of nuclear materials* 1974, Vol.51, No.1, P.30-35
130. O. Kubaschewski, and A. Walter-Stuttgart “Results of investigations of alloys by high-temperature calorimetry” *Zeitschrift für elektrochemie* 1939, Vol.45, P.732-740
131. W.R.D. Jones, and L. Powell “” *Journal of the institute of metals* 1941, Vol.67, P.177-188
132. N. Subasic “Thermodynamic evaluation of Sn-Zr phase diagram” *Calphad* 1998, Vol.22, No.2, P.157–165

133. N. Dupin, I. Ansara, C. Servant, C. Toffolon, C. Lemaignan, J.C. Brachet “A thermodynamic database for zirconium alloys” *Journal of nuclear materials* 1999, Vol.275, No.3, P.287–295
134. R.J. Hanson “Linear least squares with bounds and linear constraints” *SIAM Journal on scientific and statistical computing* 1986, Vol.7, No.3, P.826–834
135. H.L. Lukas, J. Weiss, E.-Th Henig “Strategies for the calculation of phase diagrams” *Calphad* 1982, Vol.3, No.3, P.229-251
136. A.D. Pelton “On the slopes of phase boundaries” *Metalurgical transactions A* 1988, Vol.19A, No.7, P.1819-1825.
137. D.A. Goodman, J.W. Cahn, L.H. Bennett “The centennial of the Gibbs–Konovalov rule for congruent points” *Bulletin of alloy phase diagrams* 1981, Vol.2, No.1, P.29-35
138. K. Schittkowski “NLPQL, A Fortran subroutine solving constrained nonlinear programming problems” *Annals of operations research* 1986, Vol.5, P.485-500
139. M. Hillert in: Phase equilibria phase diagrams and phase transformations, Cambridge University Press, 1998.
140. J. Nakano, D.V. Malakhov, S. Yamaguchi, G.R. Purdy “A full thermodynamic optimization of the Zn–Fe–Al system within the 420 – 500 °C temperature range” *Calphad* 2007, Vol.31, No.1, P.125-140
141. M. Hillert and L.-I. Staffanson “Regular solution model for stoichiometric phases and ionic melts” *Acta chemica scandinavica* 1970, Vol.24, No.10, P.3618–26

142. H. Guye, and J. Wilfringer in: Second international symposium on metallurgical slags and fluxes 1984, “Modeling of the thermodynamic properties of complex metallurgical slags”, Ed. H.A. Fine, and D.R. Warrendale, MA: TMS, P.357-375
143. A.D. Pelton, and P. Chartrand “The modified quasi-chemical model: Part II. Multicomponent solutions” *Metallurgical and materials transactions A: Physical metallurgy and materials science* 2001, Vol.32, No.6, P.1355-1360
144. A.D. Pelton, and P. Chartrand “The modified quasi-chemical model: Part III. Two sublattices” *Metallurgical and materials transactions A: Physical metallurgy and materials science* 2001, Vol.32, No.6, P.1397-1407
145. A.D. Pelton, and P. Chartrand “The modified quasi-chemical model: Part IV. Two-sublattice quadruplet approximation” *Metallurgical and materials transactions A: Physical metallurgy and materials science* 2001, Vol.32, No.6, P. 1409-1416
146. T. Lyche and K. Mørken in: Spline methods, Draft version, Available at <http://folk.uio.no/in329/nchap1.pdf>

APPENDIX I

Bezier curves and spline curves

The following Table A1 specifies the Bezier and spline functions [146] of linear, quadratic and cubic orders. The measurements are assumed to be in a two dimensional plane and are specified by $c_1(x_1, y_1), c_2(x_2, y_2), c_3(x_3, y_3)$ and $c_4(x_4, y_4)$.

The arbitrary numbers t_2, t_3, \dots, t_7 and t lie on the x axis and satisfy the condition

$$t_2 < t_3 < \dots < t_7$$

The linear Bezier/spline curve is essentially the line connecting the points c_2 and c_3 . The quadrature curve is fitted through three points and the cubic one is through four. Higher order Bezier/spline curves can be derived in similar fashion.

Table A1: Bezier and spline functions of different order

	Bezier curve	Spline curve
Linear	$p(t) = p(t c_1, c_2)$ $= (1-t)c_1 + tc_2$	$p(t) = p(t c_1, c_2; t_2, t_3) \quad t \in [t_2, t_3]$ $= \left(\frac{t_3 - t}{t_3 - t_2} \right) c_1 + \left(\frac{t - t_2}{t_3 - t_2} \right) c_2$
Quadratic	$p_{1,1}(t) = p(t c_1, c_2)$ $p_{2,1}(t) = p(t c_2, c_3)$ $p_{2,2}(t) = p(t c_1, c_2, c_3)$ $= (1-t)p_{1,1}(t) + tp_{2,1}(t)$ $= (1-t)^2 c_1$ $+ 2(1-t)c_2 + t^2 c_3$	$p(t) = p(t c_1, c_2, c_3; t_2, t_3, t_4, t_5)$ $= \left(\frac{t_4 - t}{t_4 - t_3} \right) p(t c_1, c_2; t_2, t_3)$ $+ \left(\frac{t - t_3}{t_4 - t_3} \right) p(t c_2, c_3; t_3, t_4)$

Cubic	$p_{3,3}(t) = (1-t)p_{2,2}(t) + tp_{3,2}(t)$ $= (1-t)^3 c_1 + 3t(1-t)^2 c_2$ $+ 3t^2(1-t)c_3 + t^3 c_4$	$p(t) = p(t c_1, c_2, c_3, c_4; t_2, t_3, t_4, t_5, t_6, t_7)$ $= \left(\frac{t_5 - t}{t_5 - t_4} \right) p(t c_1, c_2, c_3; t_2, t_3, t_5, t_6)$ $+ \left(\frac{t - t_4}{t_5 - t_4} \right) p(t c_2, c_3, c_4; t_3, t_4, t_6, t_7)$
-------	---------------------------------------------------------------------------------------------------------	----------------------------------------------------------------------------------------------------------------------------------------------------------------------------------------------------------------------------------------------

APPENDIX II

Derivatives to calculate $\frac{dx^S}{dx^L}$, $\frac{dT}{dx^L}$, $\frac{d^2x^S}{d(x^L)^2}$, **and** $\frac{d^2T}{d(x^L)^2}$

In order to calculate dx^S/dx^L and dT/dx^L from (8.13) and (8.14) the following derivatives (10.1)-(10.6) should be calculated.

$$\frac{\partial f_1}{\partial x^L} = -x^L \frac{\partial^2 G^L}{\partial (x^L)^2} - \frac{\partial G^S}{\partial x^L} + \frac{dx^S}{dx^L} \frac{\partial G^S}{\partial x^S} + x^S \frac{\partial^2 G^S}{\partial x^S \partial x^L} \quad (10.1)$$

$$\frac{\partial f_2}{\partial x^L} = (1-x^L) \frac{\partial^2 G^L}{\partial (x^L)^2} - \frac{\partial G^S}{\partial x^L} + \frac{dx^S}{dx^L} \frac{\partial G^S}{\partial x^S} - (1-x^S) \frac{\partial^2 G^S}{\partial x^S \partial x^L} \quad (10.2)$$

$$\frac{\partial f_1}{\partial x^S} = x^S \frac{\partial^2 G^S}{\partial (x^S)^2} \quad (10.3)$$

$$\frac{\partial f_2}{\partial x^S} = -(1-x^S) \frac{\partial^2 G^S}{\partial (x^S)^2} \quad (10.4)$$

$$\frac{\partial f_1}{\partial T} = \frac{\partial G^L}{\partial T} - x^L \frac{\partial^2 G^L}{\partial x^L \partial T} - \frac{\partial G^S}{\partial T} + x^S \frac{\partial^2 G^S}{\partial x^S \partial T} \quad (10.5)$$

$$\frac{\partial f_2}{\partial T} = \frac{\partial G^L}{\partial T} + (1-x^L) \frac{\partial^2 G^L}{\partial x^L \partial T} - \frac{\partial G^S}{\partial T} - (1-x^S) \frac{\partial^2 G^S}{\partial x^S \partial T} \quad (10.6)$$

Similarly the derivatives associated with the calculation of $d^2x^S/d(x^L)^2$, and

$d^2T/d(x^L)^2$ are given below in (10.7)-(10.18).

$$\begin{aligned} \frac{\partial^2 f_1}{\partial (x^L)^2} &= -\frac{\partial^2 G^L}{\partial (x^L)^2} - x^L \frac{\partial^3 G^L}{\partial (x^L)^3} - \frac{\partial^2 G^S}{\partial (x^L)^2} + \frac{d^2 x^S}{d(x^L)^2} \frac{\partial G^S}{\partial x^S} \\ &+ 2 \frac{dx^S}{dx^L} \frac{\partial^2 G^S}{\partial x^S \partial x^L} + x^S \frac{\partial^3 G^S}{\partial x^S \partial (x^L)^2} \end{aligned} \quad (10.7)$$

$$\begin{aligned} \frac{\partial^2 f_2}{\partial (x^L)^2} &= -\frac{\partial^2 G^L}{\partial (x^L)^2} + (1-x^L) \frac{\partial^3 G^L}{\partial (x^L)^3} - \frac{\partial^2 G^S}{\partial (x^L)^2} + \frac{d^2 x^S}{d(x^L)^2} \frac{\partial G^S}{\partial x^S} \\ &+ 2 \frac{dx^S}{dx^L} \frac{\partial^2 G^S}{\partial x^S \partial x^L} - (1-x^S) \frac{\partial^3 G^S}{\partial x^S \partial (x^L)^2} \end{aligned} \quad (10.8)$$

$$\frac{\partial^2 f_1}{\partial x^S \partial x^L} = \frac{dx^S}{dx^L} \frac{\partial^2 G^S}{\partial (x^S)^2} + x^S \frac{\partial^3 G^S}{\partial (x^S)^2 \partial x^L} \quad (10.9)$$

$$\frac{\partial^2 f_2}{\partial x^S \partial x^L} = \frac{dx^S}{dx^L} \frac{\partial^2 G^S}{\partial (x^S)^2} - (1-x^S) \frac{\partial^3 G^S}{\partial (x^S)^2 \partial x^L} \quad (10.10)$$

$$\frac{\partial^2 f_1}{\partial T \partial x^L} = -x^L \frac{\partial^3 G^L}{\partial T \partial (x^L)^2} - \frac{\partial^2 G^S}{\partial T \partial x^L} + \frac{dx^S}{dx^L} \frac{\partial^2 G^S}{\partial x^S \partial T} + x^S \frac{\partial^3 G^S}{\partial x^S \partial x^L \partial T} \quad (10.11)$$

$$\frac{\partial^2 f_2}{\partial T \partial x^L} = (1-x^L) \frac{\partial^3 G^L}{\partial T \partial (x^L)^2} - \frac{\partial^2 G^S}{\partial T \partial x^L} + \frac{dx^S}{dx^L} \frac{\partial^2 G^S}{\partial x^S \partial T} - (1-x^S) \frac{\partial^3 G^S}{\partial x^S \partial x^L \partial T} \quad (10.12)$$

$$\frac{\partial^2 f_1}{\partial T \partial x^S} = x^S \frac{\partial^3 G^S}{\partial (x^S)^2 \partial T} \quad (10.13)$$

$$\frac{\partial^2 f_2}{\partial T \partial x^S} = -(1-x^S) \frac{\partial^3 G^S}{\partial (x^S)^2 \partial T} \quad (10.14)$$

$$\frac{\partial^2 f_1}{\partial T^2} = \frac{\partial^2 G^L}{\partial T^2} - x^L \frac{\partial^3 G^L}{\partial x^L \partial T^2} - \frac{\partial^2 G^S}{\partial T^2} + x^S \frac{\partial^3 G^S}{\partial x^S \partial T^2} \quad (10.15)$$

$$\frac{\partial^2 f_2}{\partial T^2} = \frac{\partial^2 G^L}{\partial T^2} + (1-x^L) \frac{\partial^3 G^L}{\partial x^L \partial T^2} - \frac{\partial^2 G^S}{\partial T^2} - (1-x^S) \frac{\partial^3 G^S}{\partial x^S \partial T^2} \quad (10.16)$$

$$\frac{\partial^2 f_1}{\partial(x^s)^2} = \frac{\partial^2 G^s}{\partial(x^s)^2} + x^s \frac{\partial^3 G^s}{\partial(x^s)^3} \quad (10.17)$$

$$\frac{\partial^2 f_2}{\partial(x^s)^2} = \frac{\partial^2 G^s}{\partial(x^s)^2} - (1-x^s) \frac{\partial^3 G^s}{\partial(x^s)^3} \quad (10.18)$$